Developing high-efficiency compound Semiconductor III-V Quantum-Dot Solar Cells

Phu-Minh Lam

A thesis submitted to University College of London for the degree of Doctor of Philosophy (PhD)

Department of Electronics and Electrical Engineering, University College London

July 2016

Statement of originality

I, Phu-Minh Lam, confirm that the work presented in this thesis is my own. Where information has been derived from other sources, I confirm that this has been indicated in the thesis.

Signed: _____

Date: _____

To my parents, Senh Khuong Lam and
Sau Denh Lam,

thank you for helping to give me the
life I love today.

Abstract

A concept of utilising discrete energy levels to form an Intermediate Band (IB) within the bandgap of a semiconductor solar cell has been studied. Such a feature can be achieved using nanostructured quantum systems. A nanocrystal Quantum Dot (QD) - forms discrete energy states from its confinement potential, which could be exploited as an IB. The IB acts like a stepping-stone to absorb sub-bandgap energy photons. This concept, of the Intermediate Band Solar Cell (IBSC), was established in 1997. In theory, it could deliver a maximum conversion efficiency of 63%. After the phenomenon called two-step photon excitation had been demonstrated with QD-IBSCs, enthusiasm in this solar cell research followed. IBSC has allowed a proof-of-concept for more efficient absorption of the solar spectrum, bypassing the conventional single-junction solar cell concept. Thus, it is a suitable candidate for high efficiency photovoltaic cells. Fabrication efforts with suitable materials have become one of the main focuses to establish IBSCs in the hope of optimising the conversion efficiency using this concept.

This thesis explores the IBSC development using QD materials incorporated into III-V solar cells. The work includes experimental investigations that were carried out to study the effect of QD modification on the QD solar cell performance. The fabrication challenges facing the establishment of IBSC are described here. To tackle them, epitaxial growth as well as post-growth techniques have been studied. This work uses III-V semiconductor QDs that were fabricated using solid-state Molecular Beam Epitaxy technology. Imaging techniques such as Atomic Force Microscopy (AFM) and Transmission Electron Microscopy (TEM) have been employed to study the surface morphology and the material quality of the QDs and the grown samples.

Optical and electrical characterisation tools have enabled empirical studies on the solar cells. These include Photoluminescence (PL), External Quantum Efficiency (EQE) and current density-voltage (J-V) measurements. The work includes the study of (1) the material quality of submonolayer quantum dot (SML-QD) solar cells; (2) the effect of direct n-type doping on the voltage-recovery characteristic of charged QDs; (3) the effect of post-growth rapid thermal annealing technique used on QD solar cells and; (4) the characteristics of high bandgap barrier InAs/InGaP quantum dot solar cells.

At the end of this thesis, the conclusions drawn from the experimental work are presented, followed by a proposal for a new QD solar cell design. The new design consists of a type-II QD configuration embedded in a high bandgap material. It aims to extend the carrier lifetime within the QD as well as creating an efficient multi-step photon absorption pathway. The structural layout of the proposed QD solar cell is outlined with type-II InAs/GaAsSb QD system enclosed with AlGaAs confinement enhancing layer, which could be fabricated in future work.

Acknowledgement

I would like to thank Professor Huiyun Liu for his supervision and support. His guidance has led me into becoming an independent researcher. He shared with me his immense knowledge about III-V semiconductor crystals and has made suggestions to the direction of my work. In the process of constructing state-of-the-art research for QD solar cells, there were challenges at various stages of fabrication and characterisation. Each step of the way throughout this process was reported quarterly to Professor James Wilson and Ms. Rebecca Allison from Defence Science and Technology Laboratory (Dstl). I thank them for their time on reviewing my work and giving me very useful feedbacks. I thank Dstl for the generosity of sponsoring my research.

Along the research journey, I have also received great support from the Postdoc researchers and other PhD candidates in the group, including Yunyan Zhang, Dongyoung Kim, Arthur Onno, Mingchu Tang, Pamela Jurczak, Sabina Hatch, Hao Xu, Mengya Liao, Bingjun Yu, Qi Jiang, Siming Chen, Peter Carrington, Frank Tutu, Andrew Lee and Kevin Lee, and I thank them all deeply for the advice and the good times they have shared with me. A special thank goes to Dr. Jiang Wu who has provided excellent consultancy to me and my work. I thank Dr. Steve Hudziak for extending his duty as a lab manager and aided me through my work. Most of the conversation we have shared together in the group goes beyond the details of science, but the meaning of nature and changes in life. I suppose that is what defines philosophy, and I cannot thank enough those who have shared this with me because it has profoundly developed me into who I am today. I would like to mention that, due to the intensity of my research work over the past few years, the time I could spend with my family has shortened considerably. I would like to extend my gratitude to my family for their continual support, and acceptance of my regular absence. Last but not

least, to those who have shared with me warmth, kindness and sweetness at the times of my struggle, those were good memories and I will keep them securely, always.

Table of Contents

List of Figures

List of publications

Journal Publications:

1. P. Lam, J. Wu, M. Tang, D. Kim, S. Hatch, I. Ramiro, V. G. Dorogan, M. Benamara, Y. I. Mazur, G. J. Salamo, J. Wilson, R. Allison, H. Liu, "InAs/InGaP quantum dot solar cells with an AlGaAs interlayer", **Sol. Energy Mater. Sol. Cells**, vol 144, pp 96–101, 2016.
2. P. Lam, J. Wu, S. Hatch, D. Kim, M. Tang, H. Liu, R. Wilson, and R. Allison, "The Effect of Rapid Thermal Annealing on InAs/GaAs Quantum Dot Solar Cells," **IET Optoelectron**., Vol. 9, Iss. 2, pp. 65–68, 2015.
3. P. Lam, S. Hatch, J. Wu, M. Tang, V. G. Dorogan, Y. I. Mazur, G. J. Salamo, I. Ramiro, A. Seeds, and H. Liu, "Voltage recovery in charged InAs/GaAs quantum dot solar cells," **Nano Energy**, vol 6, pp. 3–8, Apr. 2014.
4. P. Lam, J. Wu, M. Tang, Q. Jiang, S. Hatch, R. Beanland, J. Wilson, R. Allison, and H. Liu, "Submonolayer InGaAs/GaAs quantum dot solar cells," **Sol. Energy Mater. Sol. Cells**, vol. 126, pp. 83–87, Jul. 2014.
5. S. Hatch, J. Wu, K. Sablon, P. Lam, M. Tang, Q. Jiang, and H. Liu, "InAs/GaAsSb quantum dot solar cells," **Opt. Express**, vol. 22, no. S3, p. A679, Mar. 2014.
6. F. K. Tutu, J. Wu, P. Lam, M. Tang, N. Miyashita, Y. Okada, J. Wilson, R. Allison, and H. Liu, "Antimony mediated growth of high-density InAs quantum dots for photovoltaic cells," **Appl. Phys. Lett.**, vol. 103, no. 4, p. 043901, 2013.

7. F. K. Tutu, P. Lam, J. Wu, N. Miyashita, Y. Okada, K.-H. Lee, N. J. Ekins-Daukes, J. Wilson, and H. Liu, "InAs/GaAs quantum dot solar cell with an AlAs cap layer," **Appl. Phys. Lett.**, vol. 102, no. 16, p. 163907, 2013.

Conference and Symposia Publications:

1. P. Lam, J. Wu, M. Tang, D. Kim, S. Hatch, I. Ramiro, V.G. Dorogan, M. Benamara, Y.I. Mazur, G.J. Salamo, J. Wilson, R. Allison and H. Liu, "III-V Semiconductor Quantum Dot Solar Cells, Defence and Security Doctoral Symposium", Defence Academy of the United Kingdom (2015)
2. P. Lam, J. Wu, M. Tang, D. Kim, S. Hatch, I. Ramiro, V.G. Dorogan, M. Benamara, Y.I. Mazur, G.J. Salamo, J. Wilson, R. Allison and H. Liu, "InAs/InGaP Quantum Dot Solar Cells with an AlGaAs Interlayer", Advances in concentration Photovoltaic, Imperial College London (2015)
3. P. Lam, J. Wu, S. Hatch, J. Wilson and H. Liu, "Voltage Recovery in Direct-Si doped Quantum Dot Solar Cells", QD day, University of Sheffield (2014)
4. P. Lam, S. Hatch, J. Wu, M. Tang, V. G. Dorogan2, Y. I. Mazur, G. J. Salamo, I. Ramiro, A. Seeds and H. Liu, "Voltage Recovery in Direct-Si doped Quantum Dot Solar Cells", UK Semiconductor Conference, University of Sheffield (2014)
5. P. Lam, F. Tutu, J. Wu, R. Allison, J. Wilson and H. Liu, "III-V Semiconductor Quantum Dot Solar Cells" Defence and Security PhD Scheme Conference, Kassam Stadium (Oxford) (2013)
6. P. Lam, J. Wu, F. Tutu, R. Allison, J. Wilson and H. Liu, "Improvement in Short-circuit Current due to Sb-mediated Enhancement in Quantum Dot Density", Advance in Photovoltaics conference, Institute of Physics (2013)
7. P. Lam, J. Wu, F. Tutu, R. Allison, J. Wilson and H. Liu, "Submonolayer Quantum Dot Solar Cells", UK Semiconductor Conference, University of Sheffield (2013)

Chapter 1

Introduction

1.1 **Background**

Energy is one of the pillars of civilisation development that upholds the global economy today. However, the heavy dependence of energy supply from the combustion of fossil fuels, to power industrial economies, came with large societal and environmental impacts, with almost poisonous side-effects. It results in disputed consequences of oil price fluctuations and global warming from around the world. It started since the 19th century industrialisation when oil demand became high. Simultaneously anthropogenic activities such as deforestation were also common. These processes and activities have released considerable amounts of greenhouse gases into the environment. Today, the rise in atmospheric temperatures has led to irreversible environmental impacts. Extreme weather events (i.e. heat waves, droughts and heavy rainfalls) jeopardize the world economy by decreasing crop yields which puts food security to threat. It is also increasingly prominent in changing rain and snow patterns in recent years, adding concerns to unpredictable inundations. This leaves little need to mention why the world cannot continue to rely on fossil fuel combustion.

The adverse effect of global warming has incentivised political leaders around the world to put a limit to fossil fuel consumption, with a signed agreement named the

Kyoto protocol to the United Nations Framework Convention on Climate Change (UNFCCC) in 1995 Conference of Parties (COP) 3. More recently, the 2015 COP21 Paris Climate conference has achieved a legally binding agreement to keep global warming below 2 °C. The goal is to prevent further dangerous anthropogenic interference in our natural climate system. Thus, industrialised countries are now set with binding obligations to reduce emission of greenhouse gases. Despite this, fossil fuel consumption is still occurring at a high pace, underpinned by the exponential growth of population and energy demand.

Geological specialists have forecasted a complete depletion of crude oil reserves in the few forthcoming decades [1]. This urges scientists to find new solutions of energy provision to ensure a continuous and sustainable future economy. Without it, an oil crisis would likely occur, similarly to the last one seen in 1986. To prevent a global stagnation, a replacement is required to overtake energy supply from fossil fuels. However, historical lessons have taught us to take precaution in this approach. Despite that there are a handful of choices available for this replacement, the benefits and drawbacks are always weighed against each other. For example, the past has seen catastrophic cases of nuclear power implementation with either poor design or lack of environmental measures. The 1986 Chernobyl and 2011 Fukushima nuclear disasters are notorious manmade examples that entailed profound aftermaths [2]. Learning from this, environmental-related circumstances play a major role in determining the choice for future energy sources. The important question is how to continue growing our economy with a low-carbon regime.

Renewable energy has received recognition for its potential strength in transforming our current economy to a long-term sustainable one. Based on the *Renewable Energy Policy Network for the 21st Century* (REN21), renewable energy is currently supplying 19 % of the world's energy consumption [3], with the majority contributed from biomass. The rest is derived from hydroelectric, solar, wind and geothermal energy, and biofuels. Despite a steady progression, it is still not catching up with the energy demand that is expected to increase sharply over the next few decades. Taking into consideration population growth, the projected energy demand

for 2050 is 30 terawatts (TW) [4]. Compared with the current consumption of 13 TW, there is a significant shortfall of 17 TW.

	Gross theoretical useful potential	***Technical feasible potential***
Biomass	8 – 14 TW	6 – 8 TW
Hydraulic	4.6 TW	1.6 TW
Geothermal	66 TW	11.6 TW
Wind	20 TW	2 TW
Solar	600 TW	60 TW
Waves/tide	234 TW	No data
Total	1030 TW (approx.)	85 TW (approx.)

Table 1: The energy production from various renewable energy resources tabulated with gross theoretical potential and technical feasibility potential. (data from [5]***).***

Putting the maximum potential energy supply from renewable energy sources into consideration, the only sufficient energy source is light from the Sun. It is capable of meeting the 17 TW shortfall for a very simply reason - vastness. The solar radiation on Earth surface represents ~1000 Watts per square meter ($W.m^{-2}$). The technically feasible potential that can be harnessed is an astounding 60 TW from the 600 TW gross theoretical useful potential (see Table 1), which is far greater than that which other renewables could provide. Therefore, even a fraction of this is enough to supply the predicted global energy demand in 2050 [6]. Furthermore, solar energy is known as a consistent source for at least another thousand years. Based on these facts, it is rather surprising to see that very little solar energy has been utilised compared with fossil fuels.

Solar energy is characterised by being abundant, inexhaustible and clean. It can be harnessed by capturing light and transforming it into electricity using photovoltaic technology. Charles Fritts first demonstrated the phenomenon in 1885 [7]. Unfortunately, it did not receive much attention because the efficiency was extremely small to be considered attractive. Furthermore, the society around the time had already become dependent on fossil fuel combustion at a very cheap price. In fact, earlier

photovoltaic modules are an assembly of semiconductor solar cells, commonly made of electrode-connected silicon crystals. It took many years for photovoltaic cells to be competitive with fossil fuels in terms of price. This is because the low solar-to-electricity conversion efficiency made a major hindrance, which allowed other technologies to overshadow the beauty of solar cells. With the consensus of global warming consequences, the photovoltaic market has progressed more rapidly than the most optimistic forecasts in the last 20 years.

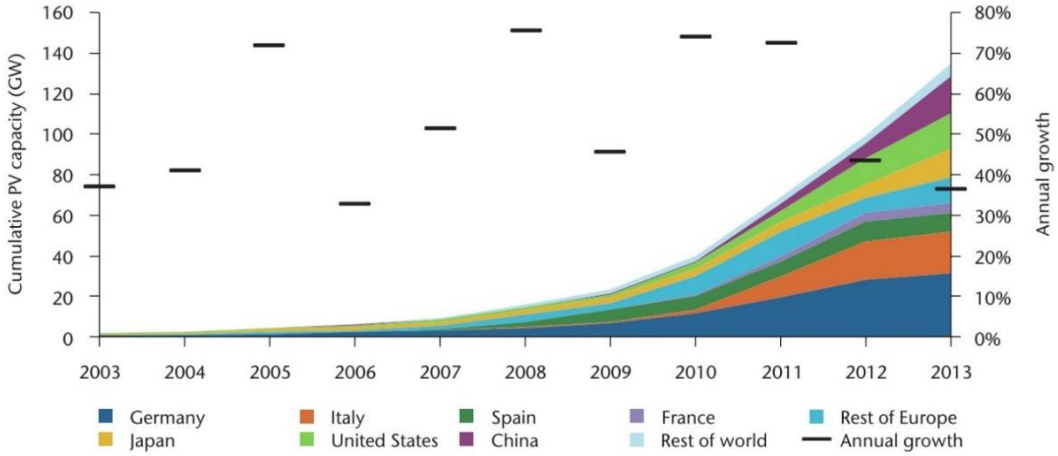

Figure 1.1: Global cumulative growth of photovoltaic capacity from 2003 to 2013 showing the rapid development of different countries. The annual growth presented in percentage is shown on the right axis. [6].

Figure 1.1 shows the development of photovoltaic cumulative installed capacities around the world. The photovoltaic industry is growing exponentially in terms of cumulative capacity, with China currently leading the momentum, followed by the US and Japan. However, whilst grid-connected photovoltaic capacity increases at an annual average rate of 60%, making it the fastest growing energy technology, the best efficiency performances for crystalline Si and GaAs thin film solar cells are only 25.6 ±0.5 % and 28.8 ±0.9 % under AM1.5G spectrum, respectively [8]. To assist with the deployment of photovoltaic energy around the world, solar cells must first satisfy industrial expectations in terms of reliability and performance. Solar modules are considered durable and require low maintenance. The qualification, manufacturing and reliability testing methodologies for solar modules can be found in the report

released by Sunpower in 2010 [9]. Many suppliers today would guarantee a solar panel lifespan of 25 years. On the other hand, solar cell efficiency performances still need to improve in order to reduce the overall system cost, as will be explained in later sections.

Solar cell devices offer a number of niche advantages such as being lightweight and the ability to supply energy in remote locations compared to fossil fuels. They operate silently without releasing any by-products. These advantages alone make them suitable for applications in many industries spanning from satellite, telecommunications and housing. In the last decade, many architectural designs around the world have exploited the aesthetic quality of solar cells, where in addition to producing electricity for a building, they also take the role of a building element, known as 'building integrated photovoltaic' [10]. Product designers have used solar cells for energy provision in many familiar low-power applications as far back as the first solar-powered calculator in 1970.

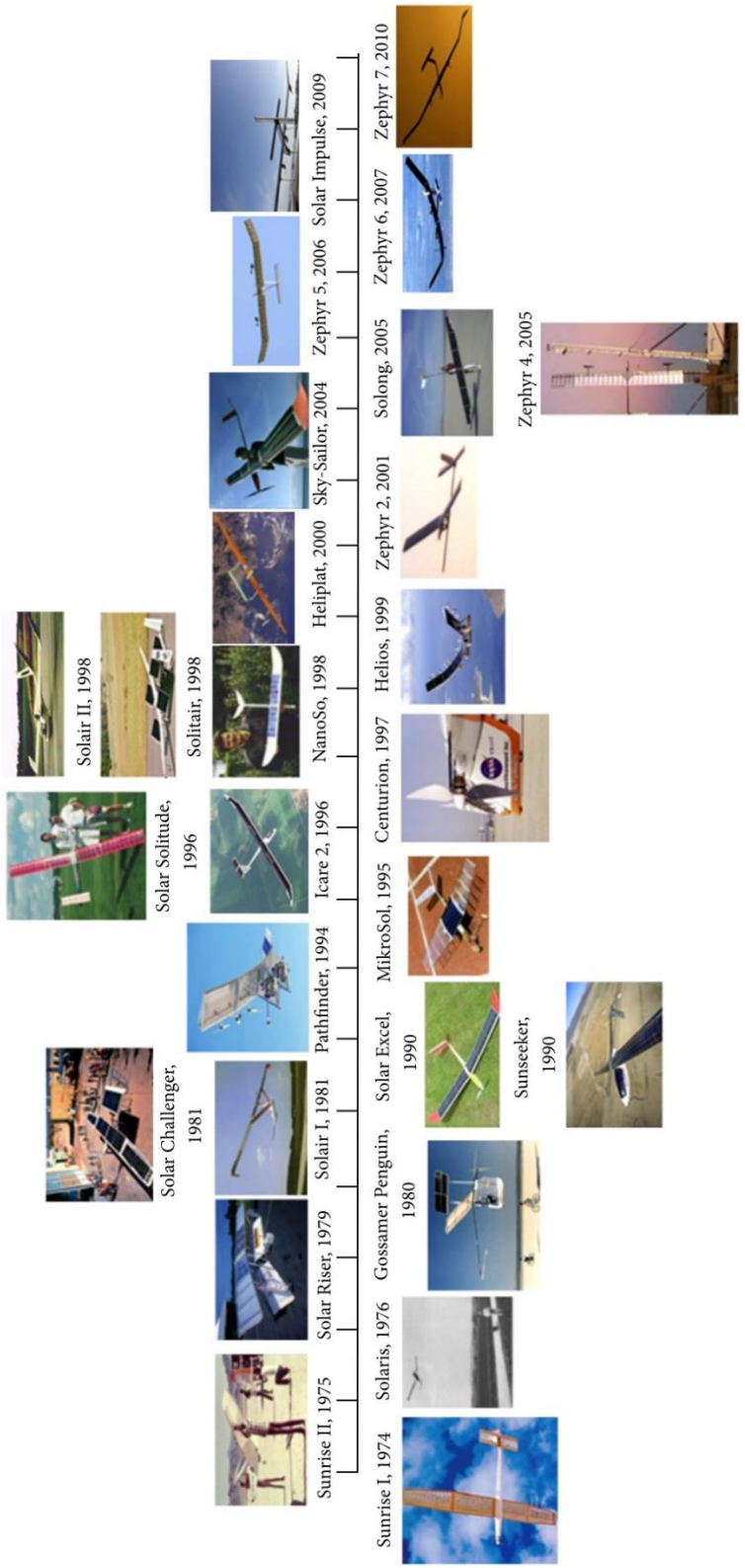
Sunrise I, 1974
Solaris, 1976
Gossamer Penguin, 1980
Solar Excel, 1990
Sunseeker, 1990
MikroSol, 1995
Centurion, 1997
Helios, 1999
Zephyr 2, 2001
Solong, 2005
Zephyr 4, 2005
Zephyr 6, 2007
Zephyr 7, 2010
Sunrise II, 1975
Solar Riser, 1979
Solair I, 1981
Solar Challenger, 1981
Pathfinder, 1994
Icare 2, 1996
Solar Solitude, 1996
NanoSo, 1998
Solair II, 1998
Solitair, 1998
Heliplat, 2000
Sky-Sailor, 2004
Zephyr 5, 2006
Solar Impulse, 2009

Figure 1.2: A timeline of the solar-powered flights since 1974 showing the persistent progression of the aircraft design with solar cells which illustrates the need of developing efficient solar cells to support the aerospace industry [11].

The aeroplane is perhaps one of the most celebrated inventions in the world. Some aircraft have now got solar cells incorporated into their design, and are named solar aeroplanes. They are perhaps the best example to showcase the effect of photovoltaic technology on other industries. Figure 1.2 shows a timeline of solar aeroplanes built since 1974. It illustrates the evolution of the design and engineering of solar aeroplanes over the last four decades. In 2010, the British-built Unmanned Aerial Vehicle (UAV) Zephyr flew 2 weeks non-stop by using only solar energy to power its propellers. It was described as "the eternal plane". The aeroplane has shown the potential to stay airborne with significant endurance. The solar energy collected by the amorphous Si-covered 22.5m wingspan and stored in Lithium-sulphur batteries, is sufficient to keep the propellers running at night. Such solar-powered high altitude long-endurance UAVs are expected to have a wide range of applications.

In respect to military applications, employing photovoltaic cells can facilitate infantry operation by accessing energy source remotely, allowing extended UAV operation, and adding flexibility to the geographical manoeuvrability and gain advantage in warzones. Photovoltaic technology can help to reduce the burden on soldiers from carrying large quantities of batteries, and cut down transportation and supply of fossil fuels to operating bases.

There are far more examples of solar cell prototypes than the actual practical applications in the market. The challenge remains in improving the efficiency whilst keeping the manufacturing cost of photovoltaic cells low [12]. Achieving this would make way for more affordable usage of solar energy so that it could extend to a wider range of industries. There is a clear growing interest from various industries, only waiting for a suitable compromise in photovoltaic devices in terms of efficiency and cost. The equation below illustrates the factors affecting the overall installation cost [13]:

$$C_{installed}\left(W_p^{-1}\right) = \frac{\left(C_{module}(m^{-2}) + C_{BOS}(m^{-2})\right)}{Conversion\ Efficiency\ (\%)\ \times 1{,}000\ W_p m^{-2}} \quad (1)$$

where, $C_{installed}$ is the cost per watt-peak of the installed system whilst C_{module} and C_{BOS} are the cost per area of the module and the cost per area of the balance of system, respectively. The solar cell industry aims to bring photovoltaic electricity prices to levels comparable with electricity from fossil fuels, along with all the above-mentioned benefits, at ~ 0.05-0.06 USD.kWh^{-1}. It can be achieved in two ways as shown in equation (1), which is either by reducing the manufacturing cost so that the cost per module area or area of the balance of system is low, or achieving higher solar cell power conversion efficiency. Continuous effort is ongoing to optimise this balance. It has been reported in 2014 that solar photovoltaic technology is increasingly competitive at the utility scale [14]. Despite this, within the physics of solar cells there is a fundamental thermodynamic limitation for single-junction solar cell efficiency. This is known as the Shockley-Quiesser detailed balance limit [15]. The immediate response to this problem was to engage in Multi-Junction Solar Cell (MJSC) systems, which have shown record efficiencies above 40% under concentration (see Figure 1.3). MJSCs use multi-layers of semiconductor materials with different bandgaps, making the solar cell highly photosensitive to the solar spectrum. However, the cost involved in this type of solar cell, which uses expensive group IV and III-V semiconductor crystals, has hindered its affordability. This has left photovoltaic researchers to seek for an alternative approach to develop a solar cell with similar efficiencies as MJSCs using inexpensive materials.

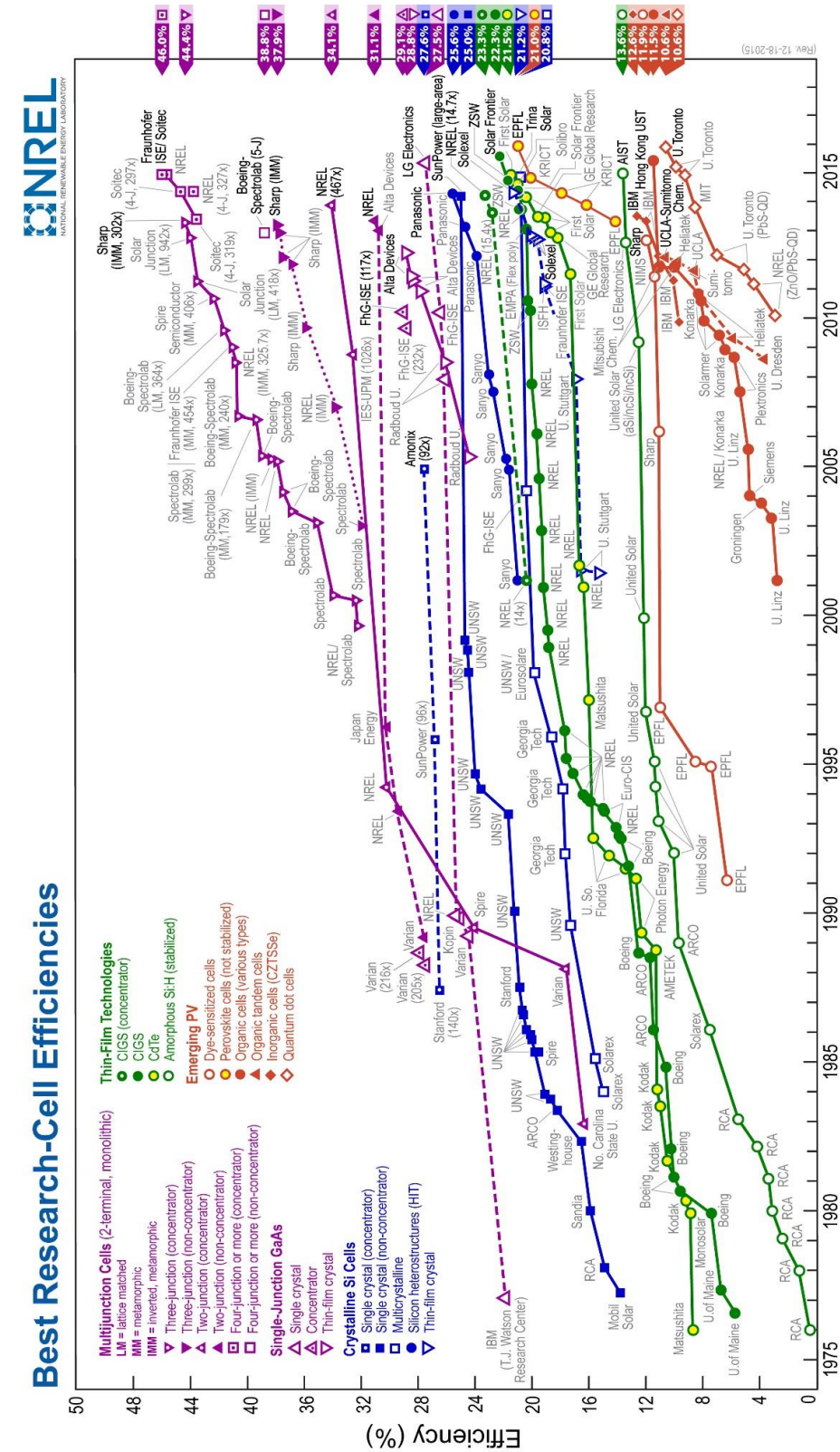
Best Research-Cell Efficiencies
NREL
NATIONAL RENEWABLE ENERGY LABORATORY
Efficiency (%)
Multijunction Cells (2-terminal, monolithic)
LM = lattice matched
MM = metamorphic
IMM = inverted, metamorphic
Three-junction (concentrator)
Three-junction (non-concentrator)
Two-junction (concentrator)
Two-junction (non-concentrator)
Four-junction or more (concentrator)
Four-junction or more (non-concentrator)
Single-Junction GaAs
Single crystal
Concentrator
Thin-film crystal
Crystalline Si Cells
Single crystal (concentrator)
Single crystal (non-concentrator)
Multicrystalline
Silicon heterostructures (HIT)
Thin-film crystal
Thin-Film Technologies
CIGS (concentrator)
CIGS
CdTe
Amorphous Si:H (stabilized)
Emerging PV
Dye-sensitized cells
Perovskite cells (not stabilized)
Organic cells (various types)
Organic tandem cells
Inorganic cells (CZTSSe)
Quantum dot cells
46.0%
44.4%
38.8%
37.9%
34.1%
31.1%
29.1%
28.8%
27.6%
27.5%
25.6%
25.0%
23.3%
22.3%
21.5%
21.2%
21.0%
20.8%
13.6%
12.6%
11.9%
11.5%
10.6%
10.6%
(Rev. 12-18-2015)

Figure 1.3: Record efficiencies of dominant photovoltaic solar cells technologies over time with progression showing the earliest record since 1976 and new entries along this technology roadmap. The highest efficiency has been reported by Fraunhofer at 46.0% in 2015 – from NREL [16].

Figure 1.3 shows record efficiencies, at the research scale, for dominant photovoltaic solar cell technologies over time by the *National Renewable Energy Laboratory*. In 2015, the highest efficiency is achieved by a four-junction solar cell under concentrated illumination, with 46.0% in conversion efficiency. It can be seen that crystalline silicon solar cells are showing signs of saturation in their performance under non-concentrated illumination. It is known from thermodynamic physics that these type of solar cells are already very close to their maximum power output. On the other hand, new emerging solar cells such as organic and QD solar cells are showing a rise in the efficiency performance. These material-types are very attractive in a sense that they allow exploration of new phenomena, providing the possibility of a scientific breakthrough.

Some QD materials to generate high efficiency and low cost solar cells have been proposed [17]. They range from multi-carrier generation, to hot carrier and intermediate band solar cells [18]. To mention the former, multi-carrier generation solar cells uses an energetic photo-excited electron to vigorously "knock-off" inactive electrons via a kinetic collision to generate two or more carriers. Hot carrier solar cells take advantage from prolonged thermalisation to extract hot electrons. All of these are designed to surpass the single-junction Shockley-Quiesser efficiency limit, but the intermediate band solar cell concept surpasses these with a theoretical efficiency of ~63% [19].

1.2 **The Concept of Intermediate Band Solar Cell**

The Intermediate Band Solar Cell (IBSC) concept is based on introducing an energy level in the bandgap of a single-junction solar cell. This energy level is designated to lie between the Valence Band (VB) and Conduction Band (CB), which creates two sub-bandgaps. The two sub-bandgaps are responsible for a different regional coverage of the solar spectrum, which widens the total absorption spectrum

for the photovoltaic cell. This concept is analogous in some way to the MJSC, which aims to better exploit the full width of the solar spectrum [20]. It was proposed by Martí and Luque in 1997 with a recognised possibility to significantly improve the photocurrent via multi-photon absorption [19]. Following photo-absorption, an electron from the VB can get promoted directly to the CB, or otherwise get promoted to the IB if the photon energy is insufficient for a direct VB→CB transition. From the IB, another low-energy photon can promote the electron to the CB. This way, the system can utilise lower-energy photons to induce an electron transition, as shown in Figure 1.4. The figure illustrates that the photon with energy α can induce a direct VB→CB transition, but this is restricted to single-junction solar cells where photons with energy β or γ are lost. The introduction of the IB could absorb the photons with energy β and γ as well as α. Therefore, IBSC can absorb more efficiently the solar spectrum.

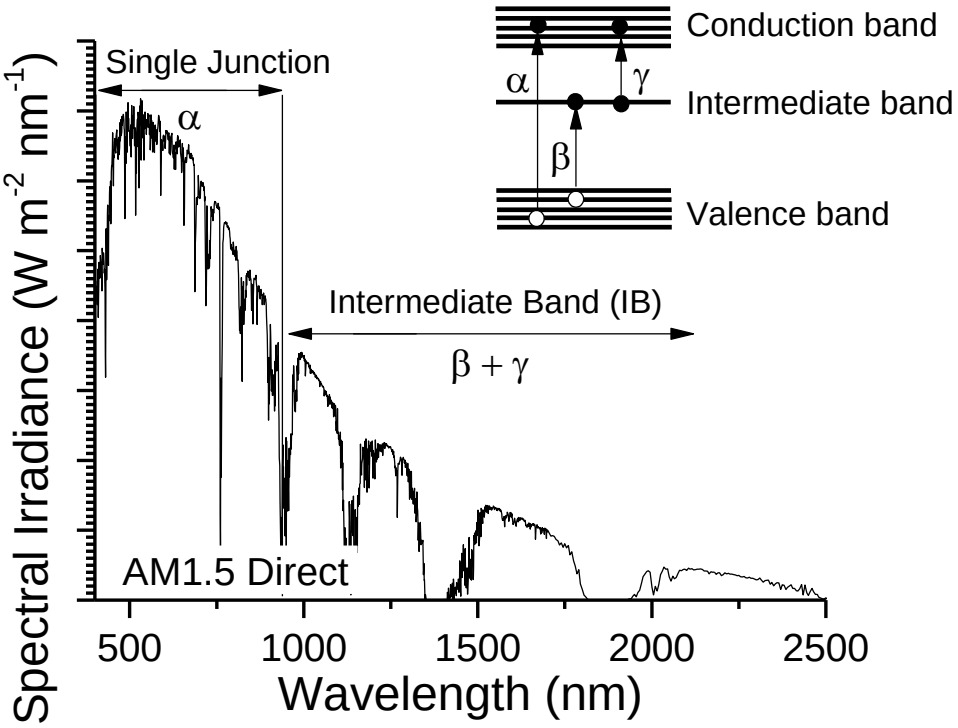

Figure 1.4: A diagram illustration of the spectral irradiance coverage of an intermediate band solar cell using a two-step photoexcitation and the respective absorption coverage of a single junction bandgap represented by α and the two sub-bandgaps represented by β and γ.

Despite that there are already calculations for multiple sub-bandgap energies suitable for optimum IBSC operations; theory is far ahead of current IBSC prototype development. One of the reasons is that tuning the position of the IB requires a very good understanding of the material properties that are used to produce this system. In nanotechnology, some newly established fabrication techniques have created flexibility in manufacturing atomically precise nanostructures, leading to the exploration of novel structures in solar cells research. This has led to the discovery of new material properties. Among various efforts involved in the development of IBSC, zero-dimensional quantum dots (QDs) with nominally discrete density of states have attracted much attention [20].

1.2.1 Employing Quantum Dots to form the Intermediate Band

The discrete energy levels in QDs can be employed in IBSCs, with the electron ground states in the QDs tentatively designated as the IB. It exhibits fundamental zero-dimension physics. The 3D potential confinement gives rise to different optical and electrical properties compared to its bulk counterpart. QDs offer flexible tuning of the effective bandgap via modification of their shape and size. This allows optical properties to be tuned to correspond to the desired wavelengths [17-18]. Therefore, QDs could benefit solar cells by tuning for a desirable optical sensitivity to cover specific parts of the solar spectrum.

QDs are also suitable in conjunction with MJSCs due to extended photon absorption compared with their bulk counterpart; thus it may also introduce additional absorption in the sub-cell and provide a better way to manage the current matching [18-19]. Another advantage of QD solar cells is their radiation tolerance compared to their bulk counterpart [24], which makes QD solar cells more suitable for space applications [21-22]. Moreover, the properties of QDs have already given rise to new optical and electrical properties, leading to the production of enhanced optoelectronic devices such as QD lasers, optical modulators and mid-infrared photodetectors [27].

Semiconductor QDs are the preferred material system to demonstrate potential IBSC efficiency of 63 %. The discrete energy states from the QDs are suitable to form the IB, which is not possible to achieve from bulk materials unless deep level doping is involved [28]. The proof-of-concept two-photon absorption phenomenon has demonstrated the feasibility of QD-IBSCs. It has proven that there is a feasible core mechanism for approaching IBSC efficiency. In brief, the experiment used QD solar cells to induce a VB→IB and IB→ CB excitation using infra-red biased external quantum efficiency measurement in cryogenic conditions [29]. It proved that additional photocurrent generation is possible using multi-step photoabsorption [30]. Primarily, it demonstrated that III-V semiconductor QD could be used to establish IBSC.

It is now important to optimise the photoexcitation pathway to promote electrons to and from the IB. The hindering problems in the fabrication process must be addressed in order to make the IB operate effectively. Usually, self-assembled InAs-QDs embedded in GaAs barrier material are used as the workhorse to test IBSC operating principles. Although the sub-bandgaps exhibited in this material system differ from what is required for optimal IBSCs, self-assembled InAs/GaAs QD materials are the most widely studied because their growth mechanism is well-known.

1.2.2 Current Challenges

QD-IBSC using InAs/GaAs QD materials typically exhibit a VB→CB transition energy equal to the GaAs bandgap. The VB to IB transition is dependent on the size of the QDs which determines the ground state position in the confinement potential. InAs-QD/GaAs materials typically have a thermal activation energy of 130 meV. This is approximately the energy difference between the Ground State (GS) of the QD to the CB of the GaAs. The small thermal activation energy is unable to thermally isolate the carriers in the QD from the CB. The easy communication between those two levels creates a thermal coupling effect. This was once thought to be a beneficial mechanism as it helps to promote carriers from the IB to the CB, which contributes to the photocurrent output. However, permitting a thermal transition of carriers between the

IB and the CB consequently enables an overwhelmingly high rate of carrier escape from the QD, known as thermal escape. This occurs much more rapidly than the IB→CB optical absorption process. As a result, it suppresses the second-photon IB→CB excitation pathway at room temperature [31]. For this reason, the practicality of QD-IBSCs in the commercial aspect remains elusive.

The thermal coupling problem also leads to an insufficient split of quasi-Fermi levels which determine the open-circuit voltage. As a result, InAs/GaAs QD solar cells usually suffer from a reduced open-circuit voltage [16,28-29]. This leads to a major loss in the solar cell efficiency. The voltage-loss problem is also seen in InAs/GaAsSb QD [34], InAs/AlGaAs QD [35] and InAs/GaAs/GaNAs QD [36] solar cells. In the past, attempts to raise the CB bandgap offset have used high bandgap capping layers such as AlGaAs [25,33] and InGaP [38]. They have demonstrated empirical success in reducing the carrier escape rates. However, the solar cells made with those material systems still face many practical problems, and the QDs material quality is not entirely blameless for the reduction in open-circuit voltage and photocurrent.

Poor material quality could be a result of high density of inherent defects. This has always been a practical limitation to solar cell performances. Defects in QD solar cells, either consequence of a lattice-mismatch or impurity-induced, form non-radiative recombination centres in the crystal lattice and degrade the solar cell performances [39]. Moreover, the layering of QD structures is restricted by the effect of the lattice-mismatched heterostructures, creating a strain field within the QD/barrier interface. This produces strain-induced defects that also form non-radiative (NR) recombination centres [30]. This puts a limit to the contribution of sub-bandgap photon absorption to the photocurrent [40]. The persistence of these problems in QD solar cells must be addressed in order to realise high photocurrent density with maximum open-circuit voltage output. It is therefore equally important to improve crystal material quality in order to create unobstructed pathways for carriers in QD-IBSCs.

1.3 **Thesis Outline**

The physics of solar cells including the dynamics of QDs are covered in the next chapter. This is followed by the experimental methods that were designed to study III-V semiconductor QD solar cells. It consists of QD solar cell growth, device development, imaging and electrical and optical characterisations. It details the necessary steps involved in fabricating a QD solar cell considering the physics involved. Further to this, there are four chapters of research work carried out to implement proposed ideas on QD solar cells.

The fourth chapter will report the research work on successfully fabricated Submonolayer Quantum Dot (SML-QD) solar cells, which was directly compared with Quantum Well (QW) solar cells [41]. This preliminary investigation outlines the importance of the strain-relaxation mechanism in the growth of QD layers. A reduction in the density of crystal defects is seen for SML-QD solar cells.

In the fifth chapter, the effect on QD solar cells of direct Si-doping in the QD material is reported [42]. The work is designed to tackle one of the main problems that face QD IBSCs. It aims to recover the voltage of the QD IBSCs, which is crucial for QD solar cells to realise the potential in achieving IBSCs.

In the sixth chapter, the effect of rapid thermal annealing treatment of QD solar cells is reported. The work tackles the problem of defect-induced NR recombination centres in grown QD solar cells. A successful reduction in defect density was demonstrated with the post-growth thermal process.

In the seventh chapter, the fabrication of a QD solar cell with high bandgap barrier structure is reported using the InAs/InGaP QD system [43]. Issues with the structure growth were resolved using an AlGaAs interlayer technique. Successful fabrication of QD solar cells, consisting of a bandgap configuration close to that of the ideal IBSC, has been demonstrated.

Finally, the thesis will end with a proposal for future work on QD IBSCs. It will involve discussion on some key aspects in the investigation efforts required in order to achieve a QD solar cell with high conversion efficiency.

Chapter 2

The Physics of Solar Cells

2.1 Semiconductor Solar Cells

A semiconductor is traditionally a crystal body formed by a network of atoms. Each atom is covalently bonded to the neighbouring ones. A covalent bond is responsible for pairing up an outer-shell electron with another outer-shell electron from a neighbouring atom. Figure 2.1 shows a picture of how a semiconductor crystal gives rise to its electronic energy profile. The left of the figure depicts a molecular network with atoms represented by black circles. The electron pair forms a covalent bond that binds two atoms together. Electrons are fermion particles, and due to Pauli's exclusion principle, no two fermions can exist in identical energy states (except for the case of having different spin states), hence no two electrons in an atom have identical quantum numbers. When applied to solids, no two electrons with the same spin character in a solid can have identical energy states. Therefore, with the gigantic number of atoms in the crystal lattice, the density of states in a semiconductor crystal is the concatenation of a very large number of very closely packed energy states, forming continuous yet finite energy band. Special to semiconductor crystals is the presence of an energy bandgap (E_G), which distinguishes semiconductors from metals. A semiconductor has two separate energy bands of interest, the higher CB corresponding to the first empty band at 0K and the lower VB corresponding to the last band fully occupied at 0K. The energy gap between these two bands forbids any

electron to have an energy level comprised between the VB and the CB, as shown on the right of Figure 2.1.

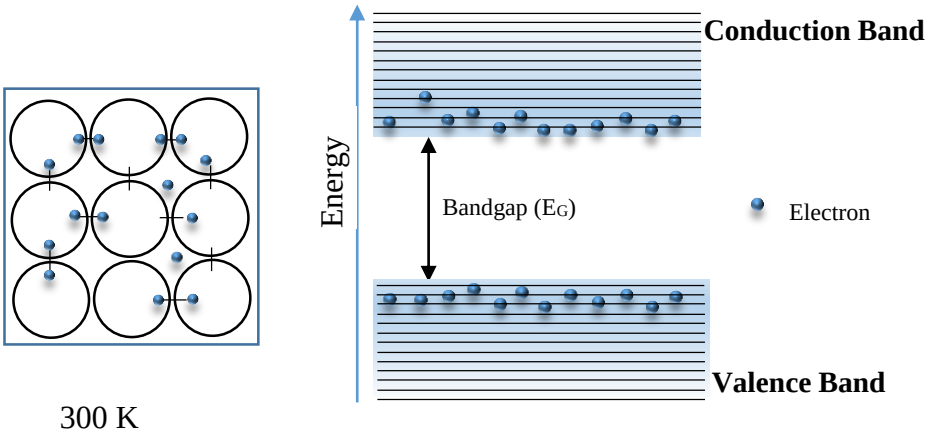

Figure 2.1: A schematic illustration of the rise of conduction and valence bands in a semiconductor. The left shows a simplified drawing of atomic outer-shells with electrons pairs forming covalent bonds. The right shows an energy diagram with electronic states within the conduction band and valence band separated by a bandgap.

The distribution of electrons in the CB and VB is governed by the Fermi-Dirac distribution function $[f(E)]$ which provides the probability of occupancy of energy levels:

$$f(E) = \frac{1}{1 + e^{(E-E_F)/kT}} \qquad (2)$$

where, E_F is the Fermi energy level where all the electrons will occupy under at 0K, approximately in the middle of the VB and CB, as depicted in Figure 2.2, k is the Boltzmann constant and T is the temperature. At absolute 0K, no electrons can occupy the CB.

At 300K, the CB hosts electrons with high energy, which can flow freely in the semiconductor. Contrarily, the VB hosts electrons with low energy, which remain stuck around the same atom nucleus. Higher energy electrons are pictured as those loosely bounded in the covalent bond. If a bound electron absorbs sufficient energy

(e.g. from thermal excitation), it breaks free from the covalent bond and joins the pool of loose electrons in the crystal, which is equivalent to the electrons getting promoted from the VB to the CB. The addition of electrons into the CB means a higher density of free-flowing electrons in the crystal lattice space. This raises conductivity, and is a feature that is paramount for semiconductor materials to exhibit a solar cell behaviour.

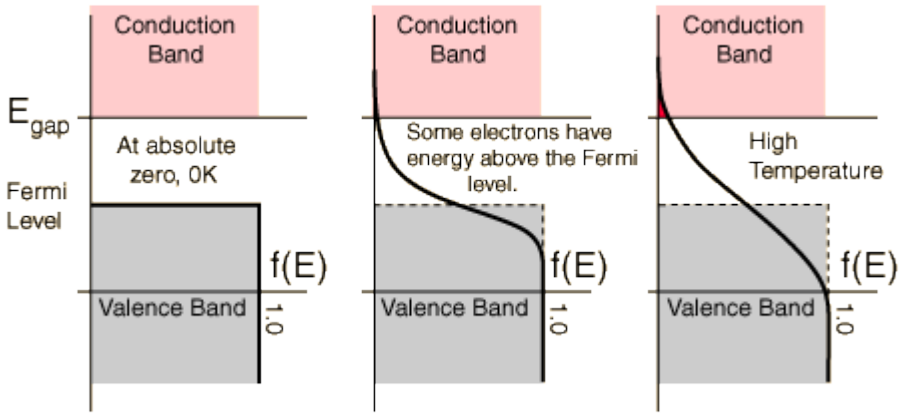

Figure 2.2: A schematic illustration of the change in electron occupation in the valence band and conduction band at absolute 0K and high temperature, with the Fermi level lying between the two bands and the Fermi-Dirac distribution function (f(E)) is directly affected by the temperature [44].

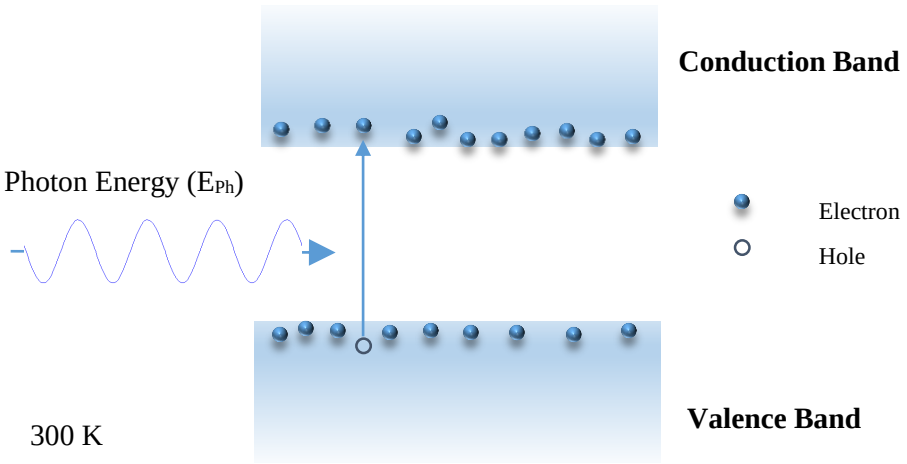

Figure 2.3: A schematic illustration of the absorption of photon energy by a semiconductor which generates an electron-hole pair. The process promotes the electron from the valence band to the conduction band, and the hole remains in the valence band.

A semiconductor crystal can absorb incoming light to induce an electronic reaction. Photons from the light can excite an electron and promote it from VB to CB. This process is called photoexcitation. Similarly, thermal energy can also excite an electron from VB to CB. This is the underlying principle in many devices available today, such as thermal detectors and photodiodes. In an excitation process, sufficient energy is required with a threshold equal to the E_G. Therefore, the energy of the photon must be equal or larger than the E_G of the semiconductor to induce a VB→CB transition. Figure 2.3 shows a schematic illustration of a photoexcited electron promoted from the VB to the CB, with the photon energy absorbed. In this process, the electron that got promoted to CB leaves behind an unbound state called a hole. Electrons are negative charge carriers and, similarly, holes are positive charge carriers. Both electrons and holes can carry electricity. In contrast with electrons, holes travel in the opposite direction and usually have a heavier effective mass and lower mobility. Electrons and holes are both energy carriers travelling in a gas-like motion. The density of the free charge carriers determines the amount of electrical current able to flow through the semiconductor.

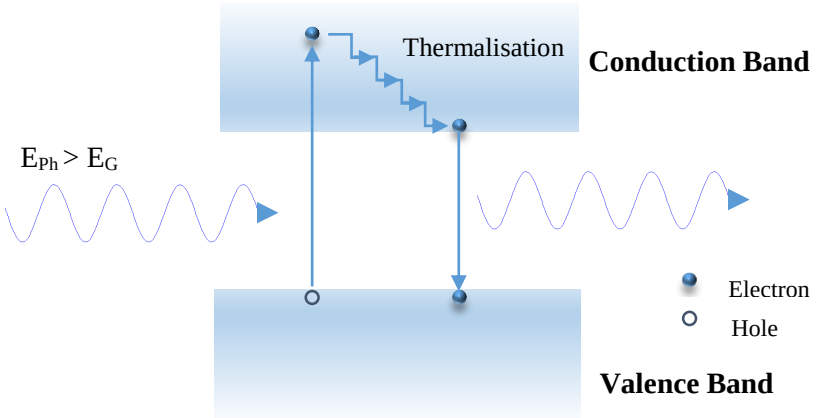

Figure 2.4: A drawing to illustrate the absorption of photon energy to promote an electron from the valence band the conduction band and the symmetric band-to-band radiative recombination process. Thermalisation of the excess energy from the absorbed photon happens orders of magnitude faster than the recombination process.

At room temperature, carriers are already present in the semiconductor due to the background thermal excitation. Hence, at 300K there are electrons occupying the CB,

as depicted in Figure 2.2. The associated carrier concentration, denoted by n_i, is called intrinsic carrier concentration. It is a temperature-sensitive parameter, as temperature has a direct impact on the thermal excitation processes prompting electrons from the VB to the CB. The density of electrons and holes in the conduction and valence bands can also be artificially modified by incorporating impurities into the crystal lattice. This is called doping and is a common method to influence the electronic parameters of semiconductor materials.

Photons with energy (E_{Ph}) higher than E_G are called supra-bandgap photons. When a supra-bandgap photon excites an electron to the CB, the electron occupies a high energy state in the CB. The electron then relaxes extremely rapidly through the energy states to the bottom of the CB, unless extracted otherwise. This process is called thermalisation, and is depicted in Figure 2.4. In the process, the descending electron dissipates the energy in the form of heat loss. Therefore, a part of the supra-bandgap photon energy is lost in the process. This is one of the major limitations in solar cell conversion efficiency.

The optical properties of the material determine the absorption probability of incoming photons. The absorption process occurs only when light propagates into the semiconductor crystal and the energy of incoming photons is transferred to electrons. Some incident light may get reflected off the surface or pass directly through the semiconductor. In the former case, the photon energy is lost via optical reflectivity, and could be minimised with anti-reflective coatings and/or surface texturing. In the latter case, the photon energy is lost via optical transparency of the semiconductor. This is because photons with energy below that of the E_G will not be absorbed. Hereafter they are called sub-bandgap photons.

The absorption coefficient (α), which is a wavelength-dependent parameter, is a factor that determines the absorptivity of a material. Figure 2.5 shows the absorption coefficient as a function of wavelength for various semiconductor materials. It illustrates that the strength of absorption at different wavelengths of light can differ

dramatically and all the material has an abrupt cut-off point at the bandgap energy wavelength.

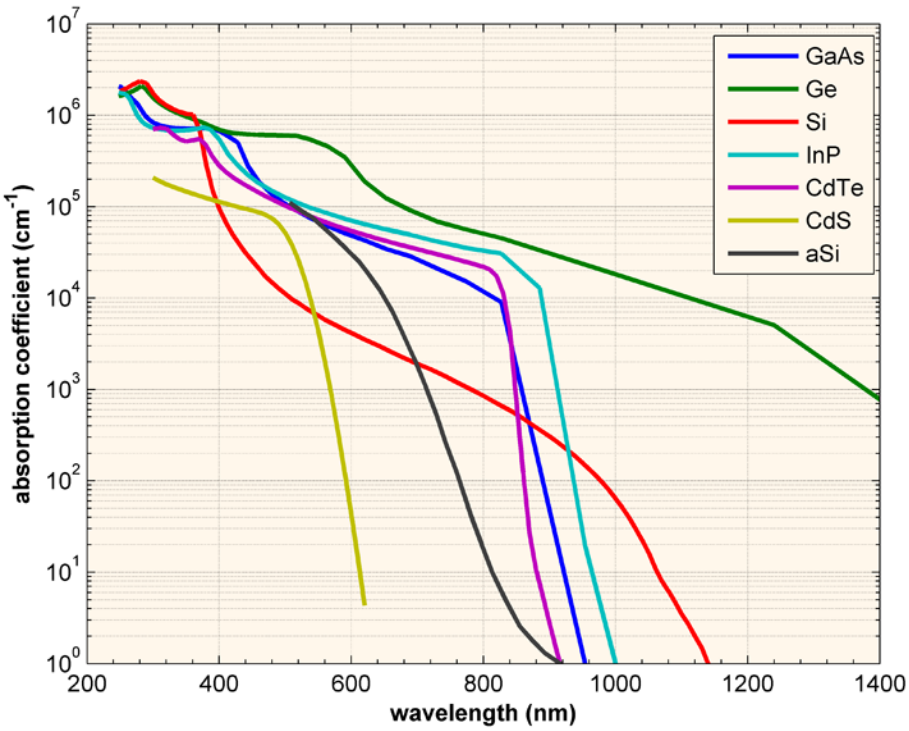

Figure 2.5: Absorption coefficient as a function of wavelengths for various semiconductor materials at 300 K displayed in logarithmic scale [45]. ***The cut-off point corresponds to the bandgap energy of the material.***

The light absorption (I) of a material can be calculated using the following equation:

$$I = I_0 \exp(-x\alpha) \qquad (3)$$

This is known as the Beer-Lambert equation, which is crucial in designing optical filters. For solar cells, it is used to determine the required thickness of the light-absorbing material. The equation states that light intensity at the point of contact (I_0) reduces exponentially with the distance into the material (x), which is dependent on the absorption coefficient (α). Blue light has a shorter wavelength and a higher α, and

is usually absorbed at the surface of the semiconductor. Red light has a longer wavelength and a lower α and is absorbed less strongly at the surface. To absorb the red light efficiently, the material needs to have a sufficient absorption length. Thus, in the design of solar cells, the semiconductor material needs to be thick enough to allow an optical pathway long enough for solar radiation to be efficiently absorbed. If the optical pathway is too short, red light may pass straight through the material without being absorbed. On a side note, surface texturing, which optically scatters the incoming light, not only reduces the surface reflection but also improves the probability of absorption by extending the length of the absorption path.

The equation can be used to find the number of electron-hole pairs generated (G):

$$G = \alpha N_0 \exp(-x\alpha) \qquad (4).$$

It is derived from the Beer-Lambert equation with the photon flux at the surface (N_0) substituted to I_0. The equation highlights an exponential reduction of generation of electron-hole (E-H) pairs with the distance into the material. Thus, the region at which the highest generation rate occurs is at the surface. In a solar cell design, the thickness of the absorbing layer should be determined by the value α. A material with high α will generally have a good absorption, and vice versa.

2.2 **The p-n Junction**

Doping is a common technique used in semiconductor crystals to change the material properties. It is a process where selected impurities are distributed in the semiconductor crystal. The impurity can either be a donor or an acceptor atom to form a negatively doped (n-type) or a positively doped (p-type) semiconductor, respectively. When a p-type semiconductor is connected to an n-type semiconductor, an electrostatic junction is formed. This is called a p-n junction, and is shown in Figure 2.6. In a p-n junction, the free-flowing excess carriers on both sides of the interface diffuse across the p-n junction. The electrons in the n-type semiconductor diffuse to

the p-type semiconductor, and the holes from the p-type semiconductor diffuse to the n-type semiconductor. As a result, a positive charge builds up in the n-type region and a negative charge builds up in the p-type region. The region around the p-n interface, where the electron-hole exchange happens, is depleted of free charge carriers and is called the depletion region. The build-up of opposite charges in the p- and n-regions gives rise to an electric field (E-field), which is a fundamental property in the design of solar cells.

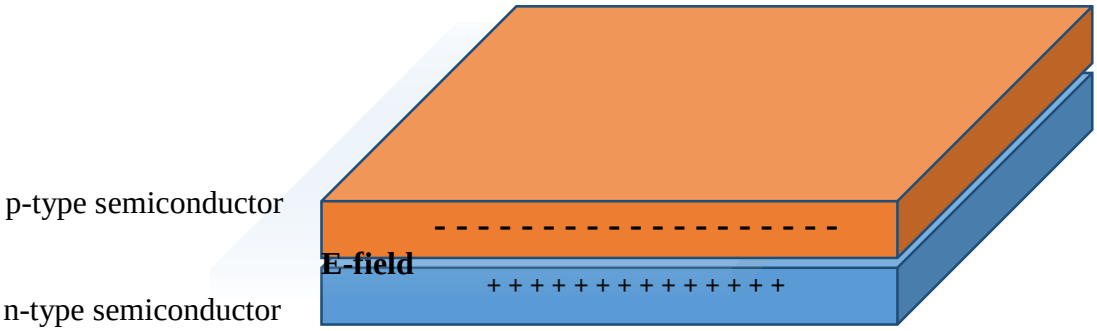

Figure 2.6: Formation of a p-n junction and the electric field at the interface, where the strength the E-field is directly dependent on the density of dopants in the p- and n-type semiconductor.

The E-field of the p-n junction is essential to the behaviour of charge carriers in the semiconductor. It enables a non-symmetric behaviour of the current flowing across the junction. The strength of the E-field is dependent on the dopant concentration on either side of the junction. Due to the E-field, electrons and holes will travel back to their region of origin, creating a drift current. This drift current acts in the opposite direction to the diffusion current presented above. Figure 2.7 depicts the direction of the drift and diffusion current of the electrons and holes. Under zero-voltage bias, the diffusion and drift currents balance out. However, under a forward or reverse bias, the E-field in the depletion region changes, and so does the depletion length. This breaks the equilibrium between the diffusion and drift currents and subsequently induces a net current flow through the p-n junction.

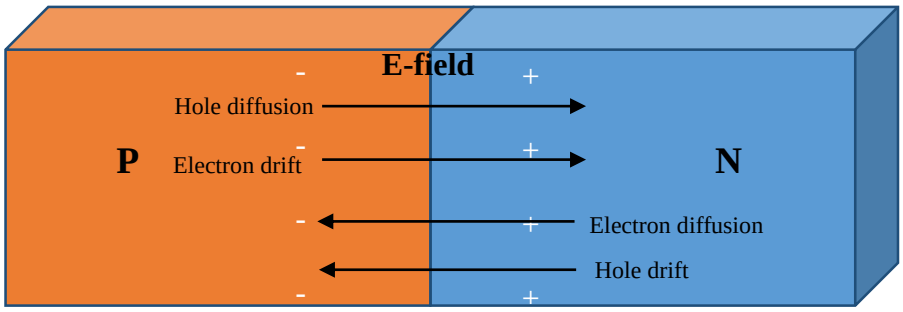

Figure 2.7: A schematic illustration of the diffusion and drift current across a p-n junction. The diffusion current is due to the difference in the distribution of free carriers on both sides of the junction. The opposing drift current is due to the presence of E-field.

Usually, a p-type semiconductor has its Fermi-level lying just above the VB. In contrary, an n-type semiconductor has its Fermi level lying just below the CB. Under thermal equilibrium, a p-n junction aligns the Fermi-levels, creating an offset of the CB and the VB on both sides of the p-n interface, but each band has an individual population that is internally in equilibrium. Figure 2.8(a) shows a band diagram of a p-n junction under equilibrium, and there is no net-flow of current as the drift and diffusion current cancel each other out. Figure 2.8(b) illustrates the effect of illumination, where the photoexcitation process generates additional E-H pairs, which are separated by the E-field. Electrons gets swept to the n-type region and holes gets swept to the p-type region. This is termed photogeneration. If the photogeneration continues to generate E-H pairs but they are prevented to leave the solar cell, more electrons will travel to the n-type region and more holes will travel to the p-type region. This pulls down the VB of the p-side, which reduces the in-built E-field that normally acts as a barrier to the diffusion current. Gradually, enough electrons in the n-region and holes in the p-region breaks the equilibrium between the drift and diffusion current. As a result, there is no barrier to prevent the diffusion current of electrons and holes across the junction. Therefore, a resultant current flow is enabled.

In solid-state physics, the quasi-Fermi level describes the population of electrons separately in the CB and the VB, when their populations are displaced from equilibrium, depicted by the red dotted line in Figure 2.8. The built-in E-field in a p-n junction is equivalent to a built-in voltage. Illumination creates a displacement of the

electron population in the system, which determines the separation of electron and hole quasi-Fermi level in the CB and VB of the p-n junction. When the built-in voltage becomes zero, the photocurrent is the highest, similar to a forward bias situation. Overall, the built-in voltage is able to generate a current flow which is activated by a photo-induced process, it is classed as a photovoltaic phenomenon. The photo-generated current together with the voltage in the p-n junction give rise to the output power.

In a measurement condition, where the solar cell is electrically connected and the p-n junction is biased, such that the photocurrent is opposed by a diffusion current, the strength of the built-in voltage can be obtained. When the photocurrent, is balanced by the diffusion current, the net current becomes zero, which is the point of open-circuit voltage. This is the maximum voltage available from the p-n junction, which is determined by the separation of the quasi-Fermi level. The effect of quantum dot thermal-coupling could reduce this separation, which will be explained in later chapters.

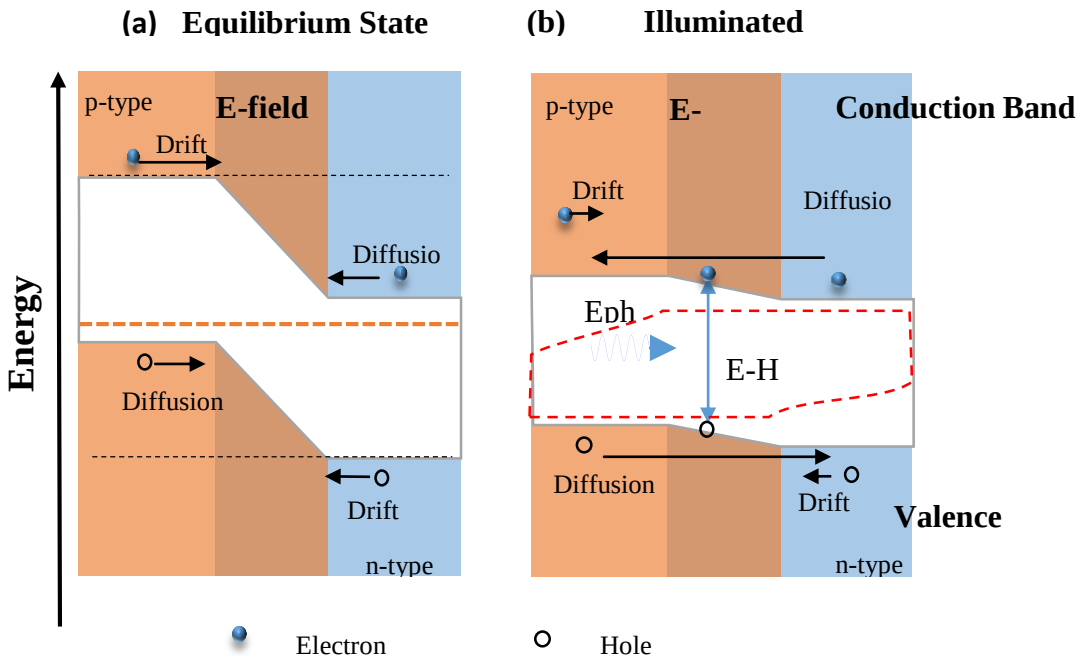

Figure 2.8: Band diagram of the p-n junction illustrating the effect of E-field on electron-hole pairs, preventing current flow. Under illumination, the E-field reduces which permits diffusion

current. The red dotted line is the quasi Fermi-level. Illumination creates a split in the quasi-Fermi level which determines the voltage of the cell.

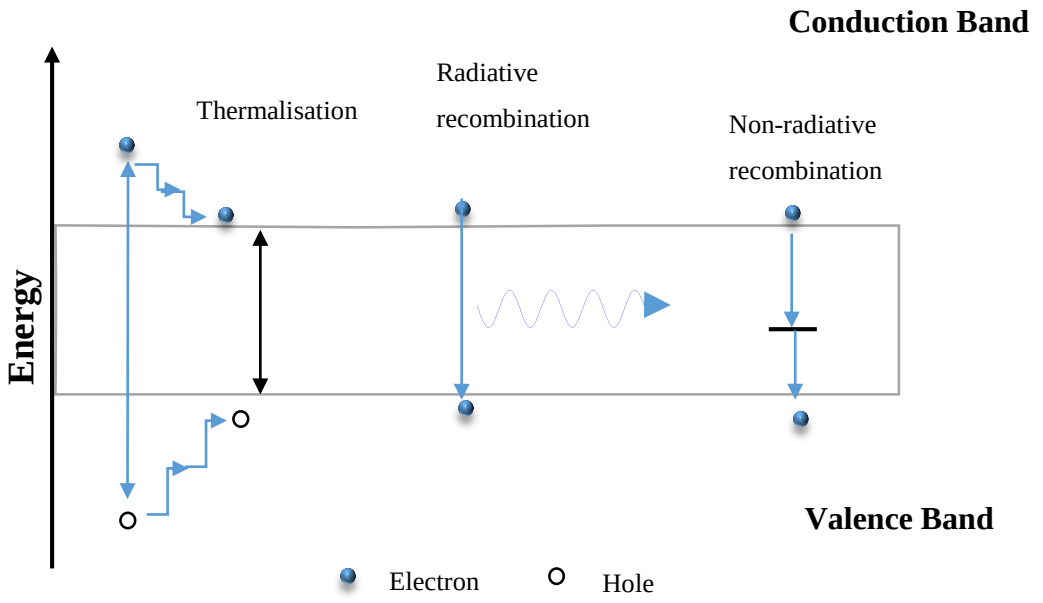

Figure 2.9: A schematic diagram showing 3 different loss mechanisms which could affect the maximum achievable photocurrent of a solar cell (i.e. thermalisation, radiative and non-radiative recombination).

The photocurrent is a result of the photogeneration of E-H pairs, which in turn results from photoexcitation. However, the equation would be incomplete without accounting for recombination processes. They are processes where electrons recombine with holes, losing the previously absorbed energy. Recombination is considered as a loss mechanism, along with thermalisation, where absorbed photon energy is dissipated, losing the contribution to the photocurrent. The two types of recombination are radiative and non-radiative (NR) recombination. They are detailed in later sections of this chapter. In brief, a radiative recombination involves a photon emission upon the recombination of an electron with a hole. However, a NR recombination involves energy dissipation through vibrations in the crystalline lattice resulting in thermal losses. In the quantum mechanical description, these are known as phonons. Both radiative and NR recombinations, along with thermalisation, are considered loss mechanisms in the photogeneration process. Figure 2.9 shows a schematic diagram illustrating the possible pathways for carriers in the band diagram

of a p-n junction. Photoexcited carriers can recombine via radiative or NR pathways before extraction. Only the extracted carriers contribute to the photocurrent. Although the E-field that separates the E-H pairs helps to minimise recombination, the loss mechanisms can occur anywhere in the P-N junction.

2.3 **The Diode Equation**

Because standard solar cells use a p-n junction, it is typically treated as an ideal diode and the classic diode equation can be used. The diode equation determines the current as a function of voltage. It can be used to solve the properties in the depletion region and calculate carrier concentrations. Semiconductors can be analysed in a thermal equilibrium state where no interference with light intensity is allowed. This is called the dark current measurement. The parameters give information about the band diagram of the semiconductor. On the other hand, a solar cell measurement can be carried out under steady state where constant voltage or light intensity is applied. Therefore, the measured parameters allow the conversion efficiency of the solar cell to be calculated.

It should be reminded here that the terms *photogeneration* and *photocurrent* refer to the amount of carriers generated by photoexcitation and the amount of carriers extracted from the solar cell, respectively. The photocurrent is a net difference between the photogeneration and recombination rates, which are accounted in the derivation of photocurrent in the diode equation. In order to calculate these rates, there are some assumptions made throughout the calculation: the semiconductor solar cell is analysed under thermal equilibrium, steady state and transient state.

The ideal diode equation for a photovoltaic device is derived from the considerations of the depletion region. The E-field strength is calculated from the dopants concentration in the p- and n-regions of the semiconductor using the Poisson's equation. This equation determines the electrostatic potential depending on the charge density. The charges are divided into four components: hole density *(p)*, electron density *(n)*, acceptor atom density *(N_A)* and donor atom density *(N_D)*. The following

equation summarises the gradient of the E-field (E) strength over the depletion region [46]:

$$\frac{dE}{dx} = \frac{\rho}{\varepsilon} = \frac{q}{\varepsilon}\,(p(x) - n(x) - N_A^- + N_D^+) \qquad (5)$$

It is equal to the charge density (ρ) over the material permittivity (ε). q is the elementary charge. The charge density is equal to the difference in the electron and hole density, minus the difference between the donor atom and the acceptor atom density, multiplied by the elementary charge. The E-field strength can be directly calculated if the charge densities in the p-n junction are known. For the ideal diode derivation, N_A is assumed constant in the p-region and zero in the n-region. Similarly, N_D is assumed constant in the n-region and zero in the p-region.

Next, to consider carrier dynamics, the transport equation is taken into account. The carrier transport is governed by the drift and diffusion current, therefore the electron current density (J_n) and the hole current density (J_p) are the net differences between the drift and diffusion current for electrons and holes, as summarised below:

For electrons, $$J_n = \mu_n q n E + D_n q \frac{dn}{dx} \qquad (6)$$

For holes, $$J_p = \mu_p q p E - D_p q \frac{dp}{dx} \qquad (7).$$

On the right hand side of the equations, the first term in each equation represents the drift current and the second term represents the diffusion current. The drift current is simply the product of the carrier mobility (μ), q, n and E. The diffusion current is the product of the carrier diffusivity (D), q and the rate of change of n over distance (x). The assigned subscript shows the type of carrier that is concerned (n for electrons and p for holes). Since the E-field is expected to sweep the carriers out of the depletion region, it is assumed that the depletion region has no free carriers. To calculate the

photocurrent, the rate of generation and recombination is taken into account. This employs the continuity equation where the movement, generation and recombination of the carriers are put together. Again, electron and holes are treated separately. They are shown in the following equations:

$$\frac{dn}{dt} = \frac{1}{q}\frac{dJ_n}{dx} - (U - G) \qquad (8)$$

$$\frac{dp}{dt} = -\frac{1}{q}\frac{dJ_p}{dx} - (U - G) \qquad (9).$$

The rate of change in carrier density is equal to the rate of change of the current density (J) over x, minus the difference between the recombination rate (U) and the generation rate (G). Under thermal equilibrium and steady state conditions the carrier concentrations do not change with time so that:

$$\frac{dn}{dt} = \frac{dp}{dt} = 0 \qquad (10).$$

Therefore, equation (8) and (9) can be rewritten as:

$$\frac{1}{q}\frac{dJ_n}{dx} = U - G \qquad (11)$$

$$\frac{1}{q}\frac{dJ_p}{dx} = -(U - G) \qquad (12).$$

Furthermore, solving equation (5) for the depletion region gives the built-in voltage (V_0) in relation with N_A and N_D (the solutions can be found elsewhere [46]):

$$V_0 = \frac{kT}{q}\ ln\frac{N_A N_D}{{n_i}^2} \tag{13}$$

This forms the component for the diode equation. k, T and q are the Boltzmann constant, temperature and elementary charge constant, respectively. The carrier concentration remains constant, equal to n_i, under dark conditions and contributes to the J_0. The dark current arises from recombination events, which is a diode component itself and is distinguished from the photocurrent diode. It is inversely proportional to the material quality of the device. The equation here provides the diode equation for the dark current which describes the current as a function of voltage:

$$J = J_0 \left[exp\left(\frac{qV}{kT}\right) - 1 \right] \tag{14}$$

Under illumination, the carrier concentration would increase due to the photogeneration process. Therefore, the diode equation for a solar cell contains the dark current component and the photogeneration component. With rearrangement to the equation, the diode equation for a solar cell becomes:

$$J = J_0 \left[exp\left(\frac{qV}{mkT}\right) - 1 \right] - J_l \tag{15}$$

This equation describes that the total current density (J) is the difference between the saturation current (J_0) and the light-generated current density (J_l) components. In fact, the exponential term usually is much greater than 1 when voltage is higher than 0.1V, hence the -1 term can be neglected. In addition, an ideality factor (m) is included to better suit the equation in practice by accounting for other types of recombination. It can be seen from equation (15) that the photocurrent diode curve is a superposition of the dark current diode curve.

Although J_l is usually the correct term to use in the ideal diode equation for solar cell measurements, in practice the current is externally measured in short-circuit conditions. This is called the short-circuit current density (J_{SC}). If the carriers diffusion lengths (L_n) and (L_p) are known, J_{SC} can be approximated using this equation:

$$J_{SC} = qG\left(L_n + L_p\right) \qquad (16)$$

To calculate the power output efficiency of a solar cell, the open-circuit voltage (V_{OC}) is needed. This can be calculated using the following equation:

$$V_{OC} = \frac{mkT}{q}\ln\left(\frac{J_L}{J_0}\right) \qquad (17)$$

Empirically, both J_{SC} and V_{OC} can be found from electrical measurements under illumination, described in Chapter 3. Moreover, Equation (17) reveals that the ratio between J_L and J_0 has an impact on the V_{OC}. Higher J_0 can reduce the V_{OC}, which reflects on the effect of material quality on the built-in voltage. Another parameter that determines the output power of the solar cell is the fill factor (FF). It is defined as the ratio of the maximum power from the solar cell to the product of J_{SC} and V_{OC}. Graphically, the more "square" the JV curve is, the higher the FF. In short, it is determined by the series, shunt resistance and ideality factor of the solar cell. Finally, the solar cell conversion efficiency (ɳ) is the product of J_{sc}, V_{oc} and FF over the input power density of illumination (P_{in}):

$$\eta = \frac{J_{SC}\,V_{OC}\,FF}{P_{in}} \qquad (18)$$

2.4 **Recombination Processes**

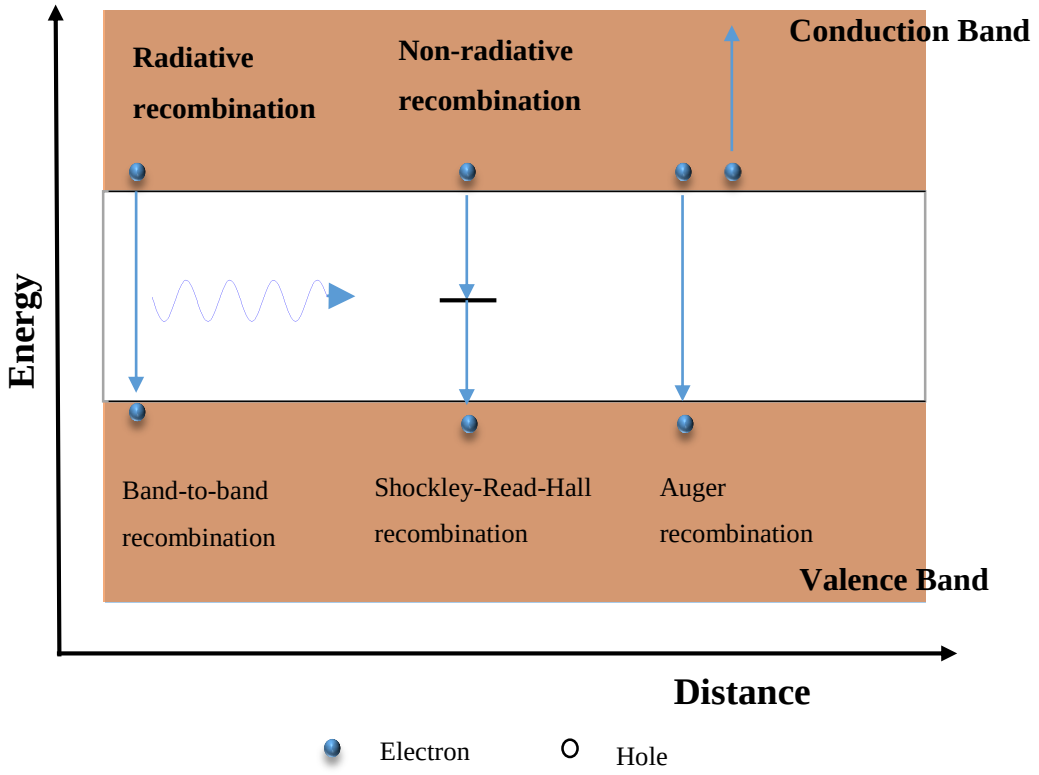

Figure 2.10: A schematic illustration of the different types of recombination pathway that could occur in a semiconductor, i.e. band-to-band, Shockley-Read-Hall and Auger recombination, where the ideality factors are 1, 2 and 2/3 respectively.

To understand the dynamics in solar cells, recombination processes cannot be ignored. Unfortunately, not every photoexcitation successfully contributes to the final J_{SC}. Usually, photogenerated E-H pairs are separated by the E-field and travel to their respective terminals, then the carriers exit the solar cell by channelling through the electrode contacts. Throughout this process, there is a tendency for electrons to recombine with holes along the photocurrent path. The recombination events lead to some excited electrons to fall back down from the CB to the VB, losing the absorbed energy. This could happen immediately after a photoexcitation event unless the carrier is successfully extracted from the solar cell. Therefore, only carriers successfully extracted from the p-n junction can directly contribute to the J_{SC}. Recombination processes are divided into two pathways: radiative and NR recombination. They

compete with each other. The characterisation of recombination pathways is used to assess the quality of a solar cell. It will be included in some of the discussions of the experimental results.

Figure 2.10 shows a schematic illustration of the different types of recombination pathway. A radiative recombination process occurs when an electron in the CB directly combines with a hole in the VB. It releases its energy by photon emission after the downward transition. This recombination mechanism dominates in perfect crystalline quality direct bandgap semiconductors. On the other hand, there are two types of NR recombination mechanisms, namely the Shockley-Read-Hall (SRH) recombination process and the Auger recombination process. In the SRH recombination process, a carrier gets trapped on an energy state within the bandgap due to a defect in the crystal lattice. The absorbed energy is lost via phonon-emission. In Auger recombination, an electron and a hole recombine but the energy is transferred to another electron in the CB. The electron relaxes through thermalisation, rapidly dissipating its excess energy in the form of heat. These are depicted in Figure 2.9. Comparing the two types of NR recombination, the SRH one is a 1-particle reaction whilst the Auger one is requires 3 particles. Since SRH recombination is a defect-assisted recombination, it dominates in semiconductor with poor crystal qualities. On the other hand, Auger recombination dominates in semiconductors with very high carrier concentrations; therefore the effect will be prominent under high concentration illuminations.

Furthermore, there is no immediate way to extract the rates of the two types of NR recombination, but experimental data may indicate which type is the dominant one. This is indicated by the ideality factor m in the ideal diode equation in equation (15). An m value closer to 2 indicates that the SRH recombination is dominant. However, m value closer to 2/3 indicates that the Auger recombination is dominant [47].

2.5 **Intermediate Band Solar Cells**

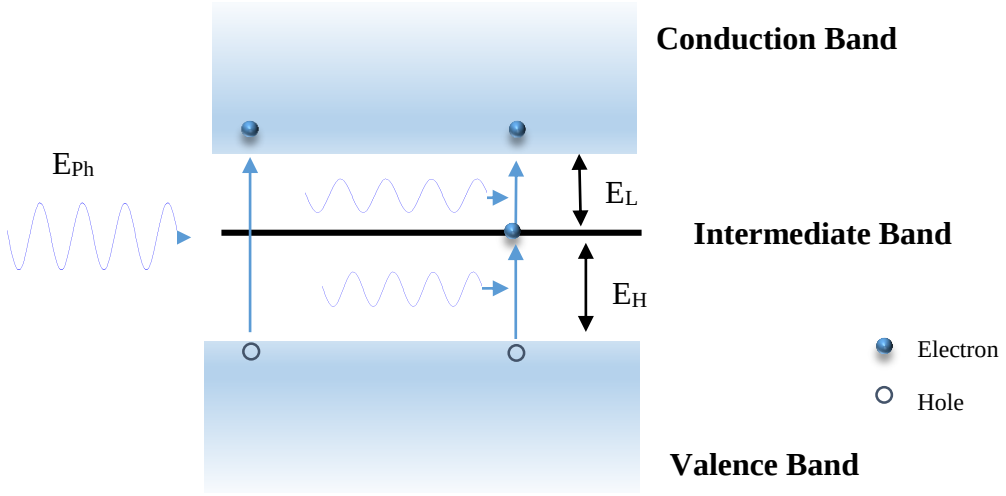

Figure 2.11: Schematic diagram showing possible photoexcitation pathways in the IBSC in addition to the single junction photoexcitation mechanism. The three pathways are valence band → intermediate band, intermediate band → conduction band and valence band → conduction band [48]

In the IBSC concept, an IB is introduced into the bandgap between the VB and the CB. It acts like a stepping stone for two sub-bandgap photons to be absorbed. Figure 2.11 shows a schematic diagram of the IBSC model, which illustrates a simple three level band for possible photoexcitations to occur. The energy difference between VB and IB is denoted E_H, and the energy difference between IB and CB is denoted E_L. It should be reminded here that the IBSC concept centralises on the two-step photoexcitation event. The first sub-bandgap photon ($E_{Ph} > E_H$) excites the electron from the VB to the IB followed by a second sub-bandgap photon ($E_{Ph} > E_L$) which promotes the electron from the IB to the CB. This two-step transition creates an advantage above that of the single-junction VB→CB transition. Hence, the sub-bandgap energy photons will not be lost through optical transparency, but collected to generate additional photocurrent to enhance the performance compared with a single-junction solar cell. It is analogous to a MJSC operation where different portions of the solar spectrum are targeted for absorption.

In ideal conditions, the voltage output of a QD-IBSC is still determined by the bandgap of the semiconductor host material. Therefore, additional photocurrent production without compromising the voltage could lead to a conversion efficiency that surpasses the Shockley-Queisser limit. This is the paramount principle of IBSCs.

The feasibility of the IBSC concept requires that the following ideal conditions are approached: (1) the NR recombination transition is forbidden, (2) carriers mobilities are infinite with no ohmic losses, (3) no carrier can be extracted from the IB unless optically pumped and (4) the IB must be partially filled with electrons for the second photoexcitation event to occur.

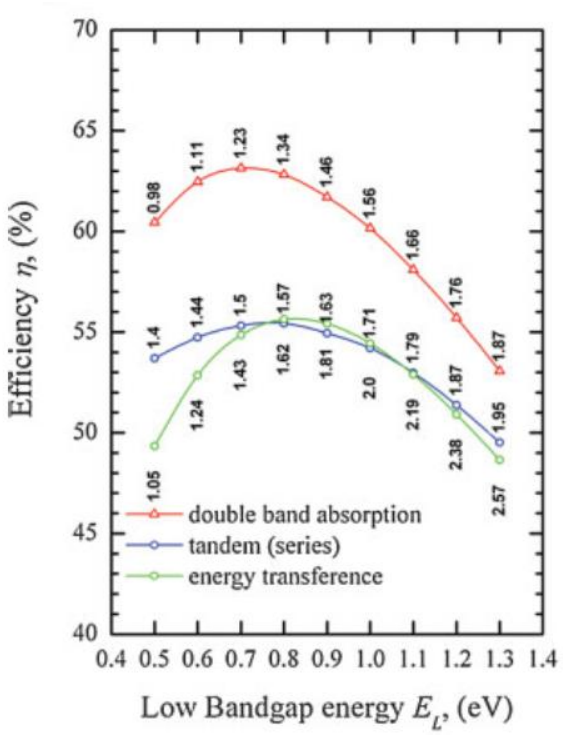

Figure 2.12: Efficiency of IBSC as a function of lower bandgap energy in the IB to CB transition as shown in red (double band absorption), and the efficiency of the same bandgap configuration in MJSC as shown in blue. The green line represents the efficiency of energy transference of the intermediate band [49].

The optimal bandgap and sub-bandgaps for IBSCs have been simulated by Martí and Luque to produce the highest theoretical conversion efficiency [49]. Figure 2.12 shows the change in the IBSC efficiency as a function of low bandgap energy (E_L) for

IB → CB transition in a double band absorption, as shown by the red line. A maximum point is reached at 1.24 eV when the E_L energy is 0.71eV. Therefore, the three optimal energy transitions for IBSCs are 1.95 eV (VB → CB), 1.24 eV (VB → IB) and 0.71 eV (IB → CB) [50]. The blue line shows what the efficiency would have been if this bandgap configuration was applied to two single-bandgap solar cells connected in series, which illustrates a reference point to the effectiveness of IBSC. Finally, the green line corresponds to the limiting efficiency of IBSC operating under energy transfer, such as when the electron in the IB is transferred to the CB via impact ionization. This way is less efficient than the two-photon absorption mechanism that is profoundly the key IBSC operation principle [49].

In general, a transition rate depends upon the strength of the coupling between the initial and final state of a system and upon the number of ways the transition can happen (i.e., the density of the final states). In many physical situations, the transition probability follows Fermi's rule. A transition will proceed more rapidly if the coupling between the initial and final states is stronger. This coupling term is traditionally called the "matrix element" for the transition. Due to the conservation of momentum accounted for in Fermi's rule, a high density of states within the IB is desirable for strong optical transition.

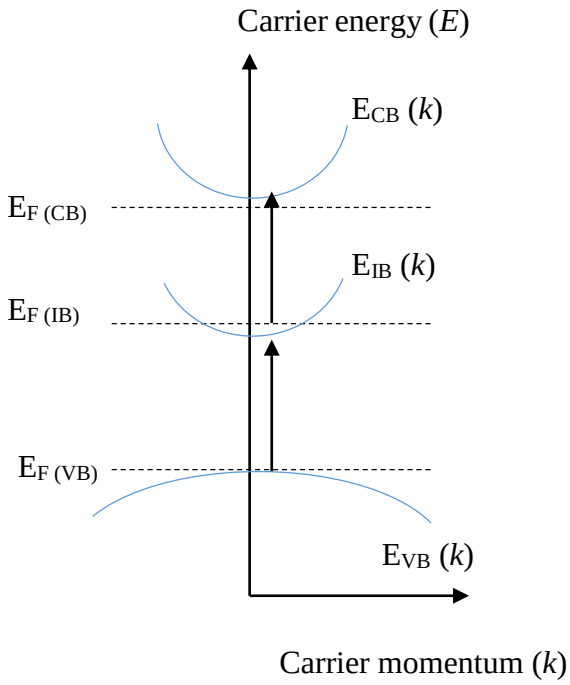

Figure 2.13: Allowed optical transitions with conservation of energy and momentum with three possible quasi-Fermi levels. Regenerated from Ref [51].

Absorption via the IB takes into account the integration of all the possible carriers that can participate in an optical transition while conserving energy and momentum. Figure 2.13 shows a schematic illustration of an energy-momentum diagram of an ideal IBSC operation with the ideal quasi-Fermi energy level $E_{F(CB)}$, $E_{F(IB)}$ and $E_{F(VB)}$ labelled. Ideally, the voltage extracted from the solar cell is the difference between the CB and VB quasi-Fermi level at the n- and p-contacts, respectively. In order to generate an efficient IBSC such that the minima of the CB and IB is aligned with the maxima of the VB, direct bandgap QD and host materials are used for this study, i.e. InAs and GaAs. To consider the effect of introducing IB between the VB and CB, the impact of the absorption coefficient on the carrier generation in the VB→IB and IB→CB transition is considered. Here, the carrier generation rate for the VB→CB transition ($G_{VB\rightarrow CB}$) is expressed in the assumption of completely filled CB and VB [52]:

$$G_{VB\rightarrow CB}(x) = \int_0^{\infty} \alpha_{VB\rightarrow CB}\, w_{VB\rightarrow CB}\, F_s\, F_D\, dE \qquad (19),$$

where α is absorption coefficient as a function of the photon energy E; w is the weighted absorption probability; F_s is the incident photon flux density and F_D is the decay factor of incident photon flux at position x. The generation rate for the IB→CB and VB→IB transitions can be written as [53]:

$$G_{IB\rightarrow CB}(x) = \int_0^{\infty} \alpha_{IB\rightarrow CB}\, f_I\, w_{CB\rightarrow IB}\, F_s\, F_D\, dE \qquad (20)$$

$$G_{VB\rightarrow IB}(x) = \int_0^{\infty} \alpha_{VB\rightarrow IB}\, (1 - f_I)\, w_{VB\rightarrow IB}\, F_s\, F_D\ \, dE \qquad (21).$$

The equations show similar components to that of the generation rate for VB→CB transition in equation (19). The component f_I is the occupation probability. The equation points out that the optical transition from IB to CB requires a state in the IB to be filled and an empty state in the CB. Similarly, the optical transition from the VB to the IB requires an empty state in the IB. Therefore the IB must support transitions both into and out of it.

Carriers in the IB should have a sufficient lifetime, which helps to keep the IB states occupied. This allows the second photoabsorption event to take place. The IB→CB optical transition could only be possible when there are occupied states in the IB, and conversely, the VB→IB optical transition requires a state in the IB to be unoccupied.

The electrostatic profile of IBSCs strongly depends on the electron density in the IB and the carrier generation/recombination rates through it. To see the impact of this on the p-n junction, the Poisson equation is employed. It considers the charge density distribution within the IB material, which can be written in the form [54]:

$$\frac{d^2\psi}{dx^2} = \frac{q}{\epsilon}(p - n_C - n_I + N_D^+ - N_A^-) \qquad (22),$$

where ψ is the electrostatic potential; n_C and n_I are electron densities in the CB and in the IB; p is the hole density in the VB. The charge density distribution in the p-n junction now contains the electron density of the IB.

Since radiative recombination is also possible via the IB, the carrier generation pathway now competes with this new recombination pathway via the IB. Hence, the interband transitions must be optimised to allow constant elevation of energetic electrons to the CB to produce a large photocurrent. Applying the current continuity equations for electrons and holes under steady state gives:

$$-\frac{1}{q}\frac{dJ_n}{dx} = G_{CV} - R_{CV} + G_{CI} - R_{CI} \qquad (23)$$

$$\frac{1}{q}\frac{dJ_p}{dx} = G_{CV} - R_{CV} + G_{IV} - R_{IV} \qquad (24)$$

where J_p and J_n are electron and hole current densities, and G and R are generation and recombination where the accompanying subscripts $_{CV}$, $_{IV}$ and $_{CI}$ represent the CB→VB, IB→VB and CB→ IV transitions, respectively. The continuity equation treats the IB as an energy level, not a band, similar to trap levels. Therefore, carriers in the IB do not travel through the IB.

Recombination rate and absorption efficiency are the important factors that determine the IBSC conversion efficiency. The recombination rates for radiative recombination processes are as follows [55]:

$$R_{CV} = \beta_{CV} \exp\left(\frac{\mu_C - \mu_V}{K_B T}\right) - 1 \quad (25)$$

$$R_{CI} = \beta_{CI} \exp\left(\frac{\mu_C - \mu_I}{K_B T}\right) - 1 \quad (26)$$

$$R_{IV} = \beta_{IV} \exp\left(\frac{\mu_I - \mu_V}{K_B T}\right) - 1 \quad (27)$$

Using the same method as when deriving the generation rate for the VB→CB transition, the sub-bandgap photocurrent generation can be written in terms of the net carrier generation rates via the IB:

$$G_{IB}^{*} \equiv G_{CI}(x) - R_{CI}(x) = G_{IV}(x) - R_{IV}(x) \quad (28)$$

It can be seen that for optimal photogeneration via the IB, the IBSC requires a high generation rate for the IB→CB transition with a low recombination rate. This is equally important for the VB→IB transition. Optimising the dynamics of the transitions is one of the keys in IBSC. It involves work in modifying the carrier lifetimes in the IB and suppressing recombination effects [56]. Also, it requires the two transition pathways to be in dynamic equilibrium. Furthermore, the VB, IB and CB must also be sufficiently separated to have three quasi-Fermi levels. It is perhaps one of the most fundamental constraint facing IBSCs that still requires much attention. In addition, recent years have seen proposals which aim to tackle the carrier lifetime constraint, such as type-II QD configurations and ratchet IBSCs [57].

2.6 **Semiconductor Quantum Dots**

Much efforts are directed towards discovering new materials to make suitable photovoltaic cells with high conversion efficiency. There are many emerging materials that can be used in the photovoltaic field. They range from perovskite [58] to dye-

sensitised solar cells [59] as seen in Figure 1.3. However, they offer no flexibility in targeting a large spectral coverage like the MJSC. Nanomaterials can display new quantum phenomena, resulting in different optical, electrical and magnetic properties compared with their bulk counterparts.

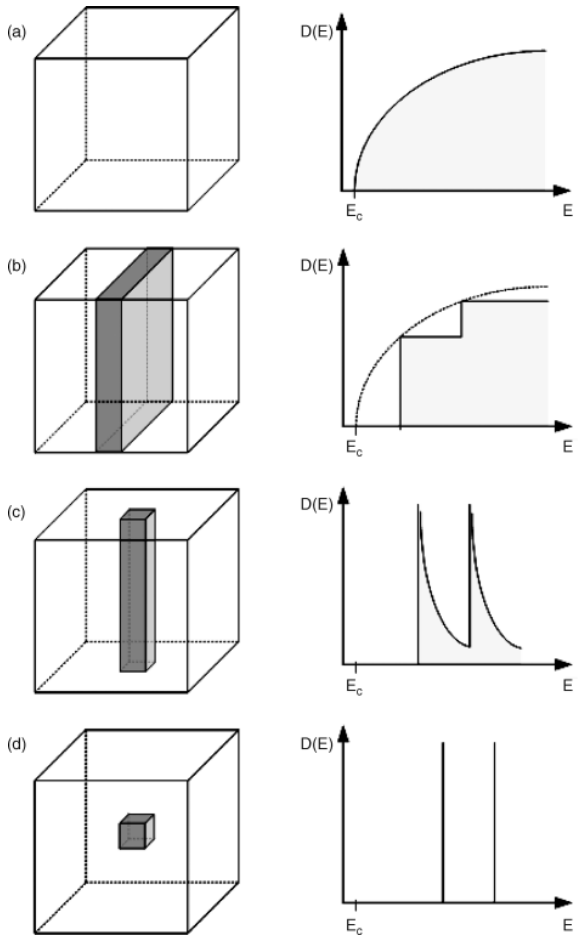

Figure 2.14 A schematic illustration of different material dimensions with the corresponding profiles of energy levels (a) bulk, (b) 2D, (c) 1D and (d) 0D.

While the motion of electrons in a bulk semiconductor material is permitted in all three (x, y and z) directions, the flow of electrons in the crystal lattice becomes restricted when dimensions are reduced. Figure 2.14 shows a schematic illustration of the evolution of the density of states as the object dimension reduces. The 3D, 2D and 1D materials with their corresponding density of states are shown in Figure 2.14 (a),

(b) and (c), respectively. As the dimension of the material is reduced, the density of states changes. This determines the way carriers can occupy the material.

A QD is a nanomaterial described as having zero dimension. This is a special case due to its size being smaller than the de Broglie's wavelength. Consequently, electrons are confined in a 3-dimensional potential well. As a result, the density of states in a QD becomes discrete, displaying atomic-like properties. Hence it is called an artificial atom. The spatial restriction on the displacement of carriers inside the quantum dot helps to localise the electrons. The photoexcited carriers are then be called excitons. An exciton is a quasi-particle consisting of one positive and one negative charge which resembles a hydrogen atom. An electrostatic interaction between the oppositely charged particles lead to an attractive force that tends to keep the electron and hole together. Although QDs have a relatively high recombination rate due to the spatial confinement of electrons and holes, the attractiveness of QDs is due to their sharp density of states. The confinement that gives rise to this sharp density of states results in a strong-light-matter interaction [60].

Another attractive feature of QDs is the adjustability of their optical and electrical properties simply by modifying their size. The energy state spectral of a semiconductor QD is determined by the depth of the potential well. Hence, QDs of different sizes emit a different photon energy. This makes the colour emission of QDs relatively easy to tune. This feature alone is desirable for high efficiency light-emitting diodes [61-62], liquid crystal displays [63-64], infra-red photo-detectors [65] and laser devices [66]. QDs have a proven track record in applications in optoelectronics. Furthermore, the photophysical properties of QDs, which makes biomolecular-tagging possible, has been applied to biological applications [67]. The ability to control the optical properties by changing the QDs size offers a valuable way to design a solar cell with a desirable absorption coverage.

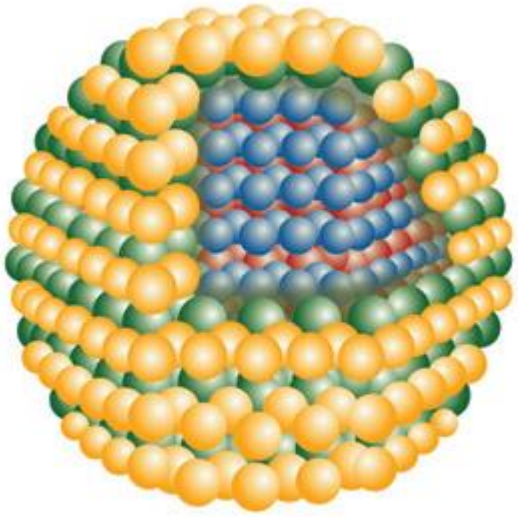

Figure 2.15 A schematic illustration of a quantum dot showing a core material (blue and red) enwrapped in a barrier material (green and orange).

Figure 2.15 shows a picture of a quantum dot structure. Solid-state semiconductor QDs are achieved by enwrapping a lower bandgap QD material with a higher bandgap host material. The difference in the bandgap energies generates an offset in the CB and VB of the QD and the host material. The presence of the potential well gives rise to discrete energy states of the CB and VB in the QD. The states in the CB are strongly connected among themselves by thermal infra-red photons. Usually, the lowest energy state in the potential well is called the ground state (GS) and the next energy level above is called the first excited state (FES), and so on. QD energy states exhibit very prominent phonon bottleneck effect [68]. That is a multi-particle mechanism that impedes the relaxation of excited electrons into lower energy states via phonon scattering. In addition, the phonon bottleneck effect makes the radiative recombination process between the CB and the IB potentially dominant.

Primarily, semiconductor QD is a favourable material to fabricate IBSCs because the discretely confined states in the QD can be used as IB states. The three-dimensional potential in the QD can isolate the IB from the CB through a true null density of state. This makes QDs suitable for other types of solar cell concepts. As mentioned above, QDs are also suitable for hot carrier solar cells [69] and multiple-exciton generation

[18]. QDs suppresses lateral migration of carriers and therefore are less susceptible to surface recombination in a solar cell. Furthermore, QDs of a specific configurations (i.e. type-II) have a sustainable optical excitation, and hence make a promising engineering prospect for solar cells. For this reason, QD-IBSCs have received much attention as a candidate for establishing high conversion efficiencies. The proper design of the QD superlattice aims to take advantage of the phonon bottleneck effect to make radiative recombinations dominant and to achieve strong photon absorption. It is a desirable phenomenon when manufacturing a QD-IBSC where rapid NR recombinations to the QD energy level must be avoided.

2.7 **Summary**

This chapter reviewed some of the operating principles of solar cells. The fundamental properties of the p-n junction have been described with equations. The rise of the depletion region from the p-n junction makes the extraction of a photocurrent possible. The E-field is responsible for separating the E-H pairs upon photo-excitation, at the same time, it is also responsible to the current flow in the solar cell. The collection of photo-excited carriers gives rise to the photocurrent. There are also possible recombination pathways, which affect carriers. They are radiative band-to-band recombination, Shockley-Read-Hall recombination and Auger recombination. The concept of IBSC has also been reviewed. The introduction of the IB into the solar cell widens the absorption coverage of low-energy photons and reduces waste of sub-bandgap photons. To fabricate such solar cells, nano-size QD materials are the most suitable candidate to host the IB due to their discrete density of states. In the next chapter, the experimental section will describe the techniques used to insert the QDs into the solar cell to form QD solar cells. The QD solar cell is used to exhibit the IBSC concept.

Chapter 3

Experimental Methods

In order to use semiconductor QDs as an absorber material in the structural design of the solar cell, it must be embedded within the p-n junction. For QD solar cells, the host material for the QD should possess a bandgap energy larger than the bandgap of the QD material. The sub-bandgap energies such as the GS and the First Excited State (FES) are determined by the QD. The energy states of the QD, usually the GS, are used as the IB. For a strong IB, in terms of optical pumping power, an array of coherent QDs is needed so that the energy states can be close enough to each other to form a band with a high density of states. In order to fabricate the QDs within the host semiconductor, a bottom-up approach has been used via a crystal growth technique, called molecular beam epitaxy. It is achieved via solid-source growth in a chamber under ultrahigh vacuum. Examples of novel nanostructures grown by molecular beam epitaxy include quantum rings [70-72], nanowires [73-74] and nanocolumns [75]. This leads to possible new designs in optoelectronic devices such as lasers, photodetectors and modulators.

In this chapter, an introduction to UCL Molecular Beam Epitaxy (MBE) system is given. This section will describe the growth facilities and components, such as monitoring devices, necessary to grow III-V semiconductor QD structures. Here, the mechanism of the QD growth will be discussed, followed by the structural outline of

the QD solar cell design. The following section will describe the fabrication methodology of QD solar cell devices. It will detail the different stages of the process. This includes acid cleaning, photolithography, etching and metallic contacts deposition. Finally, the third section will describe the method used to characterise QD solar cell devices, and the tools involved to obtain imaging, electrical and optical characterisations.

3.1 **Molecular Beam Epitaxy**

3.1.1 Introduction

In Molecular Beam Epitaxy (MBE), the success in achieving a finely grown crystal is determined by the mean free pathway of the constituent elements. Therefore, the MBE machine is designed to create long mean free path for the molecular beam fluxes. The beam flux operation takes place under Ultra-High Vacuum (UHV) environment in order to avoid contamination from poor background pressure. Therefore, the UHV system is employed to ensure ultrapure crystal quality. For this reason, the MBE machine is constructed by using stainless steel to sustain the UHV environment. It operates with a base pressure of typically ~$1x10^{-13}$ bar. To assist the ultra-clean environment, the machine is kept inside a cleanroom.

To achieve UHV pressure levels, the MBE machine requires a bakeout of the entire system at 200 °C for 24 hours [76] before starting operation. The UHV facilitates the achievement of an atomically clean surface of the wafer by deoxidisation during heating up in the growth preparation stage. Creating the UHV environment enables a clear pathway for the MBE operation without undue interference by suppressing any gas phase scattering events. The relation between the mean free path and the UHV pressure in the chamber is governed by the equation:

$$\lambda = \frac{kT}{1.414\,P\sigma} \tag{29}$$

It can be seen that the mean free path (λ) is inversely proportional to the background pressure (P) and the collision cross section (σ). k is the Boltzmann's constant and T is the temperature. UHV systems typically have a mean free path of 5 x 10^5 m. Any type of contamination could potentially affect λ and prevent the achievement of good quality crystals.

The individual effusion cells, also known as Knudsen cells, contain group III and V solid-state elements (In, Ga, Sb, Si, Al and Be) contained in a Pyrolytic Boron Nitride (PBN) crucible. The PBN crucibles are highly mechanically stable, with a very low rate of gas evolution and chemically stability up to 1400 °C, which are suitable for hosting the elementary sources to ensure ultrapure source materials and molecular beam fluxes. Each crucible is also attached with a thermocouple for accurate temperature measurement.

A Knudsen effusion cell is designed to evaporate condensed materials. It could generate and propagate molecular beam fluxes which are directed towards a substrate surface on a rotation stage. It consists of an isothermal enclosure with a small orifice which acts like an evaporating surface, but it cannot reflect incident vapour molecules. The incident molecular flux rate (F) is given by the following equation which is also known as the Hertz-Knudsen formula:

$$F = \frac{P_p}{\sqrt{2\pi mkT}} \tag{30}$$

where m here is molecular mass. It can be seen in this equation that F is directly proportional to the partial pressure (P_p), which is in turn controlled by the temperature inside the Knudsen effusion cell. When the solid state elements are heated it is evaporated into a gas phase, transported in a form of molecular beam fluxes and directed towards the sample. The advantage of this type of deposition method is its ability to reproducibly deposit material with coverages ranging from sub-monolayer to continuous films. The beam flux is controlled by mechanical shutters, which open and close in a few tenths of a second. This is an order of magnitude faster than a

monolayer usual deposition rate, allowing sharp interfaces. The shutters and heaters inside the chamber are made of either molybdenum or tantalum metals. The heater inside the Knudsen effusion cell, which is responsible for heating the crucible, is controlled by a microprocessor which manages a proportional-integral derivative (PID) controller. This system determines the power level necessary to maintain the required temperature and sends feedback to the heater to control the intensity of the beam flux [76].

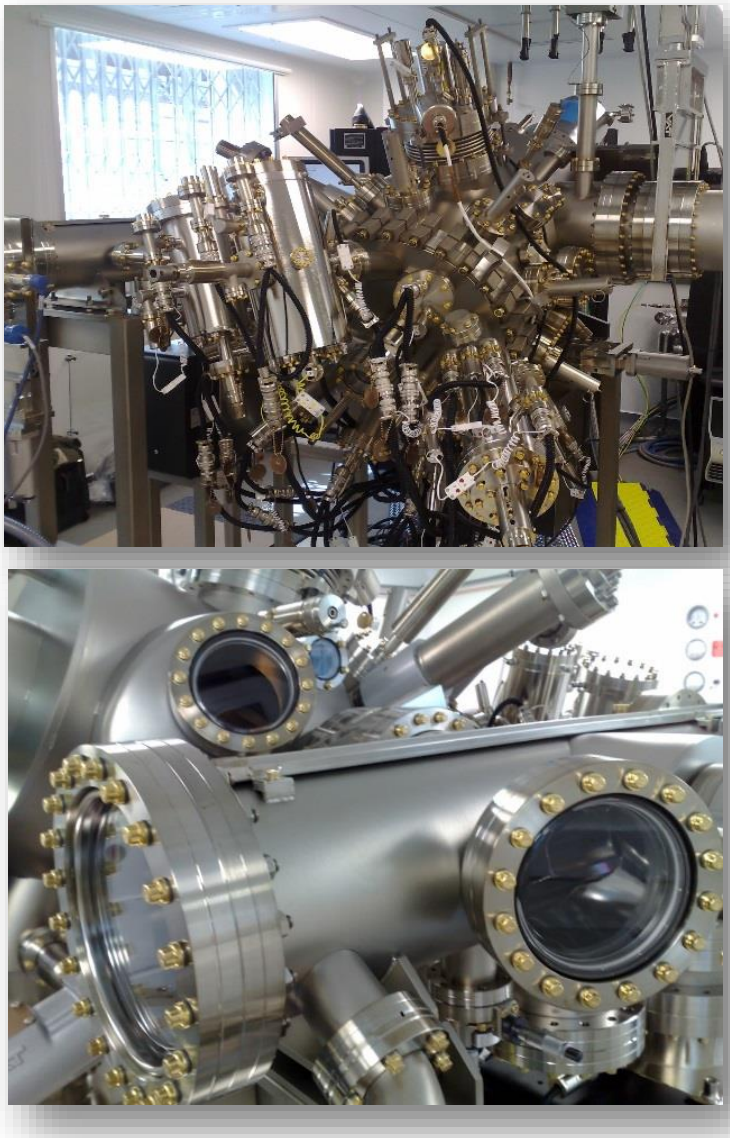

Figure 3.1: Two photos of **Veeco Gen-930** *solid-state molecular beam epitaxy system from (top) ground view and (bottom) a close-up view of the loading chamber.*

Figure 3.1 shows two photos of the UCL MBE system. The MBE consists of three chambers to keep the final growth chamber under UHV conditions at all times. The load-lock chamber utilises a rotatory mechanical pump and is vented every time a wafer is loaded. The wafer is then transferred to a preparatory chamber, which uses an

ion pump to transition from high vacuum conditions in the load-lock to UHV in the growth chamber. Finally, the wafer gets transferred to the growth chamber under UHV environment. This chamber uses an ion pump, a cryogenic pump and liquid nitrogen circulation to trap residue gases onto the cold walls of the stainless steel chamber, ensuring UHV conditions. All sample growth and maintenance work of the MBE system were carried out under the supervision and direction of Professor Huiyun Liu and Dr. Jiang Wu. They contributed to generating the recipe of the growth process, including the calculations of the growth parameters and calibration. Together, we contributed to the structural design of the solar cells for this work.

Figure 3.2 shows a schematic illustration of the MBE system. As mentioned earlier, heating an effusion cell initiates vaporisation of the ultrapure elemental source in it. The vaporised species beam out as a molecular flux onto the crystalline wafer substrate. In the process, an epitaxial build-up takes place on the growth substrate, via adsorption of incoming homoatomic molecules (e.g. Ga, As_2 As_4 etc.). The deposited species will migrate on the growing surface before dissociation occurs, which is the instant where the acquisition of the species to the epitaxial layer takes place. The migration and morphology of the growing layer depends on several aspects: (1) the flux rate, (2) the substrate temperature and (3) the crystallographic orientation.

Group III and group V elements have different polarities, and this determines the growth order sequence. The group III (cations) species have a unity sticking coefficient to the substrate surface, they are chemisorbed onto the growing surface and migrate to suitable lattice site at which they are incorporated. On the other hand, group V elements are physisorbed to the growing surface and requires the presence of group III elements in order to stick to the surface. Therefore, the growth rate of III-V compounds is dictated by the group III flux rate only and excess group V atoms are desorbed from the surface.

The migration length of the absorbed group III and V species is another important factor that determines the growth mode, and it is dependent on the growth temperature. The supply of thermal energy of the substrate facilitates the migration of the species.

In the case of low temperature, migration length is short and the III-V islands formed on the surface may fail to adjoin one another to form a complete 2D layer. In the case of high temperature, the migration length is extended and the probability of the element reaching the edge of an island increases. This facilitates an atomically flat 2D growth surface, but may lead to vacancies in lower layers.

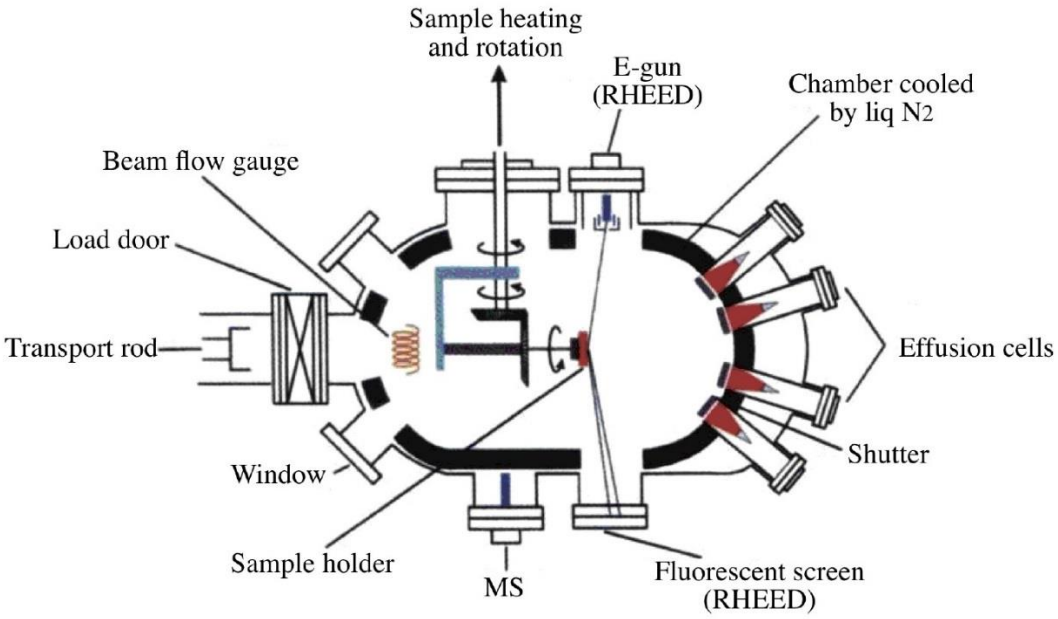

Figure 3.2: Schematic illustration of a MBE system showing the effusion cells pointing towards the sample stage controlled by mechanical shutters and an in-situ RHEED system within the growth chamber [77].

3.1.2 Reflective High-Energy Electron Diffraction (RHEED) system

In order to monitor the crystal growth, a Reflective High-Energy Electron Diffraction (RHEED) system is employed in the MBE growth chamber. Figure 3.3 shows a schematic diagram illustrating the diffraction pattern of the incident electron beam. It is a non-invasive and in-situ method to monitor the modifications of the surface morphology of the substrate wafer during growth. It consists of an electron gun that emits a high energy electron beam (~15 keV). This beam propagates to the sample surface and where it gets diffracted and reflected onto a phosphorescent screen. The phosphorescent screen captures the diffraction patterns, as depicted in Figure 3.3.

During the growth, different surface morphologies result in different diffraction patterns. The arrangement of the atoms on the wafer surface changes the diffraction pattern in real-time. As a result, the RHEED monitor gives immediate indication on the growth surface morphology. There are many advantages of integrating the RHEED system with the MBE. It is primarily favoured for creating no interference with the molecular beam fluxes.

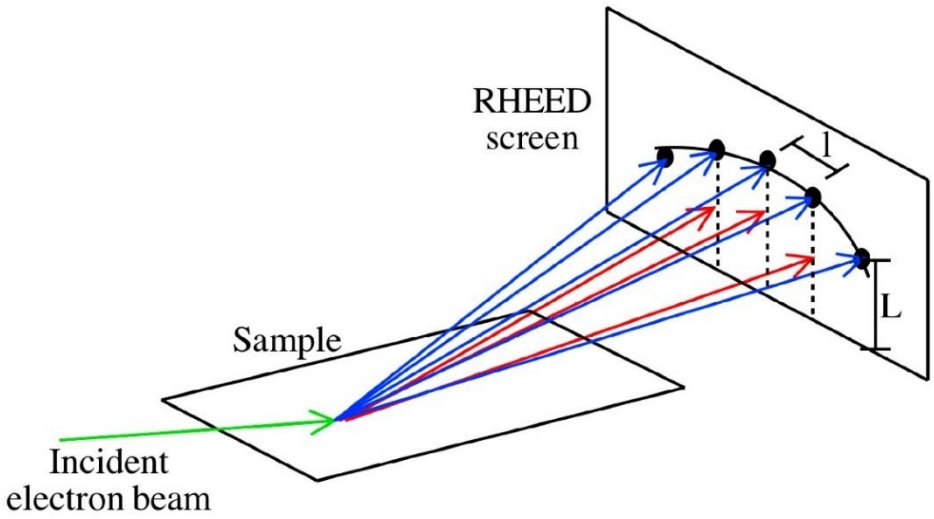

Figure 3.3: A schematic diagram showing the operation principle of a RHEED system where an incident electron beam is diffracted to the phosphorus screen depending on the surface morphology of the sample, giving information about the growth in real-time [77]

3.1.3 Growth of Semiconductor Quantum Dots

There are various ways of growing III-V solid-state QDs. The most common way is by forming 3D islands on the host surface [80]. The various MBE growth modes encompass Frank-van der Merve, Stranski Kranstanov and Volmer-Weber mode [78-80], as shown in Figure 3.4. The growth mode is determined by the lattice strain and surface free energy [81-83]. In the Frank-van der Merve growth mode, the atoms of the thin film are more strongly bound to the substrate than to each other. It undergoes layer-by-layer growth and does not initiate island formations. In contrast, in the Wolmer-Weber growth mode, the atoms of the film are more strongly connected with

each other than to the substrate. As a result, in Volmer-Weber growth mode, the atoms form 3D islands directly on the surface of the substrate. The Stranski-Kranstanov (SK) growth mode is somewhat intermediary between the two growth modes mentioned above. It initially progresses with a layer-by-layer deposition, with layers strongly bound to the substrate. Eventually, the elastic potential energy gets released during the nucleation 3D islands on the top layer.

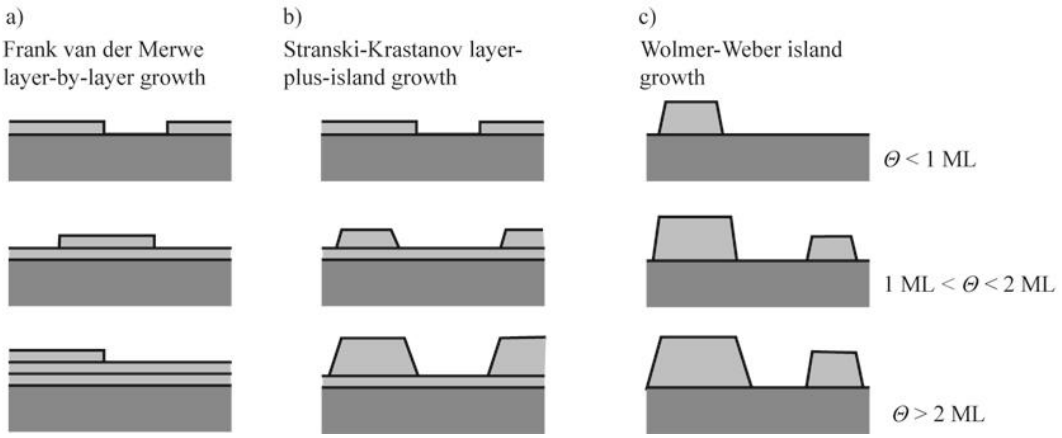

Figure 3.4: Three major processes for thin-film growth showing the gradual changes in the film as more monolayers are added to the surface: (a) Frank van der Merve, (b) Stranski-Kranstanov and (c) Wolmer Weber [78].

What makes the SK growth mode attractive in delivering self-assembled 3D islands is its relatively good uniformity and potentially defect free. This delivers a homogenous QD population that is easy to control. A homogeneous QD population gives a narrow emission line-width, which is important for certain optical devices, including QD-IBSCs. Furthermore, it is also a relatively inexpensive technique compared to other methods such as lithographically patterned electrodes and e-beam lithography.

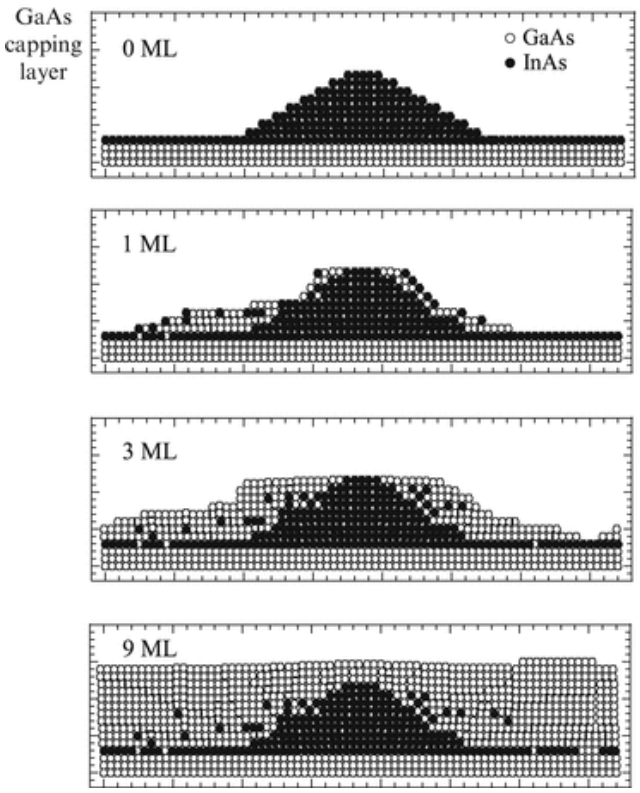

Figure 3.5: Self-assembled InAs/GaAs QD formation in SK mode showing the shape and size transformation after capping [79].

In the SK growth mode, QDs are formed by exploiting the lattice mismatch of two materials. There are different combinations of materials which forms self-assembled QD systems, such as InAs/InGaP [38, 84], InAs/GaAsSb [34, 85, 86], and InAs/AlGaAs [35, 87]. Among all, the growth conditions to yield high quality QDs are best understood for InAs/GaAs. Hence, it is the most common QD material system studied for IBSCs. InAs and GaAs are both zinc-blende materials, but their lattice constants differ by about 7%. In the growth process, the build-up of InAs epitaxial layers experiences a gradual strain on top of the GaAs layer. At a critical thickness of about 1.5 monolayers (ML), the accumulated strain creates a high elastic potential energy. This elastic potential energy is relaxed by inducing breakage of the 2D InAs layer [88]. The In and As atoms nucleate into nano-droplets on top of the GaAs, and each droplet forms a 3D island. It is worth mentioning here that the unbroken InAs layer below the InAs islands is called the wetting layer (WL). Sometimes, the presence of the WL is used to confirm what growth mode was used to fabricate the QD. The

SK mode normally obtains a QD density of 3 x 10^{10} cm^{-2} with a size distribution ranging from 20 to 50 nm [80]. The QD height is between 3-5 nm depending on the amount of InAs coverage.

Furthermore, the formation of QDs during the growth process is attested by the RHEED system. In and As atoms delivered onto the GaAs surface from the molecular beam fluxes first form an epitaxial 2D layer, with a relatively flat surface. The adsorbed atoms undergo surface migration to form the new 3D layer. The RHEED signal normally oscillates as new layers are progressively formed, and the transition from a 2D thin film to an array of 3D InAs islands directly inflicts a high degree of scattering. As a result, diffraction pattern changes with reduced signal intensity. This indicates that the 3D islands nucleation process has taken place.

Figure 3.5 shows a schematic of InAs QD-grown on a GaAs surface and capped by GaAs material. Usually, the QDs are capped with several monolayers of GaAs material as a spacer layer to enwrap the 0.36 eV InAs material. This usually results in QDs with a truncated pyramid shape as shown in the Figure. The smaller bandgap energy material enclosed with a higher bandgap material creates a bandgap offset to the VB and the CB. This induces a quantum confinement for the energy states in the smaller bandgap energy material and as a result exhibits quantised energy levels. Thus, self-assembled InAs/GaAs-QDs exhibit quantised energy levels which are employed to form the IB. The insertion of the InAs/GaAs QD system into a suitable p-n junction is the starting point for pursuing the IBSC concept.

3.1.4 Designing the Quantum Dot Solar Cell

All the solar cells in this work were grown by MBE to fabricate a superlattice semiconductor structure. The QD layers are grown within this structure. Figure 3.6 shows a schematic illustration of the QD solar cell structural layout. The solar cell structure is designed to exhibit a p-n junction in order to form a workable photovoltaic device with a depletion region. The n-side and p-side of the solar cell are doped with Si and Be, respectively.

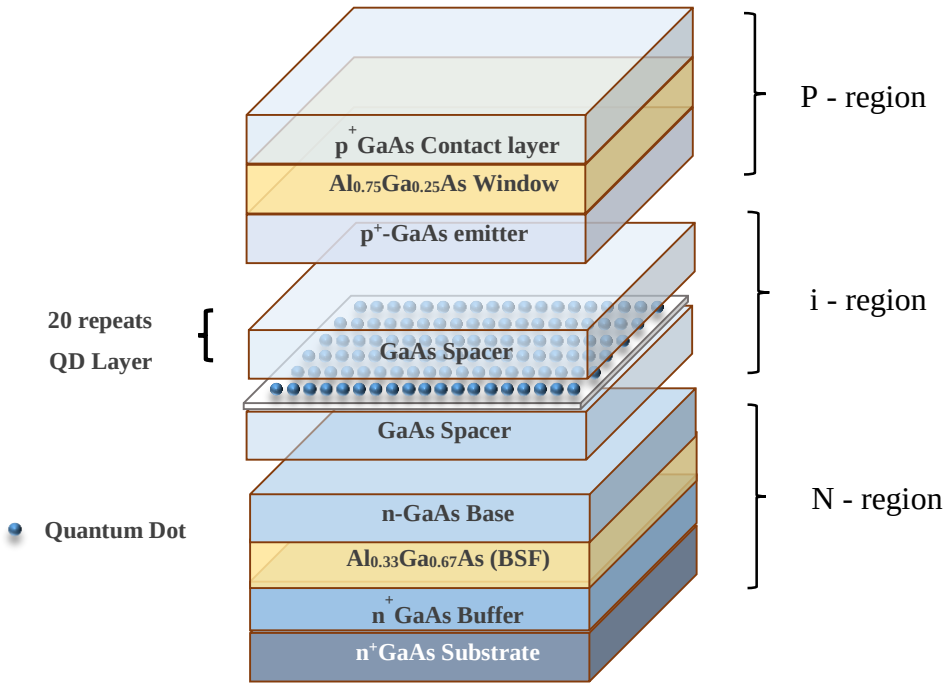

Figure 3.6: A schematic illustration of the structural design of a semiconductor QD solar cell with the materials of each layer

Usually, an epi-ready n^+-GaAs wafer (100) is used as a substrate to host the solar cell growth. To form the n-region, a relatively thick GaAs buffer layer of about 1000 nm is first grown to offset any imbalance strain from the substrate. This layer serves the purpose of accommodating the difference between two crystallographic structures and minimise strain. It is an n-type material heavily doped with donor Si atoms. A very thin Back Surface Field (BSF) is employed to reflect minority carriers back to the depletion region, which serves the purpose of minimising the carrier loss in the solar cell. More buffer layers are added at the end of the n-region to accommodate for the intrinsic (i)-region as well as to drive out photogenerated carriers with minimal losses in order to increase solar cell efficiency. Another important role for the buffer layer is to prevent abrupt band discontinuities at the interface of the window layer, preventing loss of minority carriers.

QD layers are grown inside the i-region, without any dopants. Normally, the QD layer is formed by depositing a thin GaAs layer of about 20 nm to serve as a spacer layer, followed by InAs of more than 1.5 ML. This is where the SK growth mode is

employed to achieve a highly uniform array of QDs, as mentioned above. Usually, 20 repeated layers of InAs/GaAs QDs are used to form this region. The growth rates and flux ratios can be controlled by the growth temperature and shutters sequence to modify the growth mode. This i-region can be modified for the purpose of investigation, such as changing the material or material composition.

Last, to form the p-region, a p+-GaAs layer of around 200 nm is deposited on top of the i-region. This time the GaAs layer is doped with acceptor Be atoms to achieve a p-type semiconductor. The Be dopant concentration is about 10^{18} cm^{-3}. A relatively thin window layer is composed of a high bandgap material to reflect minority carriers in the p-type semiconductor. Finally, a GaAs contact layer heavily doped with Be is deposited on top of the window layer to complete the solar cell structure. This contact layer is designed to form the interface with metal contacts to serve the purpose of carrier extraction. Therefore it is heavily doped (p^+) with Be concentration as high as 10^{19} cm^{-3}. Since the p-type semiconductor is the top surface exposed to illumination, the contact layer is kept thin at about 50 nm to minimise parasitic absorption.

The band diagram of the solar cell described in Figure 3.6 is depicted in Figure 3.7, except that only one layer of QDs is considered. It is shown here how the minority carriers are reflected back towards the designated contact by the window and BSF layers. Electrons are blocked from leaving the p-side and holes are blocked from leaving the n-side. This is possible with larger bandgap materials than the host. It is an important feature in the design of solar cells because carrier recombinations occurs more likely on the surfaces due to dangling bonds. Typically, the window layer is formed of a 30 nm thick $Al_{0.75}Ga_{0.25}As$ layer with a Be dopant concentration of 10^{18} cm^{-3}. A BSF layer is usually formed of a higher bandgap material, typically a 30 nm thick $Al_{0.33}Ga_{0.67}As$ layer doped with Si atoms with a concentration of 10^{18} cm^{-3}. Both the window layer in the p-region and BSF layer in the n-region serve the purpose of preventing the loss of minority carriers by reflecting electrons and holes back to the depletion region [91].

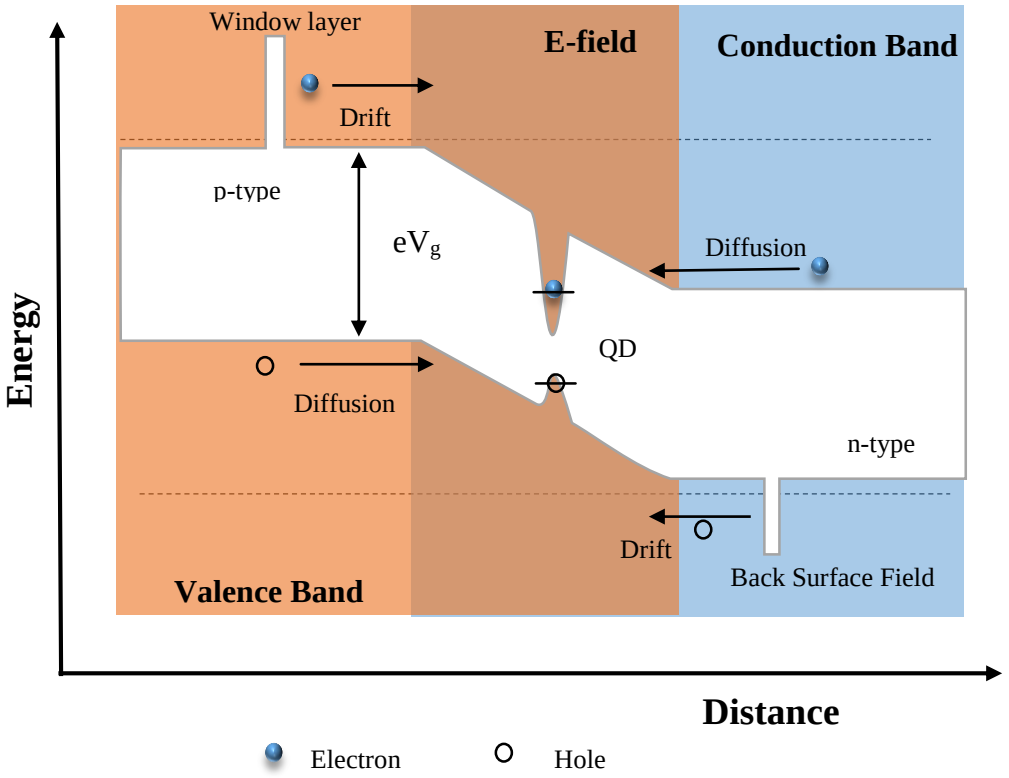

Figure 3.7: Band diagram of the solar cell with inclusion of the IB, the window layer and the back-surface field layer as illustration of design approach for quantum dot solar cell.

3.1.5 High Growth Temperature Spacer Layer

Materials with different lattice constants suffer from internal defects when grown on top of each other. These can be vacancies or interstitial defects, both forming traps for carriers and resulting in increased NR recombination rates. Superlattice structures usually accumulate a lot of strain due to the use of lattice-mismatched materials, which leads to damaging effects such as threading dislocation [92], as shown in Figure 3.8(a). This attenuates the capability of QD formation in subsequent layers. Thus not only it induces harmful defects in the solar cell but it also places an upper limit to the number of QD layers in the i-region. To prevent this problem, a high-temperature spacer layer growth technique is employed to relieve the strain [92-93]. This layer is subjected to high thermal treatment of 510 °C to smoothen the surface of GaAs by increasing the surface mobility of Ga adatoms. The reduced surface roughness prevents vertical

dislocations by relaxing the accumulated strain, as shown in Figure 3.8(b). As a result, the defect density in the GaAs spacer is minimised [90].

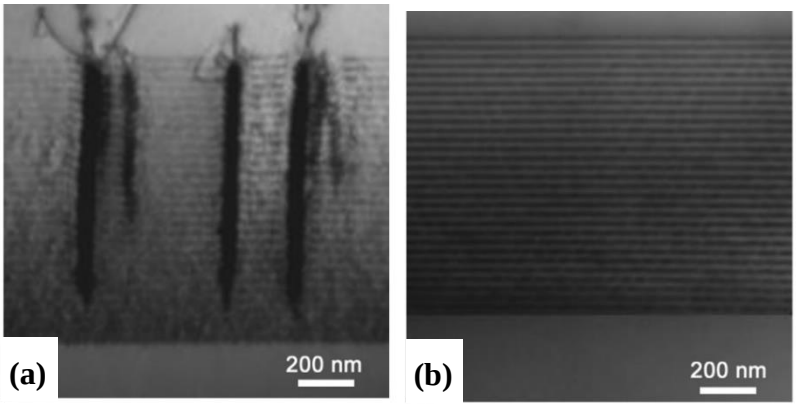

Figure 3.8: A transmission electron microscopy image or 30-stack QD layers grown with (a) and without (b) high temperature growth spacer layer [93]

The technique overcomes issues arising from strain accumulation, allowing for more QD layers to be stacked on top of one another. This allows, normally, 20-layers of QDs to be embedded into the i-region. However, this is not without limit as residual strain still remains even when the spacer layer is thermally treated. It has been reported that the performances of a 50-stack QD layer solar cell were lower than a similar structure with a 25-stack QD layer [94]. The conversion efficiency was severely degraded due to the presence of defect-induced NR recombination. For this reason, the QD solar cells design in this work will not aim to over-stack QD layers. Each QD layer normally has an array QD density of about 10^{10} - 10^{11} cm^{-2}. This would give a total density of 10^{12} cm^{-3}, which is sufficient to measure the optical properties of the QD i-region of the solar cell.

3.2 **Device Processing**

3.2.1 Introduction

After the grown QD solar cell leaves the MBE, one may cleave the sample into smaller pieces. The zinc-blende GaAs wafer with (100) orientation allows straight

clean cleaving. Therefore, a small score with a diamond tip followed by adequate pressure to the score can divide the sample in a straight line without damaging the cell structure. There may be oxidation of the AlGaAs layer from the side of the cleaved sample, causing defects, but this should not a significantly impact the solar cell performances as the ratio of the top surface to the side surface area is very low.

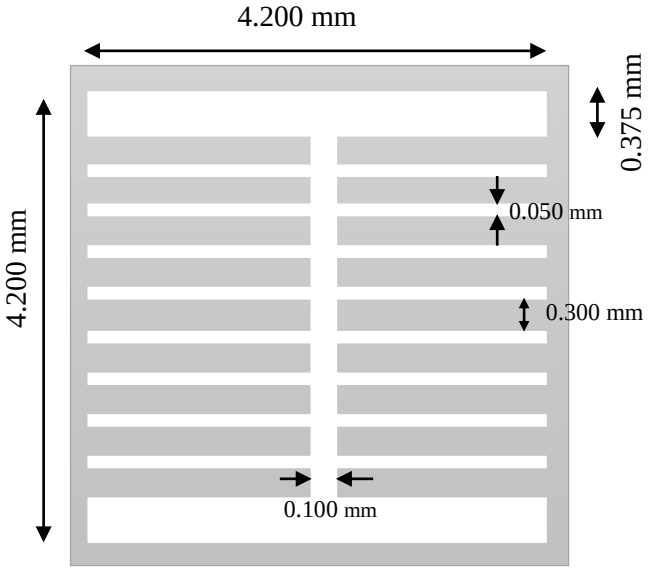

Figure 3.9: A Schematic diagram to illustrate the shadow mask labelled with the dimensions of the structure, designed for patterned metal deposition on the front surface of a solar cell.

The top surface of the solar cell is designed to allow light propagation. Therefore, the metal contact area should be minimised on this side of the solar cell to reduce shadowing. However, carriers exiting the depletion region of the solar cell have a limited diffusion length. Hence, they must be collected before recombination. In order to maximise this collection probability without a significant shadowing, the top contact of the solar cell device consists in a patterned metal contact. Figure 3.9 shows a CAD drawing of the design of the solar cell mask. The resultant solar cell could be wire-bonded onto a carrier. The mask pattern consists a middle bus bar with lateral fingers, where the fingers are thinner than the bus bar.

The patterning can be achieved by either a photoresist mask or a shadow mask. A photoresist mask allows high-resolution fabrication of small (around nm) features.

This involves photolithography techniques. In addition, the mask designed for photolithography usually facilitates mesa-etching at later stages. It can be used to isolate neighbouring devices from each other [95]. A shadow mask can be used on relatively larger samples of about 1 cm^2, and the solar cell isolation is then achieved via cleaving. In the case where solar cells are not grown directly on GaAs, but on a Si substrate instead, photolithography techniques are exploited for the purpose of mesa-etching, to allow an n-type contact to be formed directly from the top of the solar cell. This bypasses the Si substrate and avoids carrier loss through the defects at the III-V/Si interface. Both techniques take the solar cell coverage area into account, which is important for current density and efficiency measurements.

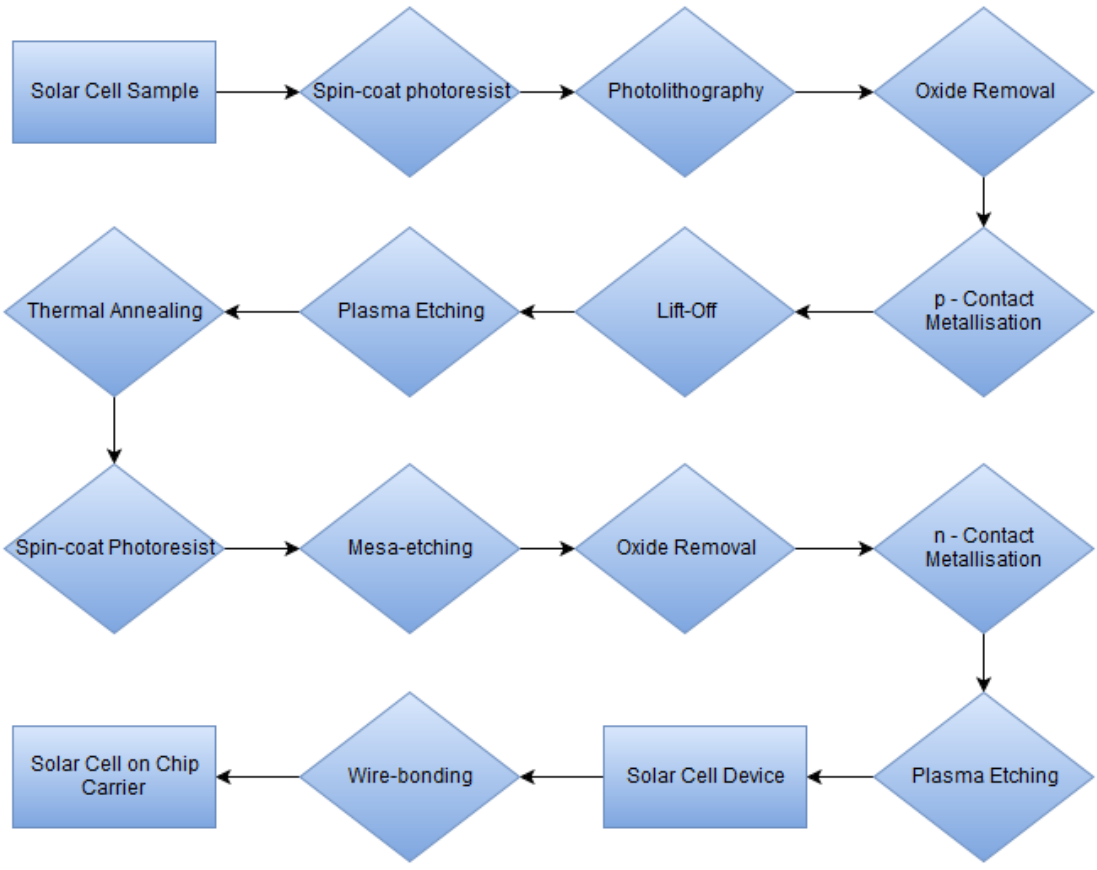

Figure 3.10: A process flow diagram illustrating the processing steps for the top p and bottom n metal contact deposition to convert a sample into a workable solar cell device.

Device processing took place in the Class 1000 (ISO 6) cleanroom of the *London Centre of Nanotechnology* (LCN). The grown solar cell structure leaving the MBE

system is transferred to the LCN cleanroom where it is processed into workable solar cells. Figure 3.10 shows a flow diagram of the process used for the deposition of the metal contacts to the solar cell, converting the semiconductor crystal structure into workable solar cells. This is essential to probe the cells and perform electrical and optical measurements on them. Current density-voltage (J-V) characteristics and External Quantum Efficiency (EQE) measurements on the solar cells would not be possible without these contact electrodes. The steps of the process are detailed here, which includes (1) cleaning, (2) photolithography, (3) chemical etching, (4) plasma etching, (5) thermal metallisation and (6) thermal annealing. Last and optional, the solar cells can be wire-bonded onto a chip-carrier as shown on Figure 3.9.

3.2.2 Sample Cleaning

In order to ensure a high quality semiconductor-metal interface, the surface of the wafer needs to be as clean as possible all along the fabrication process. Even microscopic organic residues can strongly interfere with the formation of a good Ohmic contact. Microscopic contaminants can introduce defects into the semiconductor-metal interface. This could potentially disrupt the surface crystallinity and increase surface recombination, leading to a degradation of the devices performances. To prevent this problem, each solar cell is cleaned in acetone for 5 min under sonication to degrease the surface. The sonication delivers ultrasound waves to agitate the sample, allowing organic contaminants dissolve in the acetone effectively.

Next, the sample is bathed in isopropanol (IPA) and methanol for 5 min each, under sonication. The sample is blow-dried with nitrogen gas. Chemical resistant plastic tweezers should be used when handling the sample in this process to minimise scratching on the surface. This helps to minimise possible damage to the crystal, avoiding potential scratch-induced recombinations impacting the ideality factor [96].

The sample is examined regularly under an optical microscope to identify any unexpected particles or damage on the surface. For tenacious particles, an IPA-soaked cotton bud is sometimes used to gently rub the sample to brush away the stubborn

residues. The cleaned samples are then rinsed with deionised water and dried again with nitrogen gas. For complete dehydration, the samples are heated in an oven at 200 °C for 30 min and leave to cool down at room temperature.

3.2.3 Photoresist spin-coating

A spin-coater is used to apply a uniform layer of photoresist onto the sample. Photoresist is a light-sensitive organic polymer, therefore the material is stored and handled under filtered light at all times. Dehydration of the samples helps to minimise any undesirable reaction with the photoresist. When a lift-off process is used, Shipley LOR10A (a lift-off photoresist) is spin-coated on the sample first. This photoresist has a higher rate of solubility, which is purposely used to generate an undercut. This undercut will later facilitate the lift-off process by opening channels for the solvent. LOR10A is spin-coated at 4000 RPM for 30 sec, usually leaving a thin uniform layer. Any particle on the sample surface will generate an uneven photoresist thickness on the sample, so it is important to ensure the sample is clean and dehydrated. After spin-coating, the deposited LOR10A photoresist is baked on a hot plate at 185 °C for 10 min. After cooling down, Shipley S1818 is spin-coated on top of the LOR10A using the same procedure and soft-baked at 115 °C for 1 min. Usually with this spin-coating RPM and time, the total thickness of the photoresists combined is about 2 μm.

3.2.4 Photolithography patterning

The photolithography technique uses UV-light to induce a chemical modification of the spin-coated photoresist. It is a widely used technique for electronic devices due to its ability to micro-fabricate integrated circuits with a high resolution. In a photolithography process, a photomask is used to transfer a geometric pattern onto the sample. The photomask is a glass plate with a pattern made of a thin film of chrome deposited onto it. The pattern is specifically designed for the purpose of the device. For example, the solar cell photomask used in this work has a pattern consisting of a bus bar and fingers, like the pattern shown in Figure 3.9. The features size using this technique depends on the mask. The current state-of-the-art in photolithography, using

deep ultraviolet light, can achieve a resolution of about 200 nm. Usually, one mask contains many repeated patterns to manufacture many devices onto the same sample. To be aligned with the sample, the mask is mounted onto a mask aligner using a vacuum holder. In this work, a Karl Suss MJB3 mask aligner has been used. The sample is mounted onto a vacuum chuck, in close contact with the photomask, and then aligned. The sample is exposed to UV-light in order to soften the photoresist. The exposure time is usually 1-5 sec, depending on the thickness of the photoresist on the wafer. After exposure, the sample is dipped into a developing solution (MF-26A) for 45 sec to dissolve the softened photoresist. The metal contact pattern is thus transferred to the photoresist.

3.2.5 Oxide Removal

An oxide layer usually builds up on top of a semiconductor surface when exposed to air. This will impair the quality of the contact if left on the surface. Either dilute hydrochloric acid (HCl - one part HCl with 1 part deionised H_2O) or ammonia solution (NH_3 - one part NH_3 with 19 parts deionised H_2O) can be used to remove the oxide layer. The sample is dipped in the solution for 30 sec followed by blow-drying with nitrogen gas. No rinsing with deionised water is needed. Although HCl and ammonia are both non-reactive to GaAs material, it should be noted that point defects on the surface may cause the sample to partially react with the solution. Loading the samples into the chamber of the evaporator immediately after oxide removal is recommended to avoid re-oxidation.

3.2.6 Thermal evaporation of metal contacts

Contacting the solar cell with metallic electrodes allows extraction of carriers from the semiconductor to an external load. Among metals, Au offers high electrical conductivity and is often used as part the contact electrodes. However, Au presents a relatively weak adhesion to GaAs and thermal treatment can cause the Au atoms to diffuse through the GaAs surface into the semiconductor. More importantly, to form a metal-semiconductor Schottky diode, metal with low energetic barrier is preferred

to facilitate extraction of the carriers. This thin Schottky barrier allows conduction across the semiconductor junction by tunnelling. Therefore, accompanying metal(s) are deposited first to facilitate Ohmic contact formation as well as adhering of Au and prevent Au diffusion. For the bottom contact to the n-type region, a Ni/AuGe/Ni/Au structure is typically used. For the top contact to the p-type region, Ti/Pt/Au or AuZn are typically used to form Ohmic contacts [97]. Both contacts are usually annealed separately in order to improve their crystalline quality and force the diffusion of the interfacing atoms from the electrodes into the semiconductor.

Metal contacts on the p- and n-side of the wafer have usually been deposited using an Edwards E306 Bell-jar thermal evaporator. Alternatively, an electron beam evaporator can be used to melt and evaporate metals with a higher fusion point such as platinum. Classic thermal evaporators consist of a glass bell-jar cover, which is sealed to the base of the evaporation stage with a rubber seal. The bell jar is usually cleaned before the evaporation procedure with concentrated hydrochloric acid or IPA to remove coatings from prior evaporations on the glass. This ensures good transparency, which helps to reduce heating inside the evaporator by avoiding light and heat reflection inside the bell jar. Transparency also enables visibility for the user to observe the evaporation process. Before loading the evaporator, the metal is cleaned with IPA under sonication to avoid contamination during the metallization step. Each metal type is held on a separate molybdenum boat. Molybdenum boats are used because they could withstand high currents and high temperatures. The sample is mounted on a copper block for efficient heat dissipation during the evaporation. It is placed about 15 cm directly above the metal sources.

A rotatory pump is used for rough pumping in order to obtain a vacuum level of 10^{-2} mbar inside the bell jar. A fine pumping step, using an oil pump, follows to further reduce the pressure to a vacuum level of 10^{-6}-10^{-7} mbar after a few hours of pumping. With a sufficient current through the molybdenum boat, the metal melts and generates vapours to coat the sample. The deposition rate is controlled by the current across the molybdenum boat. Mechanical shutters allow control on the beginning and ending of the evaporation. The thickness and deposition rate are monitored by a piezoelectric

quartz crystal resonator inside the evaporator. Usually, 200 nm of AuZn alloy and 5/50/20/200 nm of Ni/AuGe/Ni/Au are deposited onto the p- and n-side contacting layers of the sample, respectively. Separate evaporators are used for each contact to prevent cross-contamination. Post-evaporation thickness check is achieved with a Dektack XT surface profiler.

3.2.7 Lift-off

As the metal covers the whole sample, a lift-off process is needed to remove the photoresist and the metal on top of it to leave a patterned contact. Shipley microposit remover 1165 is normally used. It is a mixture of solvents designed specifically to remove all Shipley photoresist without degrading the sample. Normally, submerging the sample into this solution for 20 min without agitation is enough to gently lift-off the photoresist, leaving the newly evaporated metal contacts intact.

3.2.8 Plasma Etching

Microscopic organic residues can sometimes be left behind from the photoresist. Oxygen plasma etching, also known as dry etching, ensures complete removal of microscopic organic contaminants on the wafer surface to achieve an ultraclean profile. It consists of gusting the sample surface with a high-energy ionised oxygen plasma which only targets the organic residues.

3.2.9 Mesa-etching

Mesa-etching uses chemical solutions to etch down to the desired depth to create a mesa to isolate devices on the sample. This ensures current and optical confinement. GaAs etchants operate by oxidising the surface and then dissolve the oxide. In the process, it removes some Ga and As atoms. The chemical solution used for the etching consists of H_3PO_3: H_2O_2: H_20 (1:1:3). The sample is protected by a patterned photoresist layer and only exposes the area that is targeted for etching. The immersion of the sample into the solution would then be etched selectively. This exposes the area

underneath the surface of the solar cell and allows contacts to be made from the top of the solar cell, avoiding contact to the wafer.

3.2.10 Thermal Annealing

Post-evaporation thermal annealing enhances the quality of the semiconductor-metal interface by allowing diffusion of metallic atoms into the semiconductor. A Solaris 150 rapid thermal processor has been used for this purpose. It allows rapid ramp up and ramp down of temperature under controlled atmosphere. To ensure minimal oxidation, nitrogen gas is purged through the annealing chamber. The contacts to the p- and n-region are usually annealed at 380°C (30 sec) and 420°C (30 sec), respectively. Thermal treatment at the same temperature for a significantly longer time, for example 420°C for 60 min, did not show any difference. The improvement of the quality of the semiconductor-metal interface via thermal treatment process decreases contact resistivity [98]. If the thermal treatment exceeds the optimum temperature, pit can form on the metal surface. Rough undulations on the p-side metal contact have been observed after thermal treatment above 460 °C. Above 550 °C, pits began to form. This was found to be due to Ga and As atoms from the sample intermixing with Au atoms. As a result of metal degradation, the contact resistance was affected with an uneven spreading of current.

3.2.11 Shadow mask patterning

A metal shadow mask can be used as an alternative choice to the photomask in the photolithography process. It has defined patterns for metallisation where metal contacts can be deposited directly through, avoiding the use of photoresist. It forms direct physical contact with the sample and accompanies the sample inside the thermal evaporator [99]. Using thermal tapes, the 100 μm stainless steel shadow mask can simply be attached to the sample.

3.2.12 Wire-bonding

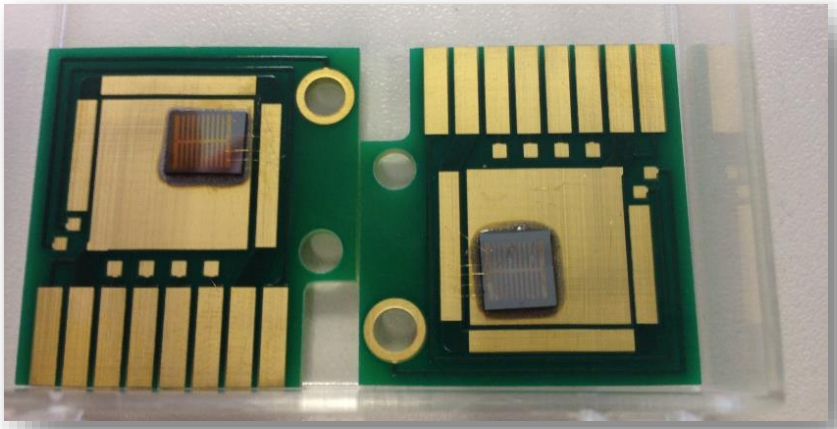

Figure 3.11: A photograph of the final solar cell wire bonded to the chip carrier.

Workable solar cells after development can be measured by connecting a probe station to the electrode contacts of the solar cell. Alternatively, a chip carrier can be used to prevent mechanical damage in the contact. This way, the solar cell contact can be extended to the chip carrier. Figure 3.11 shows a photograph of two processed solar cells bonded onto a chip carrier by gold wires and In paste.

3.3 Device Characterisation

3.3.1 Transmission Line Measurement

Low metal-semiconductor contact resistance is a requirement to ensure minimal impedance to the extraction of carriers. For a poor contact, the carrier extraction mechanism will be interfered with thermionic loss at the interface. The contact resistivity provides a general parameter used in device processing to compare the quality of the metal-semiconductor contact. It indicates how well the Ohmic contact is formed on the solar cell. To measure the contact resistivity, a Transmission Line Measurement (TLM) technique is used [97] on both n- and p- contacts. The TLM is a pattern of equally-sized metal pads unequally spaced to each other. A current sweeping

across two pads measure the resistance through the semiconductor-metal interface. The increased resistance as a function of the pad separation distance generates a plot. The line of best fit to the plot follows this equation:

$$R = \frac{\sqrt{\rho_c R_s}}{W} + R_s \frac{L}{W} \qquad (31)$$

where ρ_c is the contact resistivity, R_s is the sheet resistance, L is the distance between the pads, and W is the width of the contacts. TLM patterns are included in the solar cell photomask for the purpose of testing the contact resistivity. Currently the ρ_c achieved are ~ 1 x 10^{-5} $\Omega \cdot cm^2$ on both the n-side and p-side of the device. The other resistances including the sheet resistance across the semiconductor and probe-to-metal resistance are routinely tested for quality control. In addition, the series resistance across the cell is measured 2-5 ohms. As a result, a fill factor of typically 65-75% is achieved in this work. Each device development aims to achieve a low metal-semiconductor contact resistivity using the available tools in cleanroom facilities. It should be stressed that in order to achieve maximum solar cell performance a minimal contact resistivity is necessary.

3.3.2 Atomic Force Microscopy

An atomic force microscopy (AFM) is a topographic scanning technique invented by IBM scientists in 1986, developed by Gerd Binning and Heinrich in Zurich. An AFM consists of an atomically sharp tip attached at the end of a spring-like cantilever typically made of Si or SiN. Figure 3.12 shows a schematic illustration of AFM operating with laser diode on the cantilever spring and detection of surface topography is directly recorded using a photodetector. The tip is brought into proximity with the sample and measure the force between the tip and the sample. It scans the top of the sample in the x and y axis. The force could be mechanical contact force, van der Waals force, electrostatic force and more…etc. The force bends the cantilever co-ordinately subjected to the surface morphology of the sample. A laser is directed to the cantilever and deflected to a position-sensitive detector. There are three operation modes for

AFM: Contact mode, tapping mode and non-contact mode. In the contact mode, the signal is measured by directly contacting the tip onto the sample and drag along the surface. Tapping mode avoids the "sticking" to the liquid meniscus layer on the sample surface in an ambient condition by oscillating up and down just above the sample using a piezo element on the cantilever. This mode allows the AFM imaging technique to be used on biological components. In the non-contact mode, the tip oscillates above the surface and changes to the resonance frequency is registered by a feed-back loop and the average tip-to-sample distance constructs a topological image.

The surface morphology of the uncapped QD samples or the solar cell device was characterized by the Veeco Nanoscope V AFM machine to produce a precise topographic data of the surface of the sample. It is particularly useful in this work for examining the QD morphology. This allows the lateral size and height of the QD to be analysed. The computer software which controls the scan is called Nanosurf.

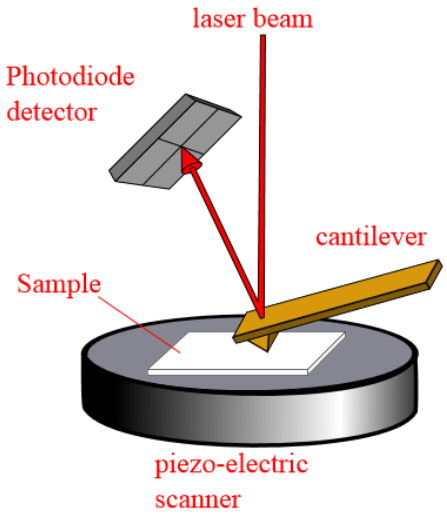

Figure 3.12: A Schematic diagram illustrating the operation principle of an atomic force microscopy [100].

Usually, to study the QD morphology, an uncapped QD layer is grown for surface examination purposes. This would deliver indications to the quality of the growth and the QD uniformity and characteristics. Information relating to the QD size distribution and density can also be obtained. Therefore, AFM images offer quick and valuable

information to understand the evolution of the QD when conducting a growth study. Any observation of large particles and clusters on the growth surface can be observed with this relatively quick and simple technique. It provides feedback to the growth process and adjustments to growth parameters can be made.

3.3.3 Photoluminescence

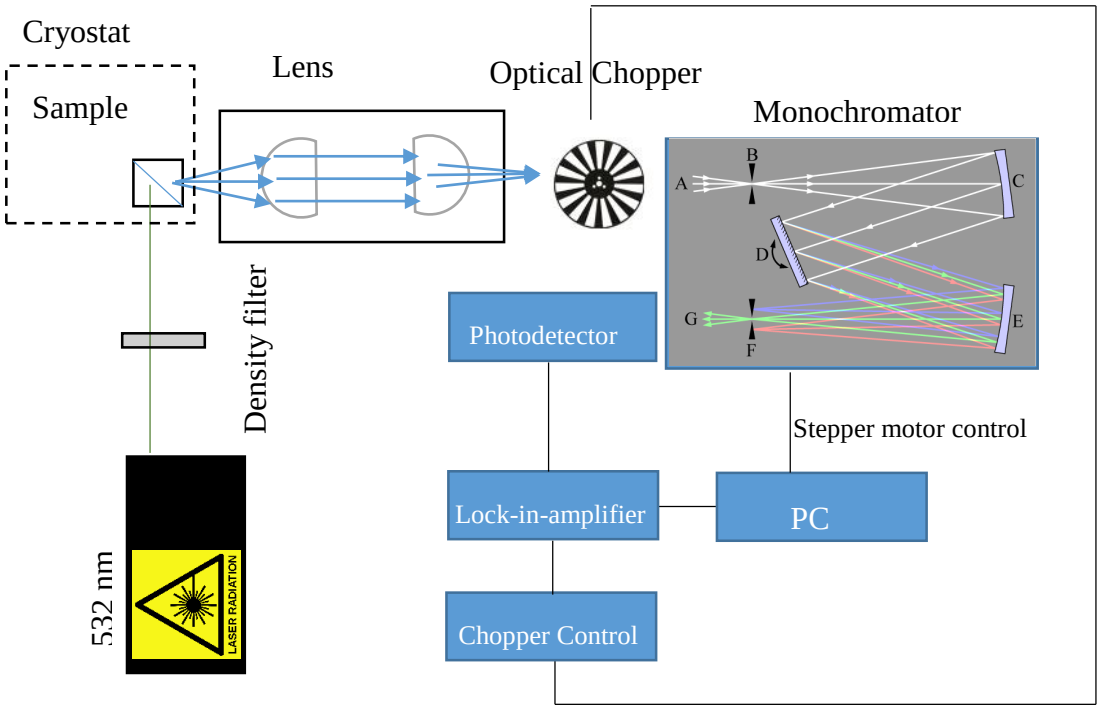

Figure 3.13: Diagram illustrating a typical photoluminescence measurement setup for optical characterisation of semiconductor devices using a 532 nm pump diode solid-state laser.

The photoluminescence (PL) spectroscopy is a contactless and non-destructive probing method using a high photon energy laser to excite a semiconductor sample of a lower energy bandgap. It is commonly used to determine the electronic structure of a sample. Figure 3.13 shows a schematic illustration of the photoluminescence setup. It was set up with a 532 nm diode pump solid-state laser. The laser spot size is 1 mm in diameter, however due to the lens and mirrors used in the setup, the laser spot size on the sample may change slightly. The laser excites the sample and luminescence is generated via the radiative recombination of the semiconductor sample. The emission signal from the radiative recombination process disperses out from the semiconductor

material and is collected in a series of biconvex lens. This converges the emission signal into a focusing spot of collimated light towards a 0.25m monochromator. An optical chopper is used to chop the signal into a modulated pulsed signal. A lock-in amplifier is employed to enhance the signal-to-noise ratio and directly controls the optical chopper. The monochromator consists of a grating system controlled by a step-motor to launch an optical diffraction. A dichroic mirror helps to direct the selected wavelength of light into the pinhole of the Ge photodetector cooled by a thermoelectric cooler. A radiometer in connection with the photodetector receives the electrical signal from the photodetector and generates a readout. The computer software TracQ Basic was used to control the start-stop of the measurement.

The PL emission spectrum offers invaluable information about the semiconductor. The position of the peak(s) in the spectrum indicates the energy of the bandgap. The height of the peak reflects on the strength of the emission, which is important for assessing the quality of the sample. For the QD emission, the full-width-half maximum (FWHM) of the peak indicates the uniformity of the QD population. Because the QD may exhibit more than one state (i.e. first excited state (FES)), it is important that a power-dependent PL measurement is carried out initially to distinguish the ground state (GS) from the FES. This can be accomplished by using different optical filters to dampen the laser power.

Due to the temperature-sensitive characteristics of a semiconductor material, a temperature-dependent PL measurement is sometimes carried out. The suppression of thermal emission removes the effect of crystal defects to the PL emission. This measurement can be carried out by mounting the sample onto a copper stage to enable intimate thermal connection to the cryo-system. This is facilitated by thermal grease and/or silver tapes. The system is enclosed with a stainless steel cryostat cover, which is clamped with a metal binding ring to enhance the seal. The chamber can be pumped down by a rotatory pump at 1500 rpm to achieve vacuum environment for the sample inside the chamber. Liquid helium from a compressor was used to circulate to the system to cool down the sample. The minimum temperature achievable in this system is 8 Kelvin. An electric heater and a thermocouple are situated directly under the

copper stage. The thermocouple generates a feedback to a thermal controller which controls the temperature in the chamber with a PID feedback loop to achieve and stabilise the temperature.

3.3.4 Light Current Density – Voltage Measurement

The light current density-voltage (J-V) curve is essentially an electrical characterisation tool in the presence of illumination. The electrical characterisation is carried out using a Keithley 2401 source meter. 4-point Kelvin probes are used to remove the effects of probe resistance. A temperature controlled stage is employed to keep the temperature of the solar cell stable, usually fixed at 25 °C.

Under dark conditions, the diode properties can be examined by injecting carriers into the cell with electrical means rather than light-generated carriers. From reverse to forward bias, a typical diode curve is formed. This gives a dark current measurement which provides diagnostic information about the solar cell such as ideality factor and saturation current. A Xeon lamp radiating collimated light which simulates AM 1.5 G spectrum, is used to illuminate the solar cell sample on the stage. Suction from the stage keeps the solar cell in position. Figure 3.14 shows the set up used in measuring the light J-V curve. Simulated sunlight (1 sun) is collimated and illuminates directly onto the stage where the solar cell is mounted.

Figure 3.14: Typical setup for electrical characterisation of solar cells using simulated sunlight of AM 1.5 G [101]

The illumination is calibrated to 1000 mW cm^{-2} using a RERA Si reference solar cell. When the solar cell sample is illuminated, a flow of the photocurrent under a photovoltaic effect generates electrical power. The area of the solar cell, usually about 0.25cm^2, is accounted in the J_{SC} calculation. The ratio of the electrical power to the power of inputted illumination is the total efficiency (η). The aforementioned equation for conversion efficiency is shown again here:

$$\eta = \frac{J_{sc}\, V_{oc}\, FF}{P_{in}}$$

J-V measurement is a standard procedure to measure the electrical parameters, which is standardised using AM 1.5G illumination to enable comparison with literature results. In a QD solar cell measurement, it is important to include a reference solar cell of the same structure but without QD structures to provide a control baseline. This is usually a p-i-n solar cell with only GaAs bulk material in the i-region. It

provides clarity in the measurement to distinguish the effect of including QD structures in the solar cell. In addition, if the reference cell is processed at the same time as the QD solar cell, the GaAs reference solar cell could offer additional information if a fabrication issue occurred.

In addition, the temperature-control stage could be used to measure the sensitivity of the solar cell at different thermal conditions up to 80 °C. The amount of changes to the J_{SC} and the V_{OC} as a function of temperature can be measured to provide information about the temperature sensitivity of the solar cell, especially when QD structures are included.

3.3.5 External Quantum Efficiency

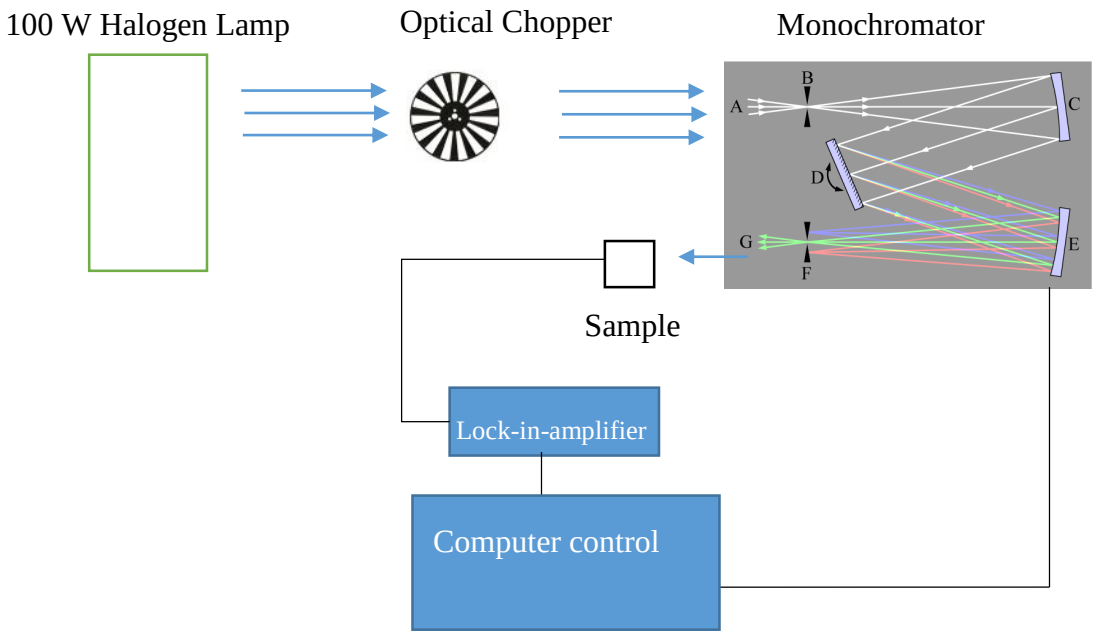

Figure 3.15: Typical setup for external quantum efficiency measurement from SpeQuest, with Halogen lamp of 100W monochromatically illuminated onto the solar cell sample.

Figure 3.15 shows a schematic illustration of an external quantum efficiency (EQE) system. The EQE spectroscopy is a measurement of the ratio of photogenerated carriers collected to the number of photons of a given energy. In solar cells and photodetector devices, it is an essential measurement to characterise the sensitivity of

the device to the wavelength of light. The setup is supplied by the RERA SpeQuest Quantum Efficiency system, which consists of halogen lamp chopped at a frequency of 188 Hz to generate pulsed light. A monochromator is employed to generate monochromatic light from the halogen lamp, which gets directed to the solar cell via a series of lens. A spectral coverage of 200-1800 nm can be measured. The solar cell is connected with an integrated Keithley system at room temperature and zero bias. Either a Si or Ge reference solar cell is used for calibration of the system, depending on the desired spectral region. Photor 3.1 software is used to initialise the system and display the EQE spectrum. The relationship between the J_{SC} and the corresponding quantum efficiency spectrum can be seen in this integral equation:

$$J_{SC} = q \int_0^{\infty} F(\lambda).EQE\ (\lambda)d\lambda$$

F is the photon flux and q is the elementary charge of an electron. It is possible to calculate the J_{SC} using the spectral response of the cell. This equation, however, assumes that the EQE used is representative of the entire solar cell.

3.4 **Chapter Summary**

The method of fabricating QD solar cell has been discussed in this chapter. Using the MBE facility, ultrapure semiconductor crystal for the solar cell can be grown. It consists of elementary solid-state sources that generate molecular beam flux on a substrate surface to initiate a reaction on the surface of the substrate. The machine can manufacture pure monolayers of semiconductor crystals, grown with fine atomic precision. Suitable dopants are available in-situ to convert the semiconductor crystal to an n-type or a p-type material. Such technology using diffusion sources promises to deliver highly uniform crystals. The substrate to host the solar cell is a semiconductor wafer on which the solar cell thin film is directly grown. The wafer containing the solar cell structure is then developed into solar cell devices.

The design of the III-V semiconductor solar cell is outlined. All solar cells are grown on a GaAs (100) epi-ready wafer substrate. InAs/GaAs self-assembled QDs grown in SK-mode were used in the solar cells. Overall, the solar cell structure comprises a p-n junction which exhibits a built-in E-field in the depletion region. This sweeps the carriers to their designated terminals to generate a unidirectional flow of carriers. A window and BSF layer are employed to minimise surface recombination. Also, the semiconductor surface contact is designed to form selective contacts. These designs accommodate the QD within the depletion region. The QDs are used as an absorber material, employed to exhibit the IB arising from the confined states of the electrons in the CB tri-dimensional potential wells, which originate by the CB offset between the InAs QD and the GaAs barrier material. The outcome is a QD implantation within the matrix of the p-n junction which gives VB→IB and IB→CB transitions in addition to the VB→CB optical transition. Ideally the voltage extracted from the QD solar cell is the difference between the CB and VB quasi-Fermi level at the n- and p- contacts, respectively.

All MBE-fabricated QD solar cells are developed using semiconductor processing technology in the cleanroom laboratory. Solar cell devices with metal contact electrodes are processed using photolithography or shadow mask techniques. Formation of Ohmic contacts with low contact resistivity ensures minimal thermionic loss [99]. Finally, the solar cells can be optionally bonded onto a chip carrier. Characterisation of the solar cell using AFM, PL, J-V and EQE measurement is described here. These characterisation tools allow one to obtain crucial information about the solar cell's behaviour. In the next chapters, results and data are presented from these tools.

Chapter 4

Submonolayer Quantum Dot Solar Cells

4.1 Introduction

Much effort has been devoted in manufacturing a strong solar-energy harnessing converter. Unfortunately, even the best new prototypes have fallen short of their ideal performance. This is partly due to practical limitations in the material quality, which applies to QD solar cells too. Although embedding QD layers into the solar cell structure has shown extended absorption coverage of the solar spectrum, the contribution of each QD layer to the total photocurrent of the solar cell is very small. For this reason, there are still no quantum systems that have shown a significant improvement that could surpass the Shockley-Queisser limit for a single-junction solar cell conversion efficiency. This includes QD-IBSC, multi-carrier generation and hot carrier solar cells. However, in QD solar cells, there is a direct relationship between the densities of QD to the strength of the sub-bandgap absorption. The sub-bandgap absorption can be observed in an EQE spectrum of a QD solar cell [102]. It is therefore demonstrated that QD solar cells are promising systems to generate additional photocurrent atop a single-junction solar cell. However, one of the challenges remains in preserving the quality of the crystalline semiconductor solar cell when QDs are embedded.

Quantum well (QW) structures were once proposed as a good material system to generate sub-bandgap photocurrents [103]. Sub-bandgap energy photons facilitate the improvement in conversion efficiency. However, the lattice-mismatch heterostructure leads to point defects in the crystal and threading dislocations happening after the growth can degrade the superlattice crystal quality. This usually generates low-quality and unreliable devices which could lead to a short life-time performance. Because the interface between two materials of different lattice constant builds up strain [25, 104], there is an upper limit to the number of stackable layers. There is a pressing need for a solution to increase the number of layers stacking on top of one another, without needing to compensate for defect formations. If this could be accomplished for QD layers such that high density of QD populations could be realised, solar cell design could gain a significant benefit by adding many thin layers of the quantum structure to increase light capture. In other words, the QD region of a solar cell could form a strong light-absorbing material for sub-bandgap energy photons.

QWs are repeating nanolayers of a lower bandgap semiconductor materials inside the matrix of a larger bandgap material. The electrons are only confined in one direction. Therefore, a continuum of states in the confined level and the semiconductor band associated with the transversal velocity of the electrons is not quantized [105]. Thus, what the QW essentially does is to reduce the semiconductor bandgap with respect to that of the barrier material and therefore produce a new semiconductor with a modified bandgap. Although they can be used to tune the bandgap of the cells in MJSC approaches and can lead to produce very good solar cells [21], [23], the separation of the QW and CB quasi-Fermi levels, which is essential for IBSC, is extremely difficult in QW solar cells. For this reason, QW structures are non-ideal as IB materials and cannot establish IBSC operation [49].

Since QDs has been proposed as a suitable candidate for IBSC due the 3D quantised energy level of the QD material, it has been extensively compared with QW structures. In the past, there have been several approaches to increase sub-bandgap photon absorption by structurally modifying QD solar cells such that the QD population increases. Tutu *et al* studied the effect of increasing the areal QD density

in a 20 layer QD solar cell and has shown improvement in the absorption of longer wavelengths. This was accomplished using SK mode to induce a nucleation process facilitated by pre-deposited antimony-surfactant, which gave rise to self-assembled QD with a population density of ~1 x 10^{11} cm^{-2} per QD layer [106]. Another way of increasing the QD population density is by increasing the number of self-assembled QD layers [107]. This approach requires QD layers to stack vertically on top of one another. However, with lattice mismatch materials being used in the process of producing the self-assembled QDs, the resultant solar cell suffers greatly from accumulated strain. It has been reported that a solar cell embedded with 50 InAs/GaAs QD-layers suffer greatly from performance degradation [94] even though the sub-bandgap current was greatly enhanced. The reason being the poor material quality in the intrinsic region extending to the emitter region of the solar cell deteriorates the solar cell. This is a result of stress produced in the QD layer. Although strain-relaxation during SK-growth releases pressure on the intrinsic layer that hosts the QD, the incomplete relaxation leaves residue strain which affects the subsequently layer above [108].

4.1.1 The Effect of Crystal Strain

Figure 4.1 shows a schematic illustration of the interface of two lattice-mismatch materials. Due to the difference in the spacing of the atoms, misfits appear periodically at the interface. This directly leads to point defects in the crystal structure which is classified in three types: vacancy, interstitial and antiphase defects. A dislocation is a line defect that extends in the growth direction. It is a direct result of accumulated strain from a build-up of elastic potential as the crystal body continues to grow [108-109]. The expansion of this elastic potential creates a strain-field which could become significant. When the crystal lattice cannot sustain the overstretching molecular bonds, a resultant threading dislocation occurs which makes cross-sectional cracks to the material. This effect is more destructive if the two interfacing materials differs significantly in thermal expansion coefficient.

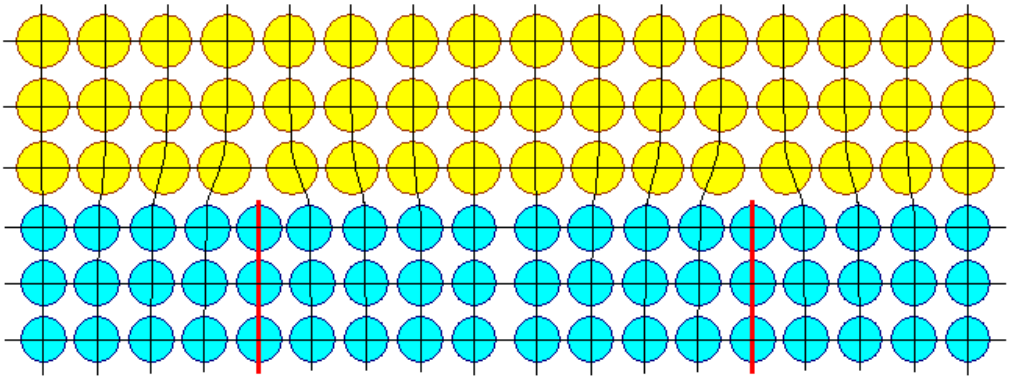

Figure 4.1: Schematic of two lattice-mismatching materials and the result of strain.

Both point defect and dislocation acts as NR recombination centres which increases the loss of carriers [110, 111]. Therefore, the presence of defects lowers the output voltage by increasing the saturation current and also the photocurrent by impeding the carrier extraction, which places a limit to the conversion efficiency.

In addition, strain within the crystal lattice of the semiconductor also makes an impact on the mobility of the carriers and the bandgap energy. Even though there are strain-compensation techniques using modified capping layers such as GaNAs [112, 113] and GaAsSb [114, 115], it is difficult to completely offset the strain without altering the electronic band structure. It was thought that strain compensation layers could tackle the many problems of a lattice-mismatched heterostructure. However, no significant improvement of the efficiency has been reported when the technique was employed. On the other hand, an effective strain-relaxation mechanism during growth could offset a lattice strain and reduce the formation of point defect and dislocations. Using an effective strain relaxation mechanism is beneficial in increasing the population density of QDs [107, 116].

Since increasing SK-QD population density only led to marginal photocurrent improvement, and highly stacked SK-QD layers has made severe degradation to the solar cell material, there is a need to search for new structures to offer a substantial solar cell architecture in order to avoid strain build-up. This promoted the attention on submonolayer (SML) QD structures.

4.1.2 Submonolayer Vs Stranski-Kranstanov Quantum Dot

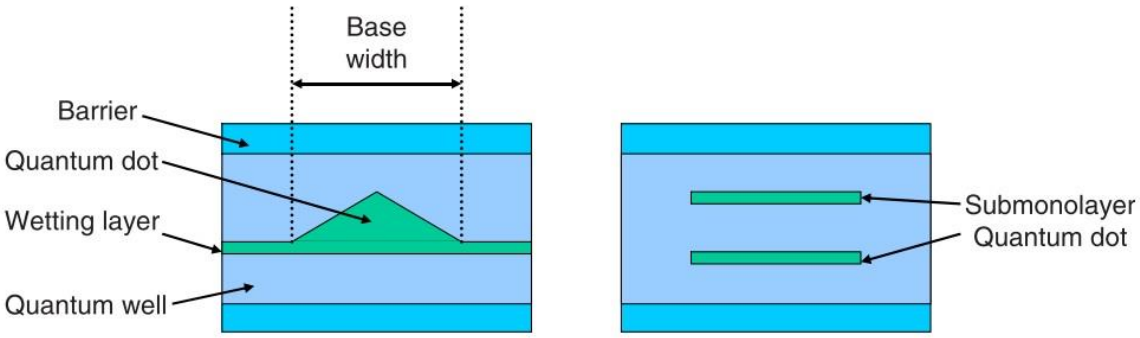

Figure 4.2: Schematic drawing of a Stranski-Kranstanov quantum dot with a submonolayer quantum dot [117].

In recent years, SML-QD has found applications in super-luminescence diode [118] and vertical cavity surface-emitting lasers [119]. It also deserves a special mention for infra-red photodetectors which has reported a significant enhancement in absorptivity [117, 120]. However, solar cells embedded with this structure have not been studied. SML QD is formed by cycle deposition with a fraction of a monolayer (ML) of the dot material buried within several MLs of matrix material [118]. Figure 4.2 shows a structural comparison between a SK-QD and a SML-QD. SML-QD is described as a parquet or disk-like shape, with the dimensionality of ~5 nm in lateral size and ~2 nm in lateral spacing, much shorter than a SK-QD [119]. This could potentially give rise to an areal density of ~10^{12} cm^{-2}, higher than the best known maximum density of 10^{11} cm^{-2} achieved with SK-QD [106].

Comparing the growth mechanism with SK-QD, the SML-QD does not require the formation of a WL because the deposition amount of the QD material is far lower than the critical thickness. On the other hand, the WL serves as an essential ingredient for SK-QDs because the nucleation process occurs on top of the WL. A disadvantage of this is the reduction of carrier confinement due to the presence of continuum states in the WL. Although some reports have shown removal of the WL using AlAs material capping [121, 122], the introduction of Al material between the QD and the barrier

layer could compromises a high-quality QD growth. In the SML-QD growth mechanism, depositing a fraction of a ML of the dot material onto the matrix material forms a dense array of 2D islands. These islands can then be capped by an overgrowth of a matrix material. The underlying strain from thin lattice-mismatched layers induces an intrinsic surface stress, which leads to the formation of arrays of anisotropic InAs islands [123]. Another feature of the SML-QD structure is the possible ultra-thin spacer layer that could be as low as 5 nm. With this structure, vertical tunnelling of carriers between dots are possible. Previous studies on SML-QD showing a narrow FWHM of the PL spectra suggests good uniformity [124]. These features give desirable advantages to optoelectronic devices such as photodetectors and solar cells.

Whilst the absorption of the normal incidence radiation is attributed by the in-plane quantization, the height of the QD is less critical. Therefore despite the short height of SML-QD islands, the 3D confinement advantages are retained [117]. It has been reported that the absorption efficiency of the SML-QD outperforms that of SK-QD [124]. This makes SML-QD a very interesting candidate for the photogeneration role of solar cells. The improvement in absorption efficiency can be explained by the attribution of strong coupling of wave functions of the carriers between states. In this chapter, a p-i-n structured solar cell with multi-stacked InGaAs/GaAs SML-QDs incorporated in the i-region is investigated. Some results in this chapter are published in the journal of *Solar Energy Material and Solar Cells* titled **"**Submonolayer InGaAs/GaAs quantum dot solar cells" [41].

4.2 **Growth and Fabrication**

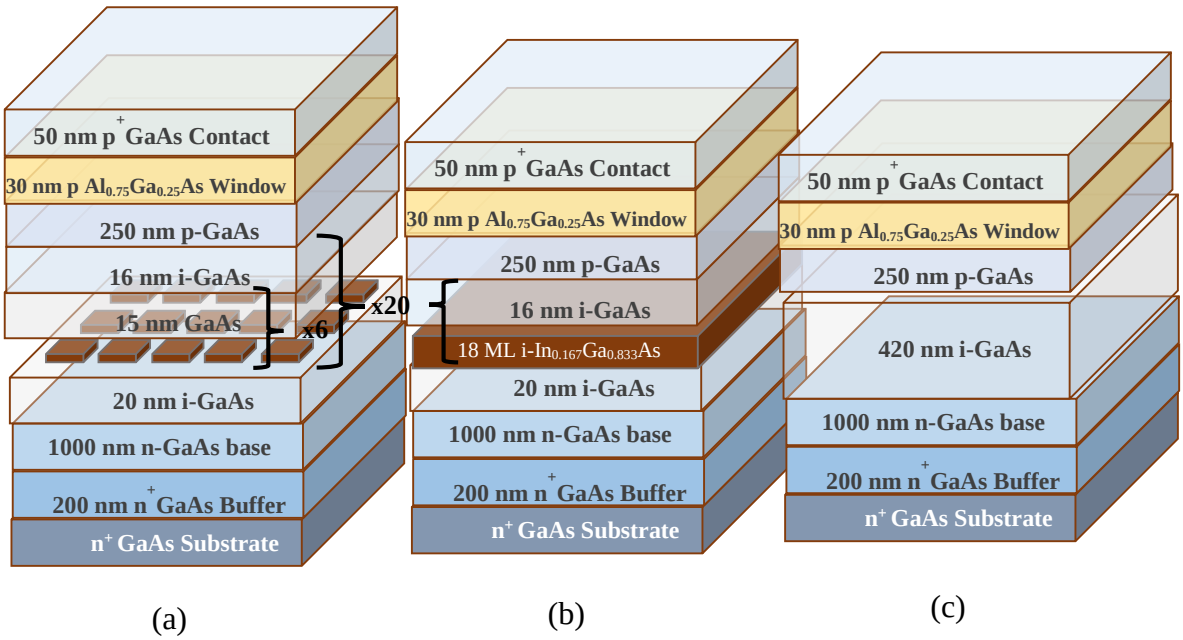

Figure 4.3: A Schematic diagram to illustrate the structure of the (a) SML-QD solar cell, (b) QW solar cell and (c) GaAs reference cell.

Three solar cell samples, GaAs reference (Ref) cell, QW solar cell and SML-QD solar cell were grown via the Veeco solid-state MBE on an n+ GaAs (100) substrates. Each substrate was heated in-vitro to degas the surface oxide. The GaAs reference cell consists of 200 nm of n+GaAs buffer, 1000 nm n-GaAs base layer, 420 nm of undoped GaAs in the i-region, 250 nm p-GaAs, 30 nm p-$Al_{0.75}Ga_{0.25}As$ window layer and 50 nm p+-GaAs. The QW solar cell has the same structure as the GaAs reference cell except 20 layers of undoped InAs/GaAs quantum well (QW) structure were inserted in the 420 nm i-region. Each QW structure is formed with 18 ML of $In_{0.167}Ga_{0.833}As$, an equivalent thickness of 4nm, and 16 nm of GaAs spacer layer. The SML-QD solar cell has a similar structure as the QW solar cell except the i-region has 20 layers of a 6-stack SML InAs QD iteration. Each stack consists of 0.5 ML of InAs and 2.5 ML of GaAs. All solar cells have high temperature growth (710 °C) spacer layers on top of each period to suppress the formation of threading dislocation [93]. A schematic illustration of the solar cells are shown in Figure 4.3.

In order to measure the JV and EQE of the solar cell, the GaAs, QW and SML-QD solar cells were cleaved into approximately 1x1 cm^2 sizes, and cleaned with acetone, IPA and methanol under cleanroom conditions. Both sides of the solar cell were lightly etched with dilute NH_3/H2O (1:20) and dried with N_2 gas to remove the thin surface oxide layer. The solar cells were loaded into an E-306 bell-jar evaporator for Ni/GeAu/Ni/Au (5/50/10/200 nm) deposition on the n-contact at vacuum pressure 1 x 10^6 mbar. This is facilitated by a bulk copper block of 0.5 Kg which is responsible for heat absorption and preventing poor contact formation. The metal contacts were thermally annealed at 420 °C with a Solaris 150 Rapid Thermal Processor. The p-side of the solar cells were mounted onto a chrome shadow-mask before reloading to the evaporator. The shadow mask consists of a pattern of a bus-bar with lateral grids designed to minimise light blockage by the metal. Au/Zn/Au (10/20/200 nm) were thermally evaporated onto the p-side solar cell. No antireflective coating was applied to the solar cell surface.

4.3 **Surface Morphology**

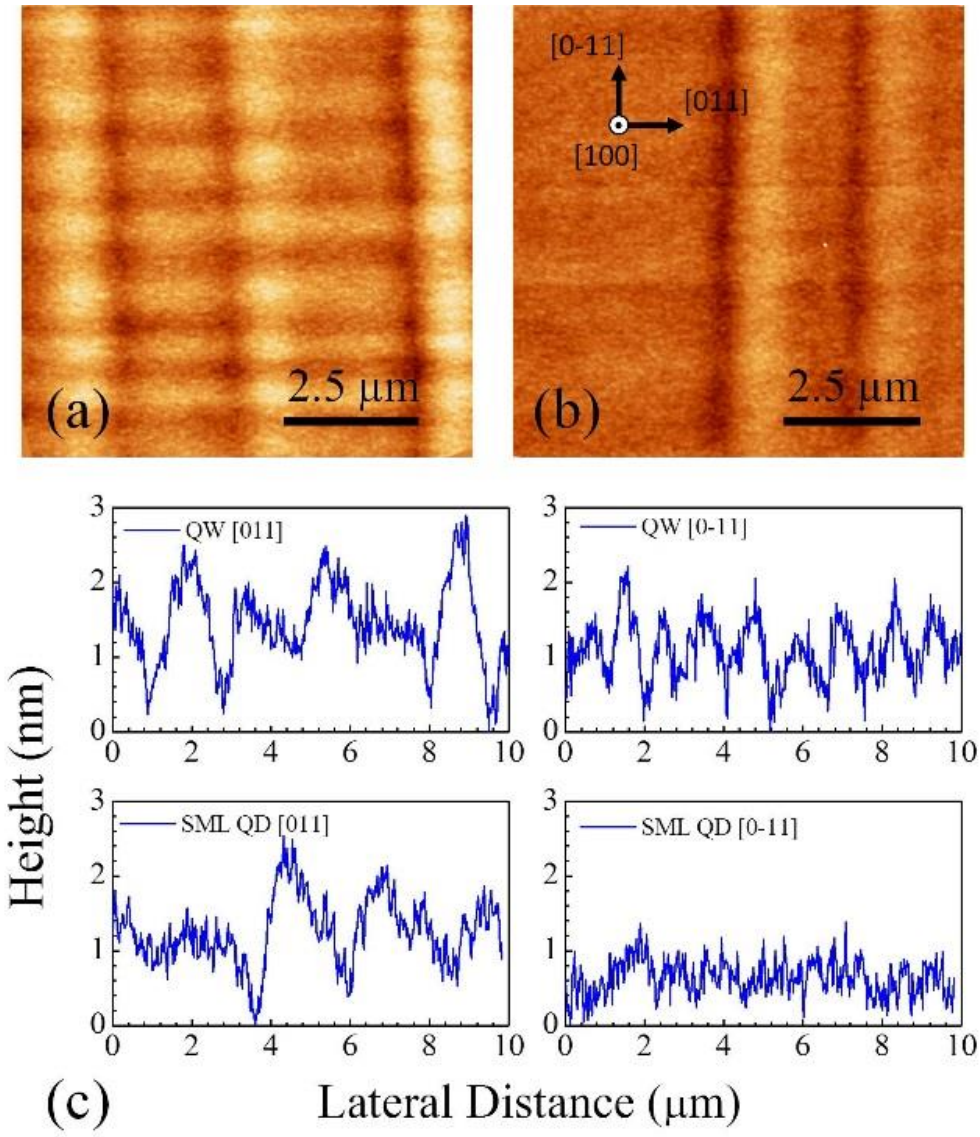

Figure 4.4: AFM images of the surface morphology of the (a) QW solar cell and (b) SML-QD solar cell. The scale bar is 2.5 µm and the z-scale is 5 nm for both images. (c) AFM line profiles along [011] direction (left) and [0-11] direction (right) on QW solar cell surface (top) and SML-QD solar cell (bottom).

In order to understand the structural impact of stacking the SML-QD structure, the top surface of the solar cell is examined first to reveal the information regarding to the upper emitter surface. Morphological studies were carried out using the Veeco AFM on the p-side top surface of the solar cell. Figure 4.4(a) and (b) shows the surface

morphology of the QW and SML-QD solar cell, respectively. Both solar cells show an uneven surface, however the QW solar cell shows deeper ridges at both [011] and [0-11] direction, with a height of 2-3 nm. The SML-QD solar cell shows a relatively flat surface with the height of only 1 nm on the [0-11] direction. The pattern presented on the surface is commonly known as a cross-hatch. It often appears on lattice-mismatch hetero-epitaxy structure surfaces. It is likely the result of strain-induced surface roughening caused by lattice-mismatch epitaxial growth [39, 125], and strain-relaxation can introduce surface undulation and local enhancement of growth rate over the misfit dislocations. The QW solar cell surface displays a wider line of the cross-hatch, which indicates a relatively rough surface, therefore stress was built up by the QW structure during growth. As compared to the SML-QD structure, less stress is resulted from the stacked layers of InGaAs/GaAs iterations. Although the same amount of lattice-mismatch materials were used, both solar cells differ from the strain accumulation. The result indicates a different strain relaxation occurred in the growth process.

The AFM line profiles along two orthogonal directions on both cell surfaces are shown in Figure 4.4(c). The difference in profile roughness in orthogonal [011] directions is attributed to the anisotropic strain relaxation. The ridges aligned along [011] and [0-11] directions is a direct result of lattice mismatched hetero-epitaxy. This could be attributed by the strain-relaxation introduced surface undulation and/or local enhancement of growth rate over the misfit dislocations [126]. On the QW solar cell, the cross-hatch pattern clearly appears to have a rougher surface with a higher number of ridges. The profile roughness along [011] direction is 0.24 nm and 0.39 nm for SML-QD and QW solar cell, respectively. The result indicates different strain relaxation during the hetero-epitaxy growth of SML-QD and QW solar cell. While depositing fractional coverage of InAs, In segregation leads to InAs agglomerations and then causes three-dimensional shape transformation or compositional modulation [127]. The formation of InAs agglomerations will partially compensate the lattice-mismatch between InAs and GaAs and therefore, elastic strain relaxation through forming undulated surface is less prominent for SML-QD solar cell.

4.4 **Cross-section Transmission Electron Microscopy**

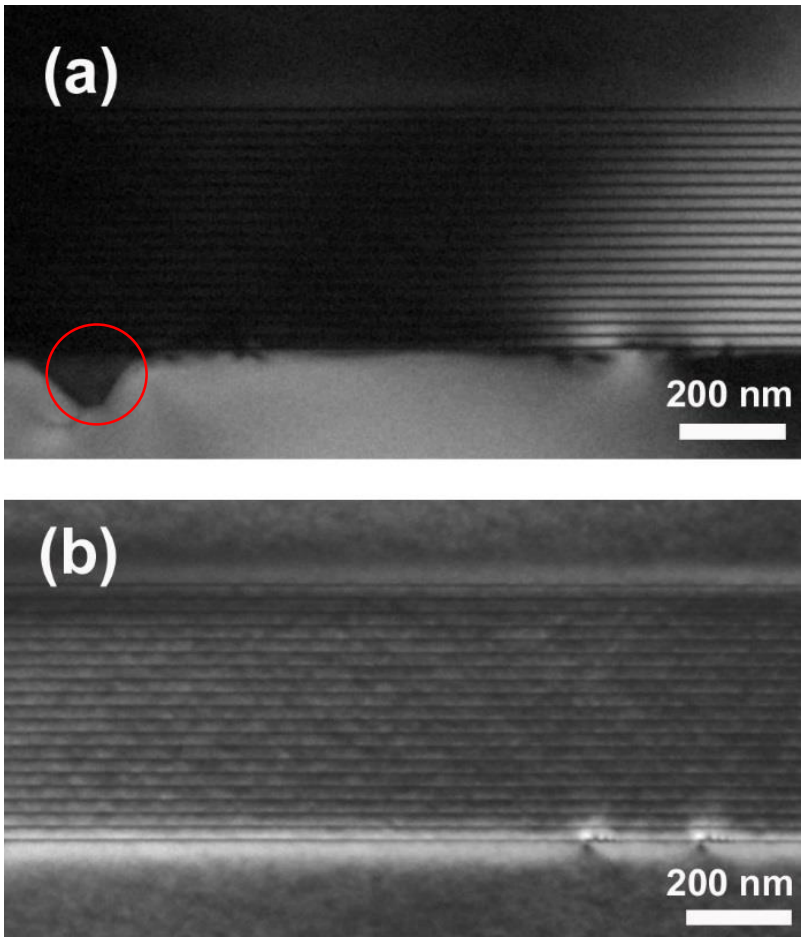

Figure 4.5: Dark field (200) cross-sectional transmission electron microscopy images of (a) InGaAs/GaAs QW in the QW solar cell and (b) multilayer SML-QD in SML-QD solar cell.

The transmission electron microscopy (TEM) results were kindly supplied by the University of Warwick. TEM imaging examines the cross-section of the solar cells under dark field mode and reveals the structure deformation in the (100) growth directions, shown in Figure 4.5(a) and (b). The formation of InAs agglomerations will partially compensate the lattice mismatch between InAs and GaAs. The undulated surface formed by elastic strain-relaxation is less prominent for the SML-QD solar cell. Therefore, the accumulation of strain in the multilayer QWs not only leads to a rougher surface but also results in the defect formation directly below the multiple QWs to relax the strain, as indicated by a red circle in Figure 4.5(a). There could be

several reasons: (1) the lattice-mismatching strain develops many point defects which forces a greater lateral pull of atoms/grains resulting in a sharp crack to the surface; (2) the thermal expansion during temperature changes in the growth process causing strain-induced defects and the successive layers gradually deform on the surface.

4.5 **Optical Characterisation**

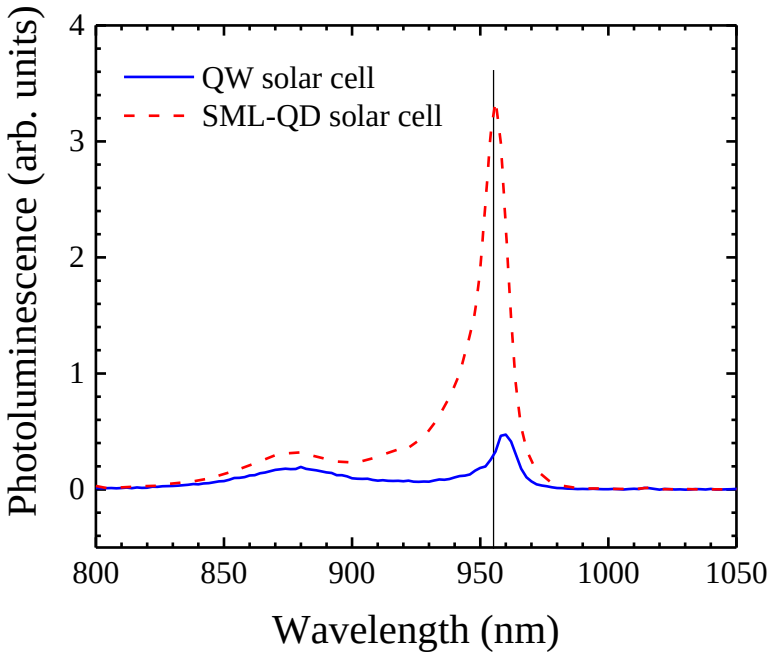

Figure 4.6: (a) PL spectra of the SML-QD solar cell and QW solar cell measured at 300 K.

Figure 4.6 shows the PL emission spectroscopy for SML-QD solar and QW solar cell at room temperature with fixed excitation power of 30 mW. Both solar cells have a peak emission at ~960 nm at room temperature, but SML-QD emission has a very slight blue-shift. Repeated measurements have shown that this shift is consistent, however marginal variance exist depending on the position of the wafer measured from. Nonetheless, the SML-QD PL emission energy is usually much higher due to its shorter height compared with SK-QD. This is consistent with results reported from Kim et al [120]. The FWHM of the SML-QD emission at room temperature is ~13 nm, which indicates good uniformity of the SML QDs. It can be clearly seen that the

peak emission intensity of the SML-QD solar cell is much higher than the QW solar cell, which indicates a more efficient radiative recombination process is taking place in the SML-QD solar cell. This may also suggest that the recombination pathway of the QW solar cell could be obstructed by the presence of NR recombination centres. The peak at 870nm corresponds to the emission of GaAs material, where SML-QD solar cell has a higher emission intensity at this peak compared to the QW solar cell. This may be indicative that the SML-QD formation assists the growth of subsequent GaAs layers with good material quality. As a measure of material quality, which is defined as the probability of the recombination event being radiative, the better emission intensity of the SML-QD solar cell is indicative that it has an improved material quality attributed by the growth mechanism. This is supported by the AFM and TEM results, which points to a degraded material quality of the QW solar cell and a relatively better material quality of the SML-QD solar cell. Since the rougher topology of the QW solar cell must be a result from all the stacked layers underneath the surface, it is possible that the GaAs layers that made up the various layers in the solar cell is affected by the growth process where the crystal comprises many non-radiative recombination sites, which explains the lower emission intensity at the GaAs peak.

4.6 **Thermal Activation Energy Estimation**

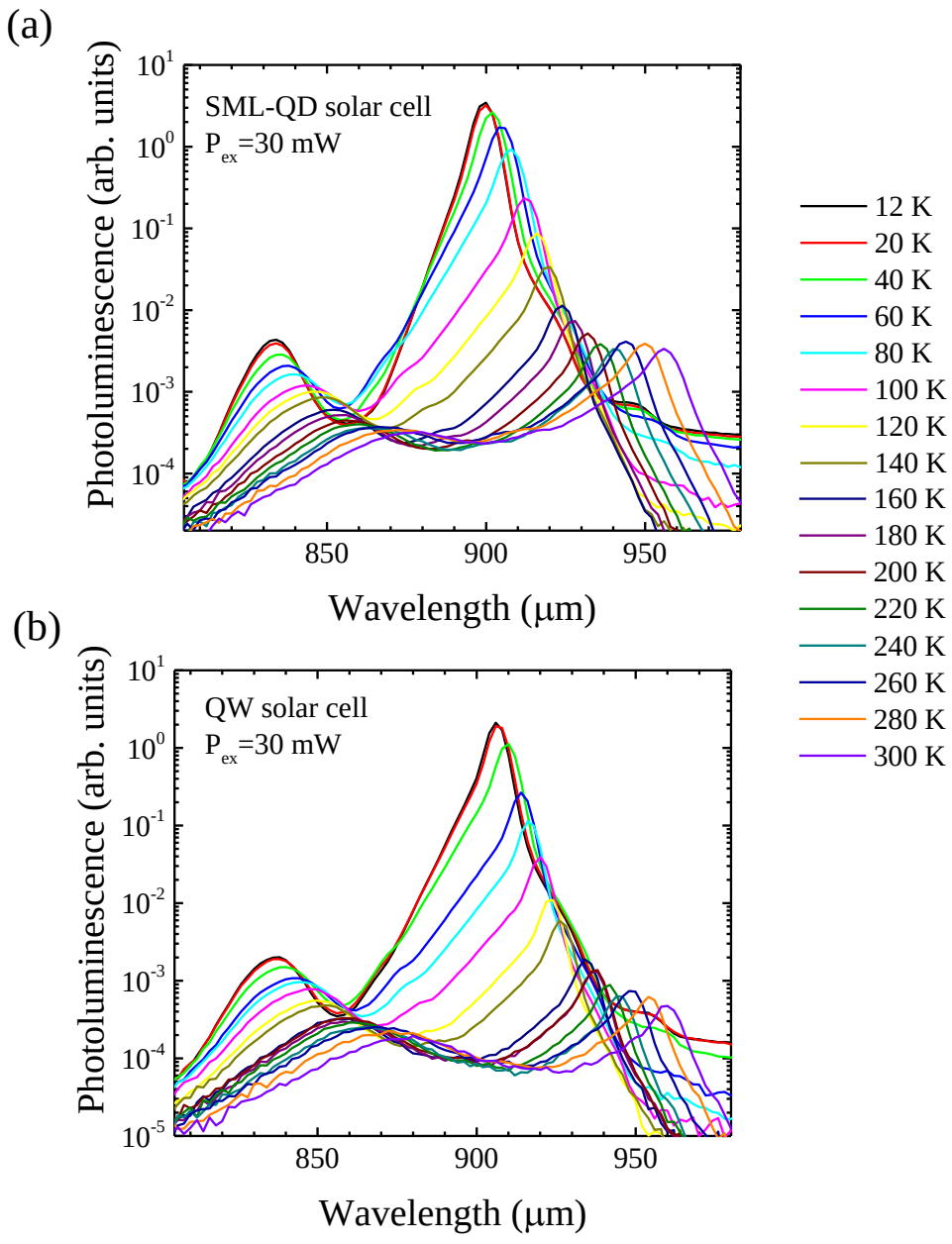

Figure 4.7: Temperature-dependent photoluminescence measurement of (a) SML-QD solar cell, (b) QW solar cell from the range 12 to 300 K using a constant laser excitation power at 30mW, plotted in logarithmic scale.

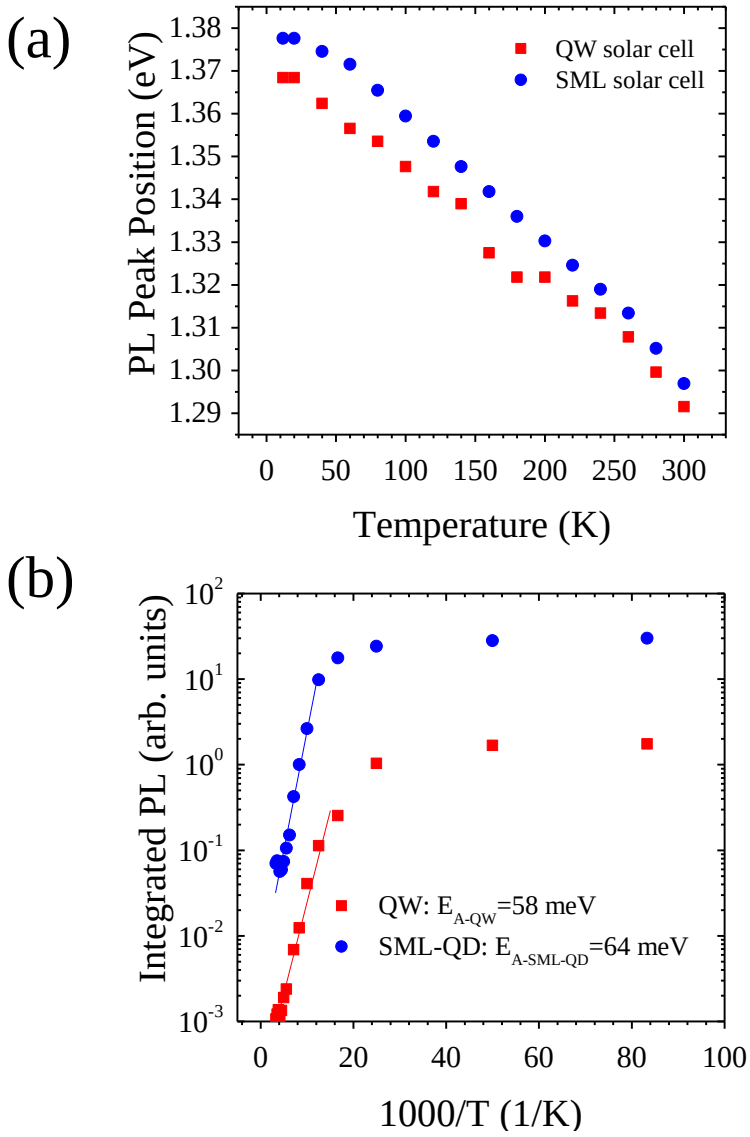

Figure 4.8: (a) PL peak as a function of temperature derived from temperature dependent photoluminescence measurement and (b) Arrhenius plot from the integrated PL intensity as a function of inverse temperature.

Figure 4.7 shows the measurement of temperature-dependent PL of QW solar cell and the SML-QD solar cell, fixed at 30 mW excitation power. The SML-QD emission is higher compared to those of QW between 140 to 300 K. Towards 12K, the SML-QD and QW emission intensity became similar. This provides evidence to deduce that carriers in the QW suffers non-radiative recombination at 300 K. The suppression of

thermal energy when the sample is subjected to low temperature reduces the trapping of carriers at non-radiative sites and increases emission intensity. The SML-QD and QW spectra blue-shifted with an increase in emission intensity as the temperature was reduced from 300 to 12 K. This is due to the widening of the effective bandgap of the quantum structure, which results in higher energy photon emission. In the cryogenic condition, the thermionic pathway which allows carrier escape in the quantum structure is suppressed. As a result, the effect of NR recombination is also suppressed.

Figure 4.8(a) shows a plot of the peak position of the emission spectra of SML-QD and QW over the range of temperatures. The difference in the change of PL intensity as a function of temperature indicates a different rate of thermal quenching of both solar cells. Thermal quenching is due to loss of energy transfer and it increases with increasing phonon frequencies. Difference in the thermal quenching rate is a clear indication that the dominant energy transfer mechanism of the carrier in SML-QD solar cell and QW solar cell is different. This is likely due to a higher concentration of defect traps in the QW solar cell which releases phonon emission.

To further analyse this data, an Arrhenius plot was generated with the integrated PL emission of the GS energy of the QD using Gaussian fitting, therefore only the plot shows the integrated PL intensity that corresponds to only the quantum structure over the inverse of the temperature as shown in Figure 4.8(b). The plot was fitted with the Arrhenius equation:

$$I(T) = \frac{I_0}{(1 + A \exp E_A/KT)}$$

where I is the integrated PL intensity, I_0 is the PL intensity at 12K, A is a constant and E_A is the activation energy. K is the Boltzmann constant and T is temperature. The fit is limited to the higher temperatures only because carrier escape will be completely inhibited at low temperature. Therefore, the boundary for the fitting is between 300K to ~80K. Due to the sensitive gradient of the fit that determines the activation energy, the best fit was guided by minimising the sum of the least square residuals and

reducing the range of the fit if necessary. From this plot, the activation energy extracted for QW solar cell and SML-QD solar cell is 58 meV and 64 meV, respectively. The two activation energy is considerably very close to each other, but the slightly higher thermal activation energy for the SML-QD solar cell could be true as it suggests three-dimensional confinement in InAs rich regions leads to stronger quantum confinement. Compared with InAs/GaAs SK-QD which typically has an E_A of 200 meV, the thermal activation energies of both QW and SML-QD solar cell are relatively small, which indicates that the GS is very close to the band-edge of the barrier material. Similar work from Xua et al has reported an activation energy as low as 31meV for SML-QD [128]. On the other hand, it is also possible that the high density of defects states of the QW solar cell lying under the CB decreases the thermal activation energy. In correlation to the AFM results, the QW solar cell with a rougher crosshatch surface compared to SML-QD solar cell supports this. The PL results supports that SML-QD solar cell has a better material quality than the QW solar cell. In respect to the solar cell structure, the strain accumulation by lattice mismatch epitaxy has an effect to these findings. They point towards the differences in the strain relaxation mechanism of SML-QD and QW solar cell during the growth. It is possible that SML QD structure holds a geometrical favourability due to the parquet shape, reducing the defect density leads to fewer NR recombination centres and improved recombination efficiency.

4.7 **EQE Measurement**

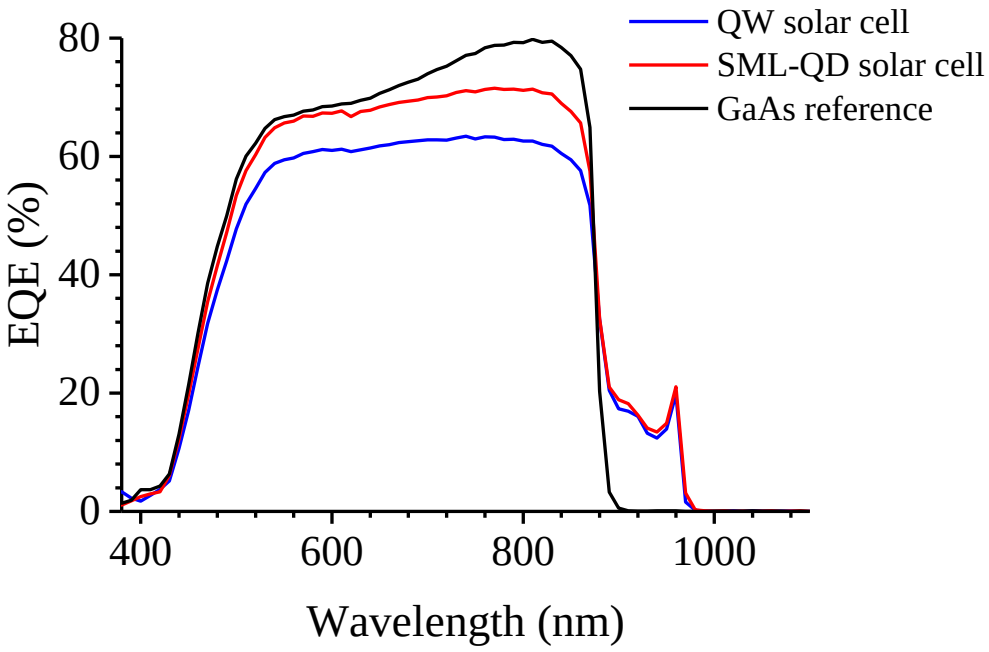

Figure 4.9: External quantum efficiency measurement of the SML- QD solar cell and QW solar cell measured at room temperature under zero bias.

Figure 4.9 shows the result of the EQE measurements for the QW and SML-QD solar cell. The spectral response for both solar cells has a similar shape with absorption coverage extended below the GaAs absorption edge of 870 nm. The extended absorption goes down to about ~960 nm, which corresponds well to the PL peak emission for both SML-QD and QW, and confirms a sub-bandgap absorption by both of the solar cell. The SML-QD solar cell reached a peak EQE of ~70% at supra-bandgap energy whilst for QW solar cell only reached about 60%. Normally, blue light is absorbed at the surface of the solar cell. The GaAs reference solar cell and the SML-QD solar cell both have similar blue light absorption strength. However, the QW solar cell shows a decreased EQE response to the blue light. With the AFM and the PL results, this suggests that the emitter of the QW solar cell has very poor photocurrent generation due to propagation of defects into the emitter region, but this is less severe for the SML-QD solar cell. It is evident that between the absorption coverage of 400-870 nm, SML-QD solar cell has a higher EQE response than QW solar cell. Since both

solar cells share an identical p-i-n structural layout with the same region thickness and material contents in the i-region, the difference in the EQE response suggests that carrier extraction in QW solar cell is impeded by non-radiative recombination sites which reduces the carrier mobility, which in turn affects the diffusion length. For a poor quality material, crystal defects dictates the photocurrent by impeding the carrier extraction pathway. This is supported by the evidences provided by PL and AFM results which shows poorer emission intensity and rougher surface of the QW solar cell. Conversely, the result suggests a better crystal quality in SML-QD solar cell is achieved, which is supported with the evidence of higher PL emission intensity and spectral response. Interestingly, the sub-bandgap region of the EQE result shows a similar spectral strength by both solar cells. It is almost as if the both solar cells have the same photocurrent generation. Whether the lower activation energy of the QW helps the photocurrent generation due to a higher amounts of carrier escape remains a question.

Nonetheless, in contrast, the relatively high spectral response of the SML-QD solar cell compared with QW solar cell is likely due to lower defect density, which reduces the impedance effect. This maintains the carrier diffusion length and therefore has a higher collection probability. From AFM and PL measurements, the improvement of the crystal quality of the SML-QD solar cell is due to strain relaxation by forming InAs agglomerations and suppressing defect formation. Compared with QW solar cell, the SML-QD solar cell does not have a very prominent non-radiative recombination process. This leads to improved collection efficiency of photo-generated carriers as evidenced by the EQE results.

4.8 **J-V Characteristics**

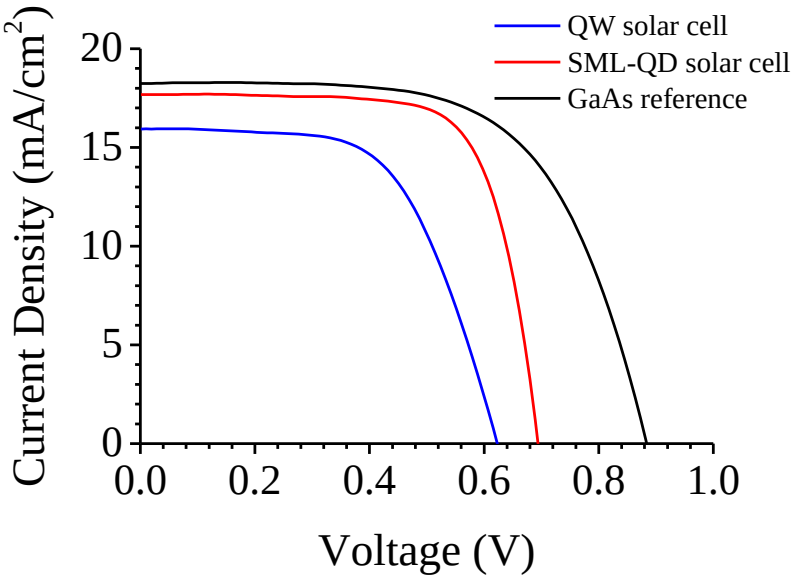

Figure 4.10: Current density versus voltage characteristics under one sun AM1.5G illumination of the SML-QD solar cell and QW solar cell.

Figure 4.10 shows the J-V characteristics for SML-QD and QW solar cells with the GaAs reference solar cell to provide a baseline. The J-V characteristics were measured under 1 sun illumination at 25 °C. The GaAs reference solar cell has a J_{SC} of 18.1 mAcm^{-2}. The SML-QD solar cell has a J_{SC} of 17.7 mAcm^{-2}, similar to the GaAs reference solar cell, whilst the QW solar cell has 15.9 mAcm^{-2}. The increased J_{SC} of the SML-QD solar cell from the QW solar cell is consistent with the EQE result which shows a larger EQE spectra. For the QW solar cell, there is a likely possibility that the defective sites within the QW have affected the carrier extraction. Therefore the J_{SC} of the QW solar cell is reduced. The point defects or dislocations, acting as non-radiative recombination centres, may trap the carriers causing it to recombine. Poor carrier movement through the solar cell and poor contact resistance are both possible reasons to explain the higher series resistance (R_S) of the QW solar cell, as seen on the slope at V_{OC}.

A V_{OC} of 0.62 and 0.69 V is recorded for QW and SML-QD solar cells, respectively. Since the same amount of InAs/GaAs contents has been used for both SML-QD and QW structure, the improvement in V_{OC} indicates the difference in the carrier dynamics between both solar cells. Although it is very tempting to relate this to the high confinement potential of the SML-QD solar cell, the difference between the SML-QD and QW emission peak wavelength at room temperature is insignificant, therefore it is unlikely that the energy band structure differences could account for a 50 meV difference in the V_{OC}. It has been reported that formation of dislocation in the QW solar cell could be the factor attributed to the reduced V_{OC} [129]. Voltage loss in QW solar cell can be explained by the high recombination events which increases the forward bias diffusion current. Note that the R_S does not have an effect on the V_{OC}, however, shortening of the carrier diffusion length can lead to the reduced minority carrier density at the junction edge.

4.9 **Chapter Summary**

There are two ways to enhance J_{SC} for QD solar cell structurally, one by increasing the areal QD density [130] and the other by increasing the number of QD stacks [113]. The latter has seen problems in strain-induced dislocations due to gradual strain build-up. The association of strain-induced defects of QD in the matrix barrier is known to limit the current density, despite attempts of using strain compensation layers to better match the lattice of the spacer layer material [114]. SML-QD structure investigated in this chapter shows a better optical performance compared with the QW solar cell. The improvement is correlated with the quality of the crystal lattice. The PL emission intensity and AFM results provides evidence to support this. The crosshatch morphology on the SML-QD solar cell surface is less prominent than the QW solar cell, which suggests less strain accumulation in the SML-QD structure. The defective formations are significant in the QW structure, which leads to poor crystal lattice in QW solar cell as the high defect density acts like NR recombination centres. As a result, the QW solar cell saw degradation to the optical and electrical performance. In contrary, SML-QD solar cell in this work has demonstrated the possibility of enhancing the light absorption via increasing the number of stacking of QD. The

outcome has lower defect density due to an alternative strain relaxation mechanism. Therefore more layers of QD material to enhance absorption will benefit the optimal design of solar cells.

The activation energy (E_A) was calculated using the Arrhenius plot showing a value of 64 meV and 58 meV for SML-QD solar cell and QW solar cell, respectively. The slightly larger E_A for the SML-QD solar cell suggests a stronger quantum confinement caused by the formation of 3D confinement in InAs rich regions. However, InGaAs/GaAs SML-QD system requires further modification in order to contribute to the IBSC [49], as the small E_A would allow thermionic excitation to dominant the photo-excitation. Sengupta *et al* has demonstrated capping of InAs SML-QD using different barrier material to enhance the thermal activation energy. Using high barrier material such as InAlGaAs-GaAs can enhance the E_A to as high as 109 meV [131]. Some QD IR-photodetectors have made the SML-QD absorbing layer effective by applying high barrier layers with Al components to form a dot-in-a-well (DWELL) structure, which raises the carrier confinement for better light absorption [117]. It would be interesting to see the effect of applying the same method for SML-QD solar cells.

The results in this chapter shows that it is possible to increase the stacking of the SML-QD periods without inducing significant material degradation as compared with QW solar cell. This is important for the continuation of adding the QD layers as an absorbing material. Primarily, this helps to improve the solar cell photocurrent via absorption of the lower energy coverage. Furthermore, the possibility of growing QD in the absence of WL has given SML-QD a structural advantage. The growth of SML-QD avoids a wetting layer formation, which helps the SML-QD solar cell to preserve its voltage output. This is evidenced in AlAs capped QD layers reported in previous studies [122], which removed WL and achieved voltage-recovery from ~0.7 V to 0.8V. Unfortunately, using AlAs capping material to the QD forms local defects around the dots, which increases non-radiative recombination processes. Therefore, a full voltage recovery cannot be realized. The SML-QD may provide an alternative approach by preventing WL formation in QD solar cells.

In the past, comparison work between 5 layers of QDs with 50 layers has shown degraded conversion efficiency due to deteriorated crystal material of the solar cell [102]. These results demonstrated here, comparing SML-QD and QW solar cells, show the importance of reducing interior stress in semiconductor solar cells with quantum structures to enable efficient extraction of photo-generated carriers in the solar cell.

Chapter 5

Voltage Recovery from Direct Si-Doping

5.1 Introduction

The QD energy states as an IB provide an additional optical pathway for carrier excitation. Two-step photo-excitation is explored as a possible pathway to efficiently utilise sub-bandgap photons. Ideally, this process will not affect the voltage output of the host material [48, 49], and the additional photocurrent could improve the conversion efficiency. However, although the QD solar cell is a promising material system to establish IBSC, the photocurrent improvement contributed by the QD is compromised with the reduction in the voltage output of the solar cell. This added another limiting factor to the IBSC conversion efficiency. The loss in voltage is due to thermal pathway generated between the QD energy states and the CB. This is profound in the commonly used InAs/GaAs QD system, where carriers in the QD energy states are too close to the CB of the host material, and with background thermal energy from room temperature the IB carriers are tightly coupled to the CB, which reduces the split of the quasi-Fermi level, hence the voltage. Therefore, the QD solar cell does not behave with ideal IBSC operating principles unless cryogenic conditions are applied to suppress this thermal-coupling effect. The effect of this prevents QD solar cells from surpassing the Shockley-Quiesser limit. In the past, many researchers

have attempted to counter this problem by using high bandgap materials as capping layers such as InAlGaAs [31], AlAs [122] and AlGaAs [87] to enlarge the quantum confinement of the QD, which separates the IB further from CB. They have shown increased thermal activation energy for the carrier in the QD which led to a reduction in the rate of thermal carrier escape. However, a complete voltage-recovery on a QD solar cell device has not been reported. To date, laboratory results QD-IBSC has only shown conversion efficiency merely exceeding its reference cell without QD by only 1% at room temperature [127]. Nonetheless, voltage loss in QD-IBSC requires fabrication attention along with other techniques, such as increasing absorption and light-trapping [133] to further improve the solar cell efficiency.

5.1.1 Open-circuit voltage loss in QD solar cells

The voltage loss problem in IBSC is a notorious issue specific to QD solar cells. It was even thought that QD-IBSC would be difficult to be made into practical applications due to the difficulty to maintain the V_{OC}. Primarily for QD-IBSC, the problem is derived from the QD energy states and the continuous states of the CB. Especially in an InAs/GaAs QD system, the QD energy states lie very closely to the CB energy states. This creates a thermal channel for the carrier to rapidly escape or relax between the QD energy states and the CB of the host material, which results in a strong thermal coupling between the electronic states in the QD to the continuum states in CB. In other words, the IB forms a continuum with the CB. The effect of this lowers the quasi-Fermi energy level of the CB which determines the voltage output of the solar cell [32, 33]. Furthermore, the thermal-coupling which allows carriers to escape the QD energy states suppresses the IB→CB transition via photo-excitation. This reduces the probability of a second-photon excitation in the IBSC. Although this thermal pathway along with a tunnelling mechanisms would allow the extraction of a sub-bandgap photocurrent, it does not allow voltage preservation because it lacks the free-energy provided by the second [20]. For a bulk single-junction GaAs solar cell, the V_{OC} is typically around 0.9 V, but when the same structure is implanted with InAs/GaAs QD layers in the intrinsic region the V_{OC} is reduced to typically 0.7 V at room temperature. By suppressing the thermal-coupling effect by applying cryogenic

conditions to the QD-IBSC, a voltage recovery has been observed [134]. It has also been shown that the reduction in V_{OC} can be recovered by the use of concentrated illumination, which enhances the rate of photogeneration to overcome the effects of rapid carrier recombination [135]. This suggests that voltage recovery can be achieved by optimising the carrier dynamics of the QD-IBSC system.

Apart from the thermal coupling issue between the QD energy states and the CB in the QD-IBSC, the holes of the QD also requires attention. Holes in the QD usually contains a high effective mass, which leads to substantially shorter spacing of the VB states. This is commonly found in type-I QD configurations, which is when the confinement potential for electrons and holes are vertically aligned. As a result, the VB offset in the confinement potential contains many states and forms a continuum. This give rise to a continuous band within the confinement potential, which connects with the VB of the host material. The effect of this leads to a shift in the quasi-Fermi energy level for the VB of the host material [136, 137].

Another factor that could result in a loss of voltage in a solar cell is the presence of NR recombination. This is not uncommon for QD solar cells grown in SK-growth mode, which is often employed as a reliable technique to manufacture self-assembled QDs. However, since this is a strain-induced technique, it could distribute defects around the QD and the matrix of the barrier material. As a result, limits the optimum crystal quality in terms of optical and electrical performance. The defect sites could either trap the carrier or impeded the carrier flow. Trapped carriers usually losses the energy via thermal emission, hence it is a NR recombination event. In an InAs/GaAs QD solar cell, the presence of defects could reduce the minority carrier diffusion length which reduces the V_{OC}. In addition, NR recombination events can also be hosted by some coalescence dots in the areal QD population as a result of poor growth. To prevent the formation of coalescence dots, low coverage of QD materials can be used during the growth. It has been claimed that this method has also achieved voltage-recovery [137]. On the other hand, strain-compensation techniques has been used in QD solar cells to suppress strain build-up and prevent a high the density of NR recombination centres but the voltage recovery was not sufficient [129, 138].

The presence of WL for self-assembled QDs grown in SK-mode also reduces the V_{OC}. The WL consists of continuum states and reduces the confinement potential of the QD. QD solar cells with WL removed, confirmed by transmission electron microscopy imaging, has shown a small voltage-recovery [122]. This provided strong evidence to show the voltage output of a QD solar cell was affected by the presence of WL, which could be due to carrier communication between the QD and the WL energy states. Furthermore, when WL was removed from the QD layer the PL emission spectra blue-shifted [122], which suggests a change in the confinement potential. Hence, the communication between the WL and the QD is an interesting pathway to target. Inducing changes to the QD layer may impact this communication pathway. In this chapter, the effect of Si-dopants introduced into the QD layer is studied.

5.1.2 Direct Doping to Quantum Dots

One of the pre-requirements of IBSC operation is to have the electronic state(s) in the IB material partially filled with electrons [140, 141]. The IB must be initially occupied with electrons to generate an IB→CB optical transition. One of the reason for the absence of IB→CB absorption is because the IB is empty of electrons [141]. Normally, electronic wave functions in the QD are large enough to permit a high electric dipole matrix elements. However, if the IB is empty then the IB→CB optical transition pathway will become inactive. Therefore, doping directly into the QD material is needed to supply electrons to the energy states in the confinement potential.

Most of the VB→IB absorption takes place between localised states in the QD at the VB and the localised states in the IB. If the IB is not partially filled, pumping a second photon will be very difficult and the voltage will be limited by the position of the IB rather than by the position of the CB [141]. This might help to explain the loss in voltage in QD-IBSCs. It is therefore important to study the effect of supplying electrons to the QD and what happens when IB is partially filled. However, this method is not commonly reported because doping into the QD region may lead to imperfections by introducing impurities to the depletion region.

Sablon et al has demonstrated an increase in photocurrent after growth QD structures with n-type doping and modelled the comparison between n-type and p-type doping [65]. Okada's simulation work shows the relationship of the electron density in IB and the electrostatic potential profile [51]. Si-impurity doping in QD solar cell fabricated with strain-compensation layers shows high EQE response below 880 nm which resulted in improvement in the photocurrent [36]. Interestingly, some work with direct doping highlights the recovery of V_{OC} [142]. State-filling PL experiments confirmed that n-doping in the self-assembled QD populates the lower electronic shells with carriers [27]. In this work, the doping technique is employed to induce changes to the quantum system in the solar cell. Some results in this chapter are published in the journal *Nano Energy* titled **"**Voltage recovery in charged InAs/GaAs quantum dot solar cells" [42]. It is expected that this technique may impact the QD and WL communication pathway and help to achieve voltage recovery. In order to achieve this, n-type dopants are deposited during the nucleation process of the QD growth. This supplies electrons to the QD and allows the confined states to be filled.

5.2 **Growth and Fabrication**

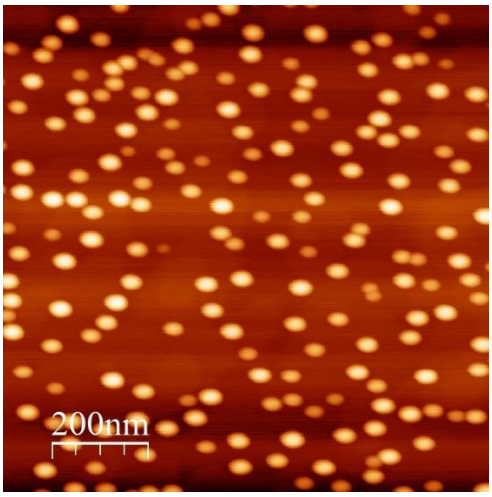

Figure 5.1: AFM image (1x1um^2) of an uncapped InAs/GaAs QD sample using 2.35 ML of InAs coverage which yielded ~3.5 x 10^{10} cm^{-2} QD areal density. This QD density value was used to calibrate for the doping density.

The QD solar cell in this work contains 20 QD layers with n-type dopant directly doped into each QD. First, to calculate the dopant concentration needed to generate an array of QD with the desired number of electrons in each dot, a conventional InAs/GaAs QD array was grown under SK-mode in the MBE. 2.35 ML of InAs QD material was deposited onto the GaAs with a growth temperature of 470 °C measured by a pyrometer, and left uncapped. An AFM image of the uncapped QDs is shown in Figure 5.1. The AFM image shows a QD density of ~3.5 $x10^{10}$ cm^{-2} with no coalesced dots. Therefore, the doping densities were calibrated using this QD sheet density value. Si impurity was chosen to be the n-type dopant for the QDs in this work because it is less amphoteric than Ge and does not have a serious segregation problem [142]. Each Si atom deposited into the QD would supply an electron to the QD. The amount of Si atom deposition is controlled by the opening time of the shutter of the Si effusion cell. The doping densities of 0, 2.1 $x10^{11}$, 4.2 x 10^{11}, 6.3 x 10^{11} and 8.4 x 10^{11} cm^{-2} were deposited just before reaching the critical thickness during the SK-growth to achieve QD doped with 0, 6, 18 and 24 electrons per dot. The nucleation process of the InAs layer would incorporate all the Si atoms into the InAs layer and the Si-atoms are expected to not diffuse into the GaAs barrier layer. The insertion of Si-dopants should have no effect on the nucleation process, and no distortion to the QD shape is expected.

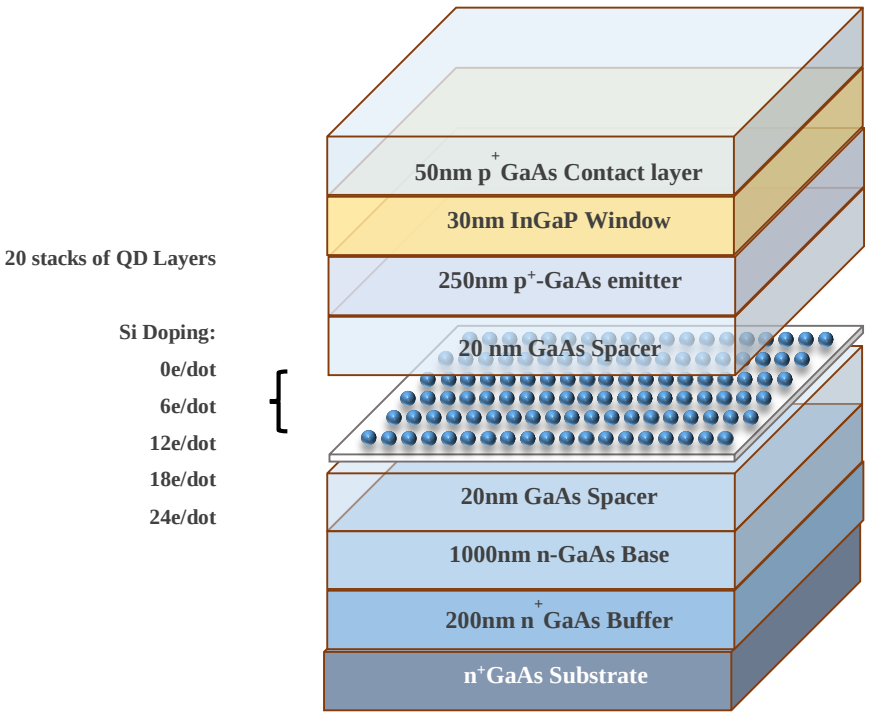

Figure 5.2: A Schematic diagram to illustrate the structure of a p-i-n solar cell with 20 x InAs/GaAs QD layers grown via Stranski-Kranstanov mode. The QD layers were doped with different Si-concentrations.

All solar cells were grown by the MBE system on an n^+-GaAs (100) substrate as shown schematically in Figure 5.2. The QD solar cells had a p-i-n structure consists of a 200 nm GaAs buffer layer with Si doping density of 1×10^{18} cm^{-3}, 1000 nm GaAs base with Si doping density of 1×10^{17} cm^{-3}, 420 nm intrinsic region, 250 nm GaAs emitter with Be doping density of 2×10^{18} cm^{-3}, 30 nm InGaP window layer with Be doping density of 2×10^{18} cm^{-3}, and 50 nm GaAs contact layer with Be doping density of 1×10^{19} cm^{-3}. The intrinsic region of the QD solar cells contained 20 stacks of QD layers separated by a 20 nm GaAs spacer. The QDs were grown by the SK-mode at substrate temperature of ~470 °C. High-growth-temperature GaAs spacer layers were applied during growth of QDs to suppress the formation of dislocations. During QD growth, direct Si-doping was carried out with dopant densities of 0, 6, 12, 18, and 24 electrons per QD and the QD solar cells were named as 0e, 6e, 12e, 18e, and 24e QD solar cells, accordingly. As mentioned above, the doping density is calibrated using a QD sheet density of $\sim3.0\times10^{10}$ cm^{-2} as shown in Figure 5.1. Two GaAs reference solar cells share the same growth conditions without growth of QDs. One GaAs reference

solar cell, 18e GaAs solar cell, was doped in the intrinsic region same as the 18e QD solar cell.

The samples were cleaved from the wafer and optically characterised with PL measurements. Temperature dependent PL measurement was performed with the sample mounted inside a Helium cooled cryostat at ~10K under 40 mW excitation power. The samples were processed into solar cell devices with thermally deposited back and front electrode contacts. The back contact consists of Ni-AuGe-Ni-Au metals of 10-50-20-200 nm thickness and the front contact AuZn alloy of 100 nm thickness.

5.3 **PL Characterisation**

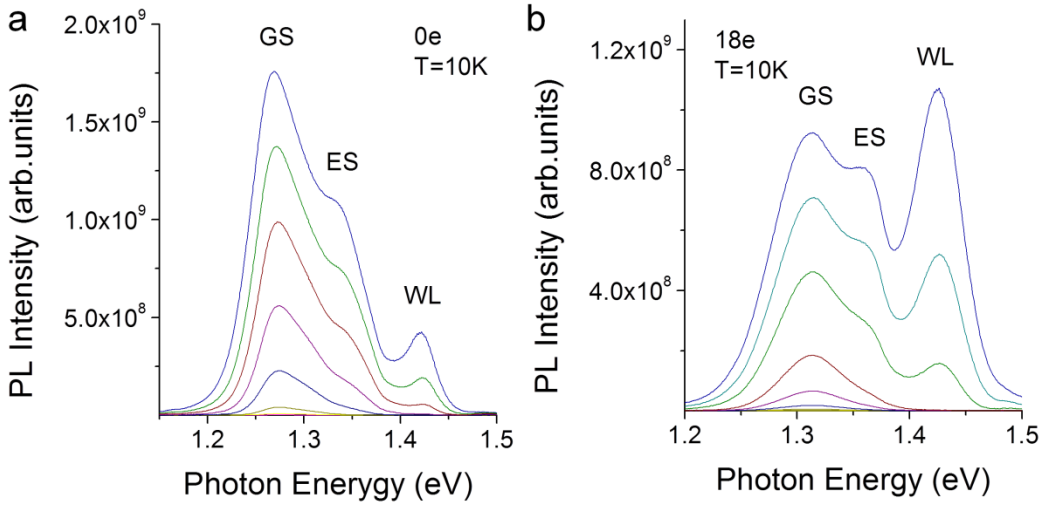

Figure 5.3: Excitation power dependent PL spectra of (a) 0e QD solar cell and (b) 18e QD solar cell, measured at 10 K with laser excitation power from 0.06 Wcm^{-2} to 10^4 Wcm^{-2}.

Figure 5.3 compares the excitation power dependent PL spectra of 0e QD solar cell and 18e QD solar cell measured at 10 K, plotted as a function of photon energy (eV). The laser excitation power is varied from 0.06 W/cm^2 to 104 W/cm^2. At 10 K, the 0e QD solar cell clearly shows a state-filling process: first, only emission from ground states (GS) is observable, then the PL emission from the excited states (ES) appears in the spectra, and finally, the WL emission shows up. However, from the 18e

QD solar cell, the sequence is different: the WL emission appears at a much lower excitation power than ES emission. The onset of WL emission prior to ES emission is a strong sign of decoupled WL/QD system.

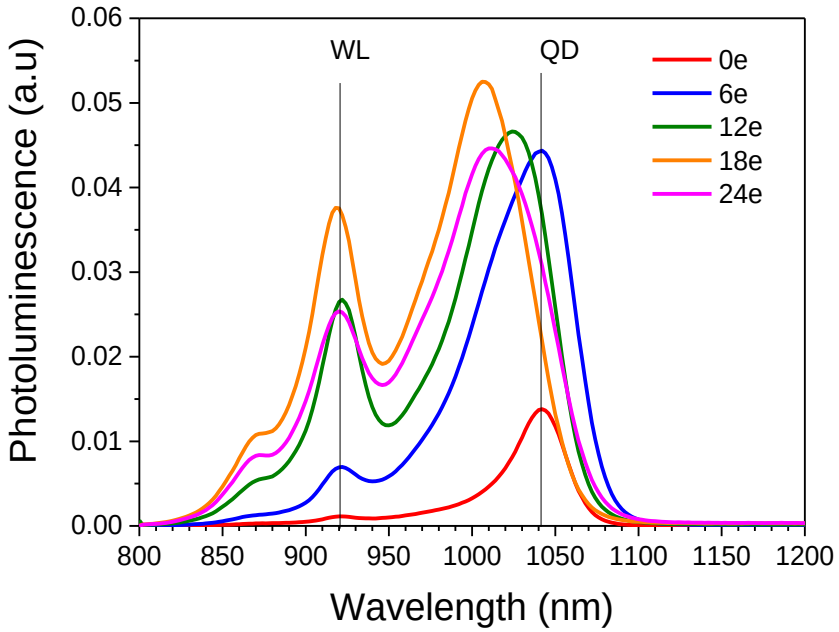

Figure 5.4: PL spectra of the 0e, 6e, 12e, 18e and 24e QD solar cells at measured at room temperature under fixed excitation power of 28 mW, labelled with QD emission at GS and WL emission.

Figure 5.4 shows the PL result for the doped and undoped QD solar cells measured at room temperature. The emission at 860 nm and 920 nm corresponds to the GaAs spacer layer emission and the wetting layer emission. The emission below this wavelength corresponds to the QD emission. It can be seen that the QD emission peaks at the wavelength of 1040, 1040, 1025, 1008 nm for the as-grown sample (0 e/dot), 6, 12 and 18 e/dot, respectively. These values indicate there is a clear blue-shift of the QD emission as the Si-impurity per dot increases, except at 24e/dot where no more blue-shift was observed. This blue-shift in PL emission in similar QD structure is also reported by several research groups [113, 146]. One of the explanations is that the Si-atoms created nucleation centres and facilitated the growth of smaller QDs which leads

to the blue-shift [147]. However, such a small ~20 meV blue-shift is unlikely to be attributed by the size modification of the QD. On the other hand, the state-filling effect was proposed to explain this point, where increased concentration of carriers leads to occupation of low-energy states. This obeys the Pauli's exclusion principle where transitions between occupied states in the IB are forbidden, leaving the possible transition from higher energy states only. The relationship between the state-filling effect with the blue-shift of the QD emission spectra is agreed by several research groups [145, 148].

Considering a quantum dot is a zero-dimensional structure, the energy states exists only in discrete energies in a delta-like function as seen in Figure 2.14(d). The degeneracy of energy states for quantum dots allows only a density of states of 1, 3 and 3 for the GS, FES and second excited states (SES), respectively [149]. With Pauli's exclusion principle, each state only allows two electron occupation, which gives a maximum of 2 electrons in the GS, 6 electrons in the FES and 6 electrons in the SES. Compare this to the PL results, assuming the presence of all three energy states, by the 18e QDSC sample, the QD states are already fully saturated, which suggests that excessive electrons could leak out to the WL, possibly via thermal excitation.

The dramatic increase in PL emission after dopants were inserted indicates that the radiative recombination process is enhanced by the Si-dopants. One of the explanations to this is an increased quantum confinement is achieved by Si-doping which increases the radiative recombination pathway. Another explanation to this is the electrons supplied by the Si-dopants have helped to fill the defect traps in the crystal lattice which saturates the NR recombination centres and which therefore, make way for more radiative recombination events. This helps to explain the stronger WL emission of the peak at 920 nm also. However, at 24 e/dot the QD PL emission intensity began to drop by a small amount. This drop in the PL emission intensity is indicative that the Si-dopant as a form of interstitial or point defects became excessive and started to destruct the crystal lattice.

5.4 **J-V characteristics**

Figure 5.5 (a) shows the J-V characteristics of the solar cells measured under 1-sun AM1.5G illumination fixed at 25 °C. The curve shows that the QD solar cell without any dopants (0e/dot) has a similar device performance as the GaAs reference solar cell but the V_{OC} is significantly reduced from 0.921 V to 0.779 V. This is typically seen for QD solar cells. The QD solar cell (0e/dot) and GaAs reference solar cell have a similar J_{SC}, but the slight increase in J_{SC} of the QD solar cell (0e/dot) may be a result of the additional sub-bandgap absorption from QDs. The J-V curve also show a reduction in the J_{SC} in the J-V curve for the Si-doped QD solar cells. Figure 5.5(b) shows a plot of the J_{SC} as a function of dopant concentration superimposed with that of the V_{OC}. It can be seen that the gradual improvement in V_{OC} is compensated by the drop in J_{SC}. With increasing Si-doping concentration in the QDs, the V_{OC} has gradually improved from 0.777 V for the 0e QD solar cell to 0.898 meV, a 110 mV recovery of V_{OC} with Si-doping for the QD solar cell with 18 e/dot. This is a significant observation which indicates that Si-doping into the QD has an impact to the V_{OC} of the QD solar cell. However, at 24e/dot the V_{OC} dropped below that of the 18 e/dot. This corresponds to the drop in PL emission intensity shown in Figure 5.4. The drop in V_{OC} for 24e/dot could be a result of increased Shockley-Read-Hall recombination.

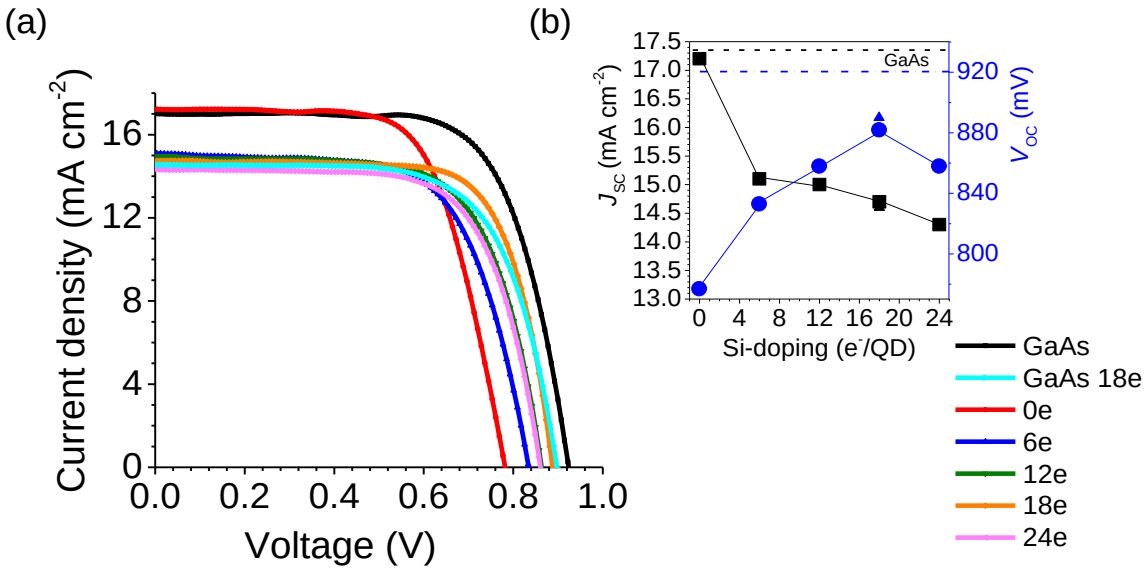

Figure 5.5: Current density vs. voltage curves for the Si-doped InAs/GaAs QD solar cells, and the doped and undoped GaAs reference solar cell under 1-sun AM 1.5g illumination (a). A plot of V_{OC} and J_{SC} vs the doping concentrations is shown in (b).

Figure 5.5(b) shows that a maximum voltage output is reached at 18e/dot with a V_{OC} of 898mV. Compared with the QD solar cell without doping (780mV), this marks a ~14% improvement. Considering the GaAs reference cell has a V_{OC} of 920 mV, the best Si-doped QD solar cell is only ~30mV away from the reference cell. The solar cell performance is summarised in Table 2.

The GaAs reference with Si-dopant concentration of 18e/dot has lower V_{OC} compare with that of the GaAs reference cell without Si-dopants. This helps to remove the ambiguity of where the V_{OC} recovery originated from. If the increase in V_{OC} is solely an effect of Si-doping, then the GaAs with 18e/dot should clearly show a V_{OC} higher than the GaAs reference solar cell. The results provide a proof that the improvement in V_{OC} after Si-dopant insertion into the QD solar cells is based on the InAs/GaAs QD layer, which suggests a modification to the electronic structure of the QD system took place.

Sample	J_{SC} *(mA/cm²)*	V_{OC} *(mV)*	*FF (%)*	*Efficiency (%)*
GaAs Ref	17.0	922	70.4	11.0
0e	17.2	777	67.8	9.1
6e	15.1	833	66.1	8.3
12e	15.0	882	68.4	8.8
18e	14.7	898	73.2	9.5
24e	14.3	890	69.3	8.5
GaAs+18e	14.6	922	69.1	8.9

Table 2: Summary of the current-density-voltage performance under AM1.5G of the fabricated GaAs reference solar cell, QD solar cell with 0, 6, 12, 24 and 24 e/dot and GaAs solar cell with 18e/dot.

The slight reduction in the V_{OC} of the GaAs solar cell with 18e/dot compared to the GaAs reference solar cell has ruled out the possibility that the voltage recovery, observed in this work, is due to the saturation of NR recombination centres by direct doping. On the other hand modulation doping, where the electrons are separated by the remote donor ions, and direct doping both claim to be capable of filling the IB states with carriers by inserting donor electrons into the confined states of the QD. Therefore, the improvement in the V_{OC} from the J-V characteristics, as a result of n-type doping, is very likely due to the effect of supplying the carriers from the dopant into the confinement potential.

5.5 **Dark Current Measurement**

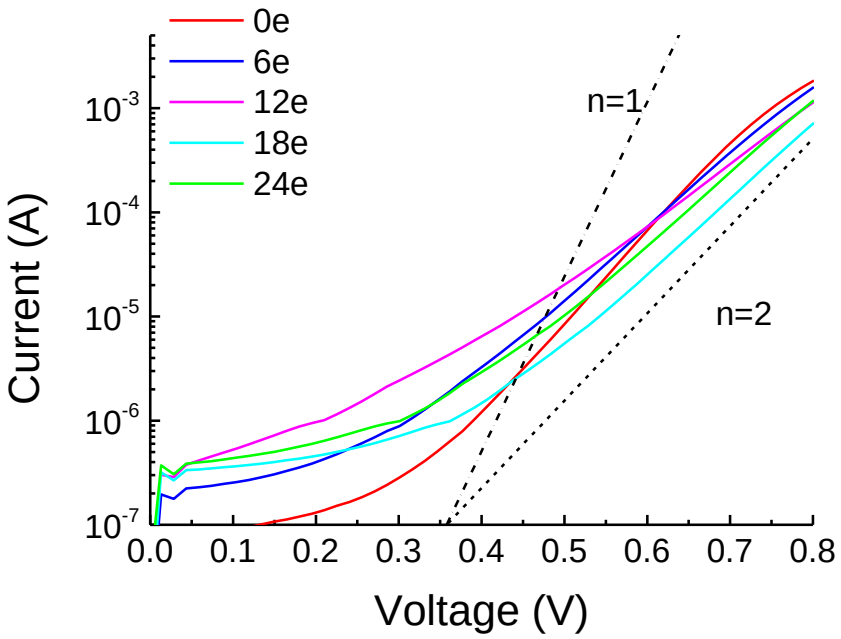

Figure 5.6: Dark current measurement plotted at semi-log scale with ideal cell ideality factor (n) for all the QD solar cells.

The dark current measurement was carried out on the QD solar cells at room temperature, as shown in Figure 5.6. All the cells have a size of 0.25cm^2.The QD solar cell without Si-doping (0e/dot) has an ideality factor between 1 and 2 as shown by the red line, and the doped QD solar cells have an ideality factor above 2 as seen by its falling gradient. This indicates a Shockley-Read Hall recombination becomes dominant in doped QD solar cells. This could be due to the impurity deep levels from the Si-dopants, which supports the PL results for the QD solar cell with 24 e/dot showing lower PL emission intensity. The contrast between the undoped and doped QD solar cell suggests the insertion of Si-dopants in the InAs QD could cause an increase in the Shockley-Read Hall recombination which could be due to Si-dopants forming interstitial or point defects in the solar cells.

5.6 **External Quantum Efficiency**

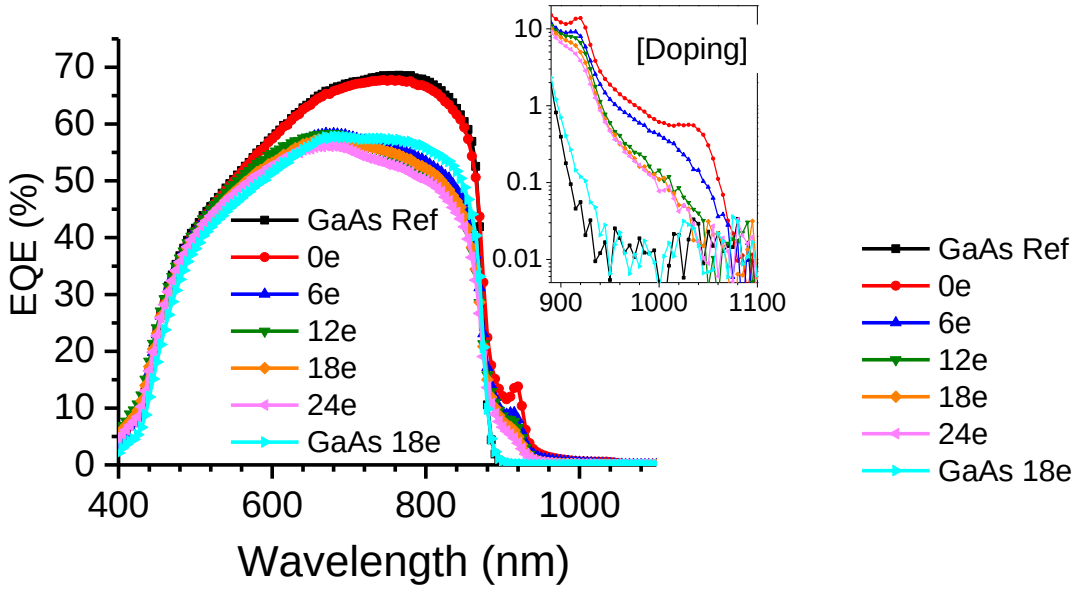

Figure 5.7: (a) External quantum efficiency of GaAs reference solar cell, doped GaAs solar cell (GaAs 18e) and InAs/GaAs QD solar cells with different doping concentrations and (b) an inset showing the magnified QD spectra.

Figure 5.7 shows the EQE spectra measured under zero bias at room temperature for all the solar cells in this work. The absorption coverage up to 870 nm corresponds to the GaAs material. All the solar cells have similar absorption for blue light, around 500 nm, which indicates the quality of the emitter of all the solar cells is as good as that of the GaAs reference solar cell. The supra-bandgap absorption strength at red light, around 800 nm, decreases for all the solar cells doped with Si-impurities, including the GaAs solar cell with 18e/dot. Supported by the result of dark current measurement shown in Figure 5.6, the reduction in the spectral strength is likely due to the crystal defects in the i-region or the base of the solar cell. Since the integration of the EQE spectra is directly representative to the J_{SC}, the drop in J_{SC} from the J-V results in Figure 5.5 is very likely attributed by the poor absorption of the GaAs material. This suggests that the defective sites are located in the GaAs material which deteriorated the quality of the GaAs barrier material around the QD. It is indicative that the direct doping technique promotes a carrier loss mechanism in the GaAs

material. The GaAs solar cell with same doping profile as the 18e QD solar cell confirms the reduction in J_{SC} of doped QD solar cells has to be linked to Si dopants.

On the other hand, the QD solar cells have extended absorption below the bandgap energy of the GaAs reference solar cell, which indicates that sub-bandgap photons are absorbed. The QD spectra is magnified in the inset of Figure 5.7. The 0e/dot QD solar cell serves as a reference baseline for the doped QD solar cell. The extended absorption attenuates around 1040 nm, which correlates with the PL results in Figure 5.4. Interestingly, as the doping concentration increases, the QD solar cell spectra decreases. The reduction in the QD spectra follows a blue-shift, which is consistent with the PL results. This confirms that Si-dopant in the QD introduces a state-filling effect. Electrons filling the low-energy states of the QD reduces the probability of optical absorption for low-energy photons [142]. Furthermore, the blue-shift of the QD spectra points toward the possible increase in the quantum confinement of the QD region as a result of Si-dopant insertion. This gives rise to the possibility of a potential barrier as described below.

5.7 **The Formation of a Potential Barrier from Si-doping**

The state-filling effect introduced by direct Si-doping is confirmed by PL results in Figure 5.4 and EQE results in Figure 5.7. They show that insertion of Si successfully donate electrons to the electronic states of the QD. The improvement in V_{OC} together with improved emission strength of the solar cells indicate an enlargement in the QD confinement potential. This enlargement in confinement potential is supported by the blue-shift of the sub-bandgap absorption seen in the EQE results. This leads to a picture that envisions a potential barrier which lies at the interface of the QD, which must be linked with the Si-dopants in the InAs QD layer. Reviewing the growth process, the Si-dopants are directly deposited on the InAs epilayer just before the nucleation process of the SK growth mode, therefore only some of the Si dopants are incorporated in the QDs and the rest remain in the wetting layer (WL), where free carriers are supplied to charge the QDs [148]. As a result, positively charged WL with ionized Si donors and negatively charged QDs are created by direct Si doping. This is

expected to form a potential barrier at the WL/QD interface that increases with doping density. The effect of this would directly help to suppress the electron thermal escaping.

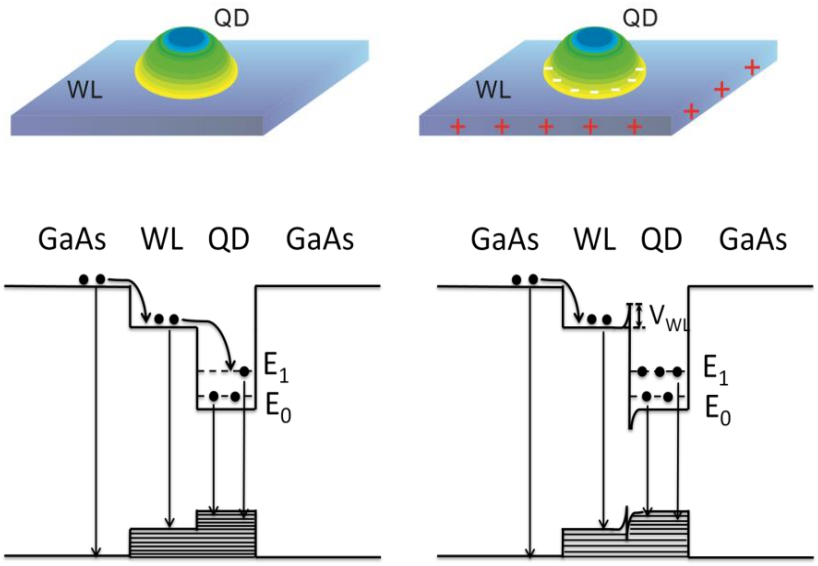

Figure 5.8: A schematic diagram illustrating the result of charges distributed in the QD and around the WL leading to the built-in potential in the QD solar cell.

To help visualise this, a drawing is supplied in Figure 5.8 to illustrate the assembly of negative charges in the QD with distributed ionized Si-donors in the WL. The band diagram shows how the distribution of the charges create the potential barrier between the QD and the WL. The presence of this potential barrier would barricade the relaxation of the electron from WL to the QD energy states.

5.8 **Thermal Quenching in PL**

Further to the hypothesis of a potential barrier between the QD and WL, the carrier dynamics are studied using temperature-dependent PL spectra. It is fundamental to understand the impact of the charged QD to the carrier communication between the QD and the WL. Usually, thermal-coupling between the electronic states of the QD to the WL is prominent in InAs/GaAs QD systems, which permits thermal escape of the electrons in the QD at a very high rate. Subjecting the solar cell in a low temperature

condition suppresses this thermal pathway and reduces thermal escape of the carriers. This keeps the carrier occupied in the QD energy states. As a result, the probability of carrier recombination in the QD increases because the downward transition could occur more efficiently.

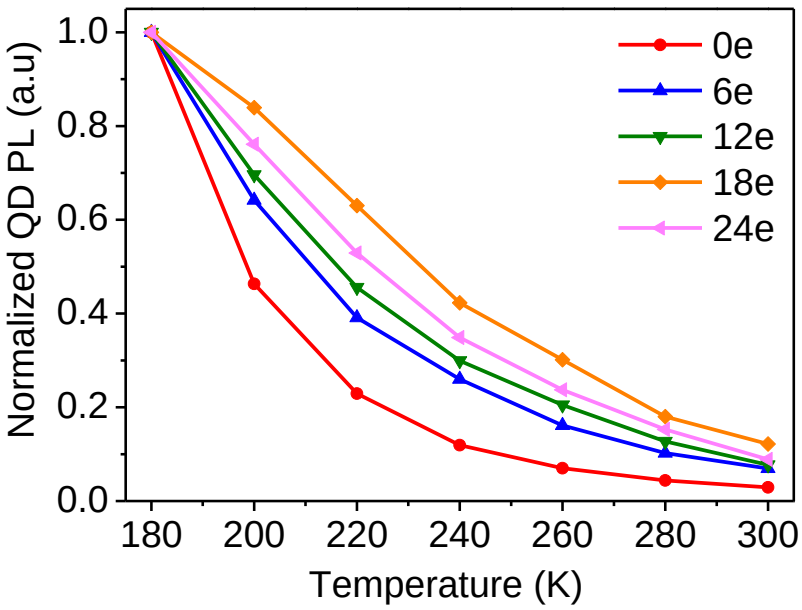

Figure 5.9: Integrated PL intensity plotted as a function of temperature, normalised to show the rate of change in thermal quenching of solar cells with 0e, 6e, 12e, 18e and 24e per dot.

Figure 5.9 plots the integrated PL emission intensity of the GS of the QD over the temperature range of 180 to 300 °C for the QD solar cells. The plot is normalised to show a relative rate of change of the PL emission intensity over the temperature. The relationship between the PL emission intensity over the range of temperatures shows a thermal quenching behaviour. It can be seen that the rate of change of the integrated PL for the QD emission changes with temperature. A stronger thermal-coupling effect usually leads to a higher rate of thermal quenching. As seen in Figure 5.9, the thermal quenching is more rapid in the QD solar cell without Si-doping (0 e/dot) compared to those with Si-doping. A gradual reduction in thermal quenching is seen for the QD solar cells with doping up to 18e/dot, as reflected by the rate of change of the integrated PL intensity over the range of temperatures. This is an indication that the confinement

potential of the QD increases with increasing Si-dopant concentration, which supports the proposal of a potential barrier created between the QD and WL. This observation of thermal quenching by Si-doping is also reported by Kita [150]. For the QD solar cell with 24 e/dot, the thermal quenching does not follow the trend with Si-dopant concentration. This is reasonable as defect states could likely reduce the thermal activation energy.

5.9 **Time-resolved PL**

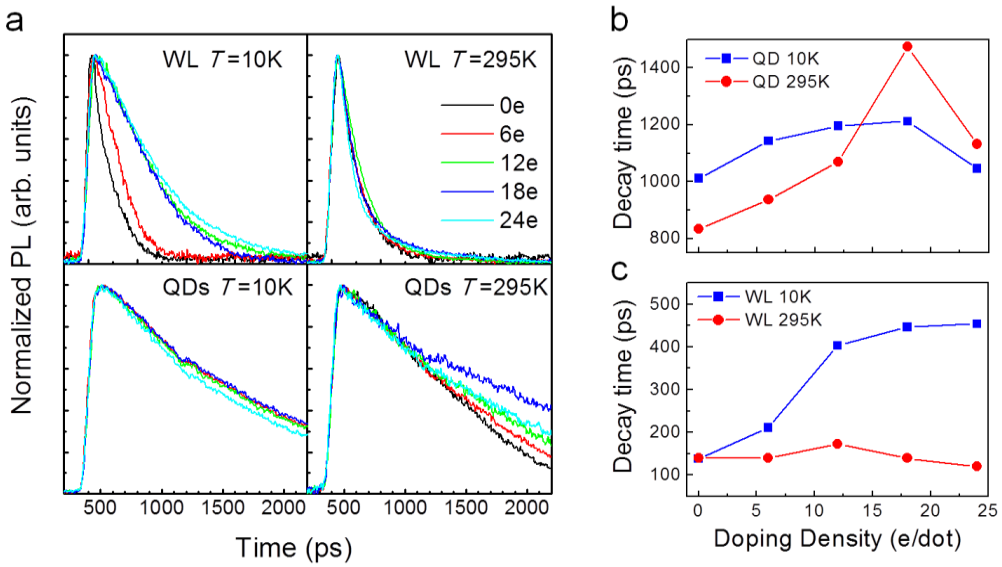

Figure 5.10: (a) A time-resolved PL decay behaviour for QD and WL of different doping concentration at 295K and 10K in with the normalised PL plotted in logarithmic scale. (b) A plot of the QD and WL decay time for QD solar cells with different doping concentration at 295K and 10K.

To understand the effect of the potential barrier on the voltage recovery characteristic in Figure 5.5, time-resolved (TR) PL measurement was provided with the help of Arkansas University [42]. TRPL measurement is facilitated with time-correlated single photon counting and are highly suited to monitor carrier dynamics [151]. The transient PL measurements used 2 ps pulses at excitation of 750 nm from a mode-locked Ti: sapphire laser that produces an optical pulse train at 76 MHz; Hamamatsu

synchroscan streak camera C5680 with an infrared enhanced S1 cathode was used for signal detection. Figure 5.10(a) shows the TRPL results for WL and QD peak emission for all the QD solar cells, measured at room temperature (295K) and cryogenic (10K) conditions. The WL emission of all the QD solar cells measured at 295 K shows no changes in the decay whilst for QD emission at the same temperature the decay only started to show prominent differences in the decay after 1200 ps. This time is longer than the usual radiative and non-radiative decay time. This suggests the observation is based on the doping level, and it rules out the non-radiative processes. Therefore, the possibility of this is likely the supply of carriers from the wetting layers to the QDs. On the other hand, WL emission measured at 10 K shows a clear difference in the carrier lifetime for the different Si-doped QD solar cells. The difference in the decay time indicates a change occurred in the relaxation pathway of the WL. The relaxation pathway for the WL is only available with the link to the QD energy states. Normally, rapid relaxation is expected between the WL continuum to the energy states of the QD, but in the presence of an electrostatic potential barrier the relaxation mechanism is expected to be suppressed. The TRPL result showing a slow decay of the PL emission of the WL supports the hypothesis shown in Figure 5.8.

Figure 5.10(b) shows a plot of the carrier decay time as a function of Si-dopant concentration. The decay time was calculated by fitting the exponential decay formula using the results from Figure 5.10(a). At 10 K, the PL decay time of the QDs is nearly constant for all the QD solar cells with doping. The decay time ranges between ~1.0 ns and 1.2 ns, typical for carriers in an InAs/GaAs QDs. The PL decay time of the WL at 10 K significantly increases with doping density in the QDs. In contrast, PL decay time of the QDs at 295 K increases with Si doping concentration in the QDs while the PL decay time of the WL (~150 ps) remain almost unchanged. The enhanced PL decay time of the WL at high doping concentration confirms a presence of the potential barrier at the WL/QD interface. The potential barrier localises the photon-excited carriers in the QDs for extended time. Therefore, the potential barrier formed between the WL and QD restricts the relaxation of excited carriers into the QD. This potential barrier effectively increases the quantum confinement of the QD, which is supported by the blue-shift of the QD emission seen in the PL results in Figure 5.4 and the QD

absorption spectra seen in the EQE results in Figure 5.7. The stronger quantum confinement could be due to a reduced effect of the WL continuum states, which weakens the thermal-coupling effect and leads to a steady voltage-recovery.

5.10 **Chapter Summary**

The effect of direct Si-doping into the QD of the QD solar cells induces a steady recovery in the V_{OC}. This is explained with the existence of a potential barrier with the evidence derived from the PL, EQE and TRPL measurements. An increase in the PL emission intensity was seen for the QD solar cells when doping concentration increases. This is attributed by the increased quantum confinement of the QD and possibly the inhibition of the defective traps that hosts the NR recombination sites. The blue-shift seen in the QD PL spectra as Si-dopant concentration increases is explained with the state-filling effect where gradual filling of lower energy states in the QD causes transition to occur at higher energy states. This is consistent with the EQE results which shows a blueshift in the absorption QD spectra. The voltage-recovery characteristic from the J-V results deduces that the effect must be linked to the Si-dopants in the QD layer. The Si-dopants deposited on the InAs layer during the growth of the QD will leave n-type dopants in the entire layer which includes the WL. Charged QD with positively charged Si ions distributed in the WL led to the proposal of an electrostatic potential barrier. Temperature-dependent PL studies saw reduced thermal quenching as Si-dopant concentration increases in the QD solar cell. This provided indication to the reduced effect to the thermal pathway for the carriers in the QD which could be due to increased quantum confinement, which supports the proposal of the potential barrier. The TRPL results provided evidence for an increase carrier lifetime in the WL which suggests that the presence of the potential barrier reduces the relaxation of the carrier into the QD. This potential barrier separates the thermal connection between QD energy states and the WL continuum. Hence the thermal-coupling effect is weakened and brought voltage-recovery to the QD solar cell. The reduced thermal-coupling may have helped to push the quasi-Fermi energy level of the CB upwards. Overall, a gradual voltage-recovery from 0.777 V (0e/dot)

to 0.898 V (18e/dot) is achieved, which marks as a ~14% V_{OC} improvement. Although the voltage-recovery was compromised with reduction of current density, the work has provided a technique to tackle the thermal-coupling issue.

Chapter 6

Rapid Thermal Annealing of Quantum Dot Solar Cell

6.1 Introduction

The self-assembled InAs/GaAs QD grown in SK-mode is known as a strain-induced mechanism. The QD formation deteriorates the crystal plane above the QD layer. To compromise this, thick spacer layers can be used to ensure the strain field induced by the QDs do not affect the formation of the subsequent QD layers. Moreover, the combination of lattice-mismatched materials generate defects which degrade the material quality. These inherent defects could be mobile interstitial atoms or point vacancies in the active region, which hosts Non-radiative (NR) recombination events in the semiconductor crystal. Under concentrated illuminations, the NR could generate densely localised carriers known as a microplasma. This effect can become intensified at high temperature which causes damage to the material crystal lattice.

In general, semiconductor devices containing a high density of inherent defects in the crystal material are considered unreliable due to the tendency of fast device degradation during operation. Inherent defects also creates much hindrance to the semiconductor device performance, such as reduction in V_{OC} and J_{SC} in solar cells. It is therefore important to remove host sites of NR recombination in order to improve a

semiconductor solar cell's material quality. This chapter details the effect of rapid thermal annealing (RTA) process on QD solar cell performances. Some results in this chapter are published in the *IET Optoelectronics* conference proceedings titled **"**Effect of rapid thermal annealing on InAs/GaAs quantum dot solar cells" [177]. RTA is a technique that has been extended to post-growth treatment to enhance structural and optical quality of nanostructures via interdiffusion of constituent atoms [152]. This effect has demonstrated improvement in material quality by removing inherent defects from heterostructures [153]. Furthermore, RTA induces atom diffusions in the crystal lattice and the intermixing effect modifies the shape of the nanostructure, making it an alternative technique for changing the interband transition energies of QD [154, 155].

6.2 **Fabrication Details**

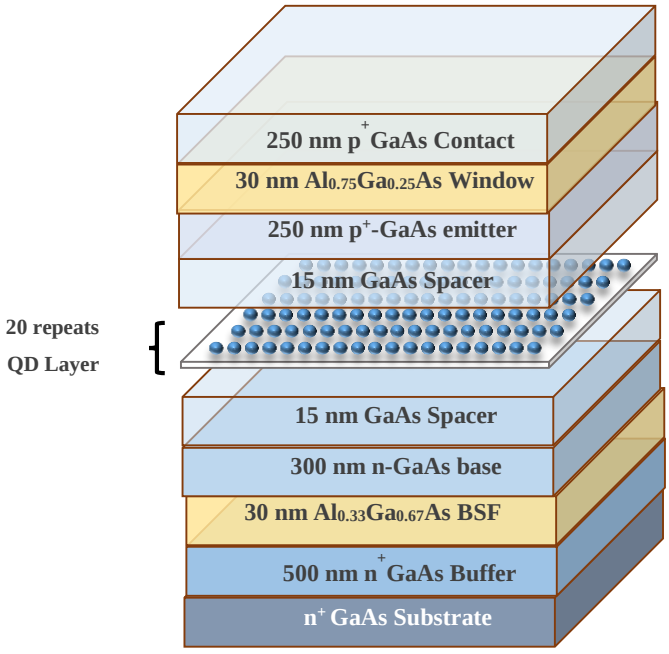

Figure 6.1: Schematic illustration of the quantum dot solar cell structure, grown with 20 repeats of InAs QD layers, each separated by 15 nm of GaAs spacer.

Figure 6.1 shows a schematic illustration of the structural layout of an InAs/GaAs QD solar cell grown on an epi-ready n^+GaAs (100) substrate. The solar cell structure consists of 500 nm n^+GaAs buffer, 30 nm $Al_{0.33}Ga_{0.67}As$ BSF, 300 nm n^+GaAs base,

15 nm undoped GaAs spacer layer, 20 layers of InAs QD each separated by 15 nm of GaAs spacer layer grown at 470 °C recorded from the pyrometer, 250 nm p^{+}GaAs emitter, 30 nm $Al_{0.75}Ga_{0.25}As$ window layer and 250 nm p+GaAs emitter layer. Each spacer layer was grown using high temperature growth spacer layer technique [93]. The QD coverage in each layer was grown with 2.5 ML of InAs.

The grown QD solar cell was cleaved into approximately equal sizes of 5 x 5 mm^2. A 200-nm protective SiO_2 coating was deposited on both sides of the QD solar cell using STS plasma-enhanced chemical vapour deposition (PECVD) followed by RTA treatment using a Solaris 150 RTP System at 650, 700 and 750 °C under N_2 environment. The annealing duration was 30 seconds with a ramp-up rate of 25 °C/sec. It should be mentioned here that such high temperature annealing cannot be performed after the electrode contact deposition because the high annealing temperature could lead to mutual diffusion of atoms between the metal and the semiconductor, causing metal degradation. The SiO_2 coating was removed using a buffered HF bath. Ni-AuGe-Ni-Au contact (5, 50, 25, 200 nm) and AuZn alloy contact (120 nm) were thermally deposited onto the back and front (shadow mask) surfaces, respectively.

6.3 **PL Characterisation**

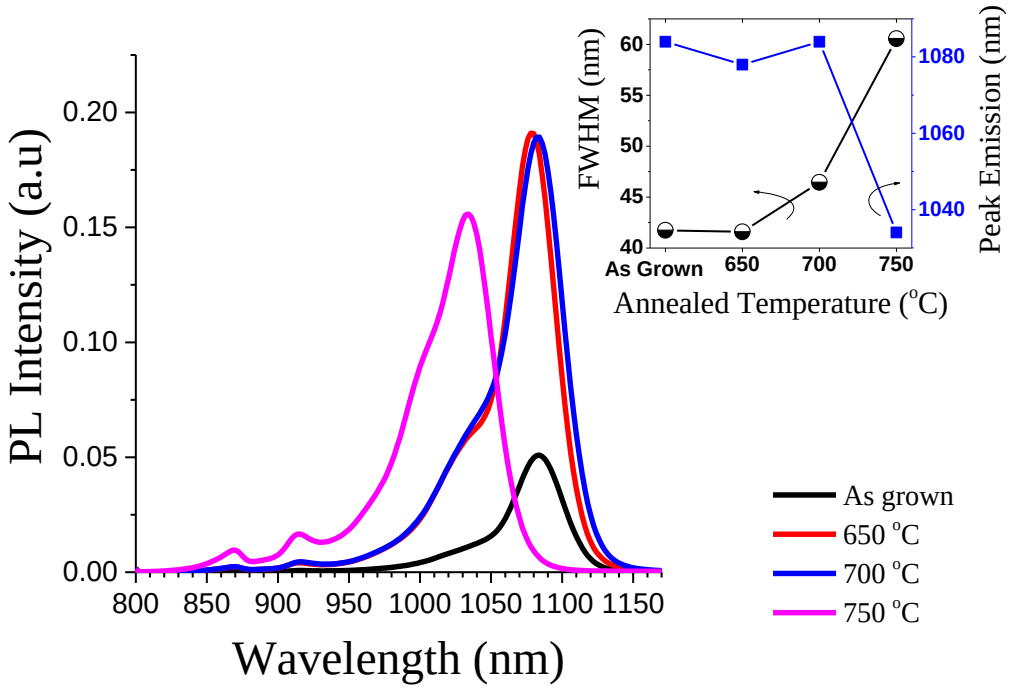

Figure 6.2: Room temperature PL measurement of as-grown, 650, 700 and 750 °C annealed QD solar cells, and an inset showing the full-width half maximum and peak emission plotted against annealed temperature.

Figure 6.2 shows the PL spectra an as-grown QD solar cell and the annealed QD solar cells at 650, 700 and 750 °C. The measurement was carried out at room temperature condition with an excitation power of 18 mW. The as-grown QD solar cell exhibits a QD peak emission wavelength at 1080 nm. The peak at 870 and 920 corresponds to the GaAs material and WL emission, respectively. The QD PL emission intensity dramatically increased after the QD solar cells that underwent the RTA process. At 650 and 700 °C, the QD peak height increased more than 3 times that of the reference QD solar cell. This indicates changes in the optical quality of the QD solar cell related to the material quality. The dramatic increase in the PL emission intensity indicates that a more efficient radiative recombination process took place in the annealed QD solar cells, which signifies better material quality in terms of defect concentration [156]. It is common that the RTP process facilitates the removal of

interior defects from a semiconductor crystal lattice. This helps to suppress the NR recombination pathway [157].

The position of the QD PL peak of the QD solar cell annealed at 650 and 700 °C remains relatively close to that of the as grown QD solar cell, which suggests that the effective bandgap of the QD has not changed, as also the confinement potential. Therefore, the increase in the PL emission intensity is not due to the changes in the QD confinement potential, but a suppression of the NR recombination pathway as a result of reduced density of electron traps which allows a more efficient radiative recombination process. However, at 750 °C, the emission intensity falls below that of 650 and 700 °C with a significant blue-shift. This suggests compositional changes in the QD took place [158–160]. It could be explained by the intermixing effect at higher temperatures. The intermixing induces diffusion and reduces the QD size, therefore enlarges the confinement potential [161].

The inset of Figure 6.2 shows the Full Width Half Maximum (FWHM) and peak energy of the QD solar cell as a function of annealed temperature. At 650 °C and 700 °C, the FWHM is similar to that of the as-grown sample, which indicates that no significant changes to the homogeneity of the QD population. In addition, annealing temperature above 750 °C shows QD peak merging with that of WL at 920 nm, which indicates that the QDs began to disappear after dissolving into the WL. Similar results are reported in Ref [162] and [152].

6.4 **Power dependent PL**

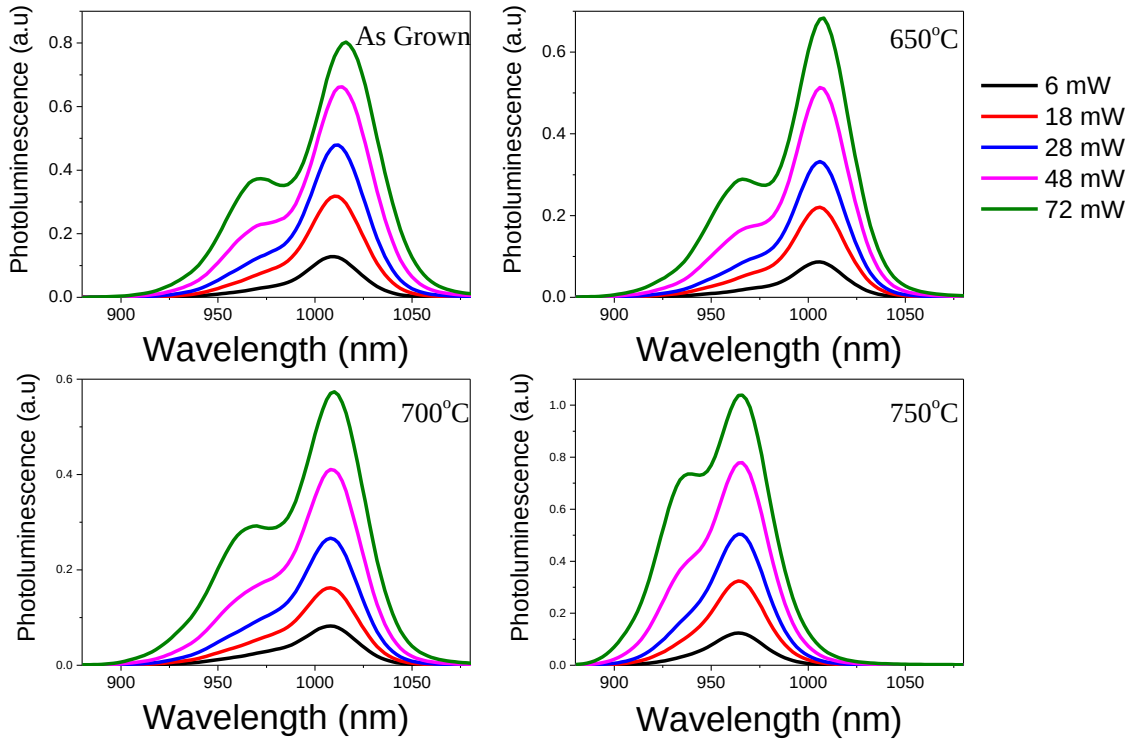

Figure 6.3: Low temperature (10K) power-dependent PL measurement for the as grown QD solar cell and annealed QD solar cell at 650, 700 and 750 °C, with excitation power of 6, 18, 28, 48 and 72 mW.

To confirm the origin of the spectral peaks, the QD solar cell is measured with different power excitations. Figure 6.3 shows a power-dependent PL spectra for as-grown and annealed QD solar cells. The measurement took place under 10 K cryogenic conditions under liquid helium circulation. The PL spectra of the as-grown solar cell shows the lowest energy emission peak at 1010 nm, which represents the GS emission of the QD. This is shifted 80 meV from that measured at room temperature shown in Figure 6.2, which is a result of increased effective bandgap of the QD. Increasing the excitation power increases the PL emission intensity without changing the peak emission position. A peak at ~ 970 nm emerges as the excitation power increases, seen in the PL spectra for the as grown or annealed QD solar cell. This

emerging peak is followed by the saturation of the 1010 nm peak, indicating populated lower energy levels excitation power increases. Therefore, a transition of a higher energy level in the QD dominates. This confirms for the as-grown QD solar cell that the peak at 1020 nm originates from the GS emission whilst the peak at 970 nm originates from the FES. This helps to rule out the possibility of a bimodal QD population in the QD solar cells. In brief, a bimodal QD population is a population of two different QD size distributions. The PL spectra from the as-grown and all the annealed QD solar cells are similar in shape, therefore the possibility of a bimodal QD population is eliminated. At 750 °C, the PL spectra shows the GS and FES emission peak position lies close to each other. This suggests that the high temperature annealing has raised the GS of the QD, effectively reducing the separation of the two energy states.

6.5 **J-V characterisation**

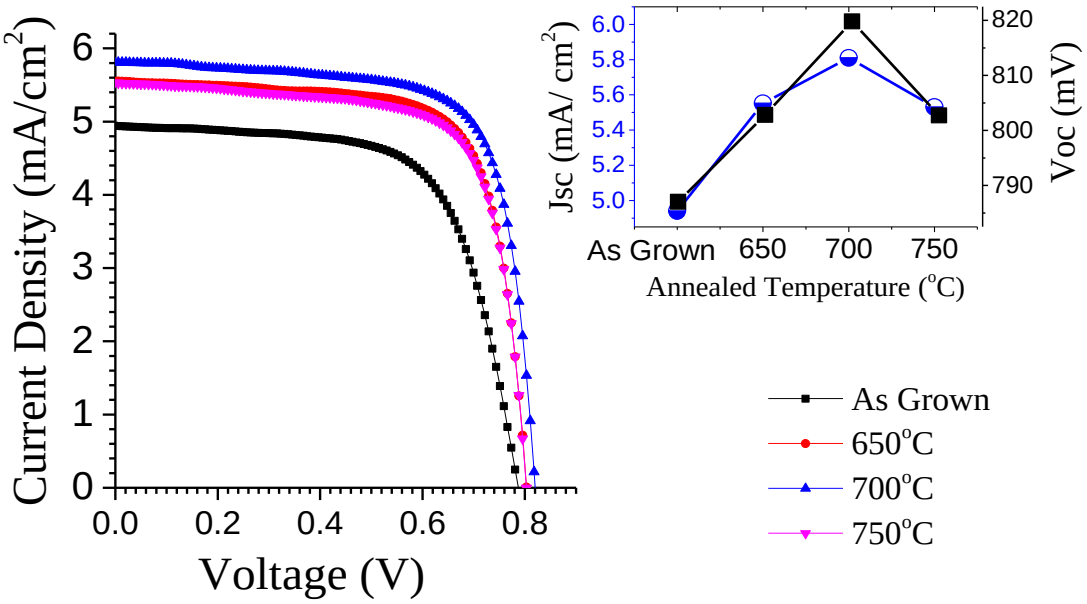

Figure 6.4: J-V curve measured under AM 1.5G (1 sun) condition at 25 °C for the as-grown and annealed QD solar cells, with an inset showing the short-circuit current and the open-circuit voltage plotted against the annealed temperature. .

Figure 6.4 shows the J-V characteristics for the as-grown and annealed QD solar cells measured under 1 sun (AM 1.5 G spectrum) illumination. The as-grown QD solar cell has a J_{SC} and V_{OC} of 4.94 $mAcm^{-2}$ and 787 mV, respectively. The lower J_{SC} recorded here compared with the work in the previous chapters is likely a result of a thicker contact layer (250 nm) in the QD solar cell of this work. The as-grown QD solar cell has a V_{OC} consistent with the value previously reported value [41-42]. Despite this, the improvement in J_{SC} is seen for all the annealed QD solar cells.

The inset of Figure 6.4 shows a plot of the J_{SC} and V_{OC} as a function of annealing temperature. The maximum J_{SC} was reached at 700 °C with 5.81 $mAcm^{-2}$, which marks an 18% increase from that of the reference QD solar cell, and the V_{OC} increased by 30 mV to 0.82 V. This increase in V_{OC} is likely the result from the removal of NR recombination centres, which is supported by the increased PL emission intensity in Figure 6.2. The improvement in both J_{SC} and V_{OC} as a result of thermal annealing suggests that defects are removed from the crystal lattice of the QD solar cell and has led to improvement in material quality.

The removal of defects helps to reduce the impediment to the mobility of the carriers, which extends the carrier diffusion length and increases the probability of carrier extraction. The parameters and efficiency of the solar cells are summarised in Table 3. It can be seen that the FF for the annealed QD solar cells has also improved compared with the as-grown QD solar cell, which may be contributed by the removal of NR recombination centres. However, annealing at 750 °C has shown a poorer solar cell performance as compared to that annealed at 700 °C in terms of J_{SC} and V_{OC}. This may be due to the effect of intermixing. Excessive constituents from the InAs QD and GaAs spacer layer could lead to an exchange of atoms between the InAs QD and GaAs spacer layer at high temperature, which reintroduces vacancy defects. The reduced PL emission intensity at 750 °C supports this view.

RTA Temperature	J_{SC} (mA/cm^2)	V_{OC} (mV)	FF (%)	Efficiency (%)
As Grown	4.94	787	66	2.57
650 °C	5.55	802	72	3.25
700 °C	5.81	819	73	3.48
750 °C	5.53	802	72	3.20

Table 3: Summary of the J_{SC}, V_{OC}, FF and efficiency performances for the as-grown QD and annealed QD solar cell.

6.6 **EQE measurement**

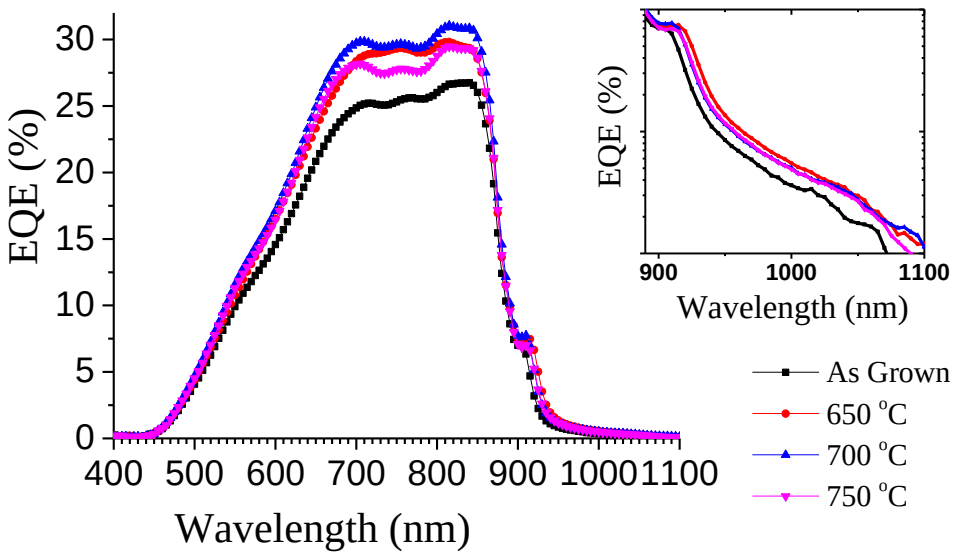

Figure 6.5: EQE measurement for the as grown and annealed QD solar cell at zero-bias at room-temperature conditions, with an inset showing a magnified view of the QD absorption region.

Figure 6.5 shows the EQE spectra for the as-grown and annealed QD solar cells at room temperature. The spectral response in the as-grown QD solar cell shows a sub-bandgap absorption coverage up to ~1100 nm. This is consistent with the PL spectra measured at room temperature as shown in Figure 5.4. The EQE spectra shows a supra-bandgap absorption between 400 – 870 nm which corresponds to the GaAs material. The blue-light absorption (~500) of the QD solar cell in this work is relatively low compared with those in the previous chapters. This is likely due to the parasitic absorption of the thick GaAs contact layer (250 nm) used in the QD solar cells of this work. The thick contact layer would absorb most of the blue light, which doesn't contribute to the solar cell's J_{SC}. Despite this, all the annealed QD solar cells show an improvement in this supra-bandgap absorption region. This suggests that the photocurrent enhancement seen in Figure 6.4 is largely contributed by an improved absorption of the GaAs material in the QD solar cells. The result is consistent with that reported in Ref [159]. The result is explained by the removal of interior point defects from the GaAs region as a result of Ga/In interdiffusion.

At 700 °C, the QD solar cell exhibits the highest spectral response out of the other annealing temperatures, which is consistent with the improved PL emission at 700 °C. However, the spectral response starts to decrease at 750 °C which suggests that the reduction of J_{SC} at 750 °C is also responsible by the GaAs material in the QD solar cell, which signifies that high temperature annealing may reintroduce vacancy or interstitial defects and distributes in the GaAs material of the QD solar cell [163].

The inset of Figure 6.5 shows a magnified view of the QD absorption region. The effect of RTA also improves the spectral response of the QD as compared to the as grown QD solar cell. This suggests that the effect of RTA also facilitates the improvement of the material quality of InAs QD, which helps to increase absorption of sub-bandgap photons.

6.7 **Chapter Summary**

QD solar cells grown in SK mode have inherent defects localised in the InAs QD as well as its surrounding GaAs material. These could be interstitial or vacancy defects acting as NR recombination centres which impedes the flow of intrinsic carriers. As a result, the carrier mobility and extraction probability is impacted due to the presence of electron traps. By using the RTA post growth technique at 650, 700 and 750 °C on the QD solar cells, Ga/In interdiffusion in the crystal lattice of the InAs/GaAs material system induces molecular rearrangement in the crystal lattice of the material, which removes some defects and effectively removes the electron traps. This helps to suppress the NR recombination pathway and allows more efficient radiative recombination process to take place. This is evidenced by the increased PL emission intensity after the QD solar cell underwent RTA.

The suppression of NR recombination has helped to improve the QD solar cell performance in terms of J_{SC} and V_{OC}. As a result, an overall improvement in the conversion efficiency is seen. The RTA temperature that delivers the best J-V performance of the QD solar cells was found to be 700 °C. This has achieved an improvement of J_{SC} from 4.94 to 5.81 $mAcm^{-2}$ and V_{OC} from 787 to 819 mV, which marks an 18% and 4% improvement in J_{SC} and V_{OC}, respectively. On the other hand, a QD solar cell annealed at temperature above 750 °C has a reduced QD PL emission peak. This is no surprise because above this temperature the QD will begin to dissolve into the WL forming a QW equivalent structure and have lost the properties of QD, including 3D confinement. Hence, there is an upper limit to the annealing temperature for QD solar cells. The thermal treatment must be kept below 750 °C to sustain the requirement for establishing IBSC. It has been shown by other report that intermixing upon RTA processing has facilitated tuning to the desired spectral response [155], [158]. In this study, substantial tuning is initiated when the annealing temperature is above 700 °C.

Chapter 7

InAs/InGaP QD solar cells with an AlGaAs interlayer

7.1 Introduction

One of the ways to separate the IB from the CB in a QD solar cell is to raise the bandgap offset, the difference between the CB of the QD material and the CB of the host material. This can be achieved by embedding the InAs-QDs within a large bandgap host material. It would lead to enhanced quantum confinement for the carriers within the QD GS, therefore minimises the thermal escape of carriers. In principle, this could allow the QD-IBSC to preserve the V_{OC} of the host material [31]. Nonetheless, IBSC operation requires a suitable material system to maintain three separate quasi-Fermi levels [135-136]. Since IB is formed by introducing confined discrete energy states from the QD within the band gap of the host material, changes to the material type of the QD and the barrier will naturally modify the bandgap. For this reason, the work of exploring different material combinations has been extensively studied and the search for the optimal performing material system for IBSC is still ongoing.

The highest theoretical efficiency for IBSCs requires a high bandgap of 1.93 eV. This can be achieved using AlGaAs or InGaP materials. On the other hand, the sub-

bandgaps required are 0.7 eV and 1.2 eV [19]. The success of achieving this would depend on the position of the IB. Conventional InAs/GaAs QD system is not an ideal candidate for IBSCs because the GaAs bandgap is about 500 meV lower than the ideal IBSC [54, 122,164,165]. In the past, QDs embedded in high bandgap materials have been studied, such as InAlGaAs, AlAs and AlGaAs which have shown empirical achievements [31], [122], [87]. These works have shown increased confinement potential and reduced thermal activation energy. It has been demonstrated that a built-in potential barrier between the QDs and WL can be formed by directly dope the QDs with Si, resulting in the thermal decoupling of the IB and CB for QD solar cells [37], [42], [142], which has been discussed in chapter 5. This approach has proven to be a promising solution to resolve the long-term thermionic emission issues of QD-IBSCs. Recently, the efficient two-step photon absorption has been theoretically predicted by inserting closely stacked InAs QDs into a high-bandgap InGaP matrix [166]. In addition, this material system is well known for its strong phonon bottleneck effect at low temperature due to the large confinement for carriers [167]. It has been shown that $In_{0.4}Ga_{0.6}As$/GaAs QDs grown in InGaP matrix have larger energy separation between the QD GS and the CB in comparison to conventional InAs/GaAs QDs [168]. More recently, prototype InAs/InGaP QD-IBSCs were fabricated with enlarged intersubband energy over 400 meV [169]. So far, the InAs/InGaP QD system gives an encouraging outlook to the IBSC concept, and deserves further experimental research.

This chapter details on the growth study of InAs-QDs grown on the surface of InGaP buffer layers as a function of InAs coverage and growth temperature. The evolution of QDs was examined by AFM and PL measurements. High-quality InAs QDs directly on the InGaP layer were hindered by a destructive surface exchange reaction between InAs and InGaP. To solve this problem, an AlGaAs interlayer was used to separate the InAs QDs from InGaP. This approach yielded high-density QDs without observing any defective clusters by AFM measurements. Furthermore, low-temperature power-dependent PL results showed that the bandgap configuration of this InAs/AlGaAs/InGaP QD system closely matches that of an ideal IBSC. A QD solar cell with 20 layers of InAs/InGaP QDs with AlGaAs interlayers was thus

fabricated. This was followed by a post-growth RTA process to further improve the material and device quality. Some results in this chapter are published in the journal of *Solar Energy Material and Solar Cells* titled **"**InAs/InGaP quantum dot solar cells with an AlGaAs interlayer" [43].

7.2 Growth study of InAs-QD/InGaP Heterostructure

All samples were grown in the MBE system on epi-ready p+-GaAs (100) substrates. The growth of InAs QDs on the $In_{0.49}Ga_{0.51}P$ buffer layer lattice-matched to GaAs substrates was studied by varying the InAs nominal thickness from 0.3 to 2.1 ML and the growth temperature from 480 to 510 °C. Each sample consists of two layers, one layer is formed with InAs-QDs embedded into the InGaP buffer and another layer was grown directly on top without capping. Surface morphology studies were performed on these uncapped samples by using AFM imaging. The PL spectra were measured at room temperature with 6 mW excitation power.

7.2.1 The Effect of InAs Coverage on InGaP

Figure 7.1 (a)-(d) shows 1×1 μm^2 AFM images of samples with InAs deposited directly on the $In_{0.49}Ga_{0.51}P$ layer at 495 °C. Large (>50 nm diameter) clusters can be seen along with irregular sized QDs after depositing 0.3-ML InAs. The QDs are very unlikely formed via the SK mode because the deposition is significantly lower than the critical thickness of ~1.5 ML, which is generally required for initializing the SK-type InAs/GaAs QD. In general, the large clusters with irregular shapes are defective [170-172]. The formation of defective clusters can be explained by the aggregation of QDs. The tendency for out-diffusion of In atoms from the InGaP buffer layer has interfered with the QD growth [38, 173, 174]. It can be seen that even with InAs coverage as low as 0.3 ML could form QDs and other dot-like particles. This indicates the additional supply of In atoms has took part in the growth process. Since the QD sizes exhibits a very large variance, it is very likely that the diffusion mechanism for In atoms from the InGaP buffer layer is random. The densities of coherent dots and defective clusters as a function of InAs coverage are plotted in Figure 7.1(e). The

highest QD density of 4.6 × 10^{10} cm^{-2} was observed at 0.5 ML of InAs coverage. Further increase in InAs coverage led to a rapid reduction in coherent QD density and an increase in defective dot density. The maximum defect density of 9 × 10^{8} cm^{-2} was found at 1.3 ML of InAs coverage. This suggests that the defective dot density cannot be suppressed by increasing the InAs coverage and the out diffusion of In atoms could severely penetrate the upper layer.

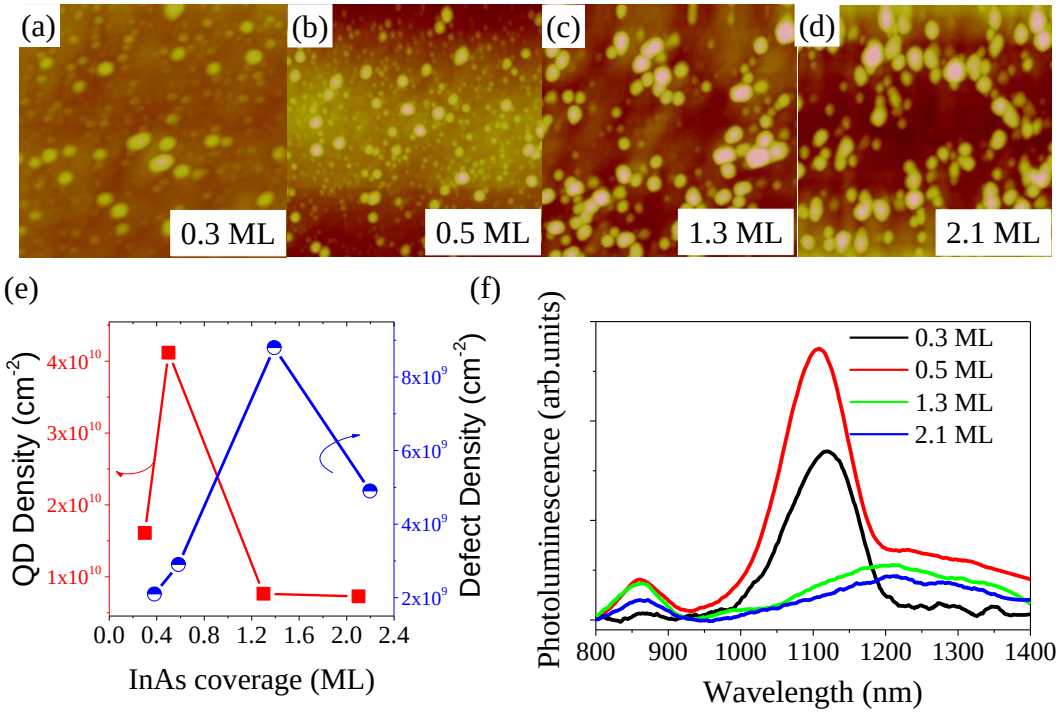

Figure 7.1: AFM images (1×1 µm2) of InAs QDs grown on the InGaP surfaces at 495 °C with (a) 0.3 ML, (b) 0.5 ML, (c) 1.3 ML and (d) 2.1 ML of InAs coverage. A plot of densities of coherent dots and defective clusters as a function of InAs coverage is displayed in (e). The corresponding room-temperature PL spectra are shown in (f).

Figure 7.1(f) shows the room-temperature PL spectra of these samples using an excitation power of 6 mW. The PL emission peaks at ~1100 nm, which confirms the presence of QDs for all these samples. The peak at 870 nm corresponds to the emission of GaAs substrate but the InGaP buffer emission, which is expected to have a peak <800 nm, is not seen in this spectral coverage. At 0.5 ML InAs coverage the PL emission intensity is the highest compared with the other spectra. Increasing the InAs

coverage dramatically reduced the PL emission intensity. This indicates that the material quality of the InAs/InGaP QD became poor, which could be due to the increased NR recombination related to the defective clusters observed in the AFM images. The emission at ~1100 nm has also gradually red-shifted which indicates an increase of the average size of the QDs in the population as InAs coverage increases. Furthermore, the WL emission which is normally seen at ~920 nm for InAs/GaAs QDs is absent from the spectra, which rules out the possibility of the QD being grown via the SK-mode.

7.2.2 The Effect of Growth Temperature on InAs-QD/InGaP surface

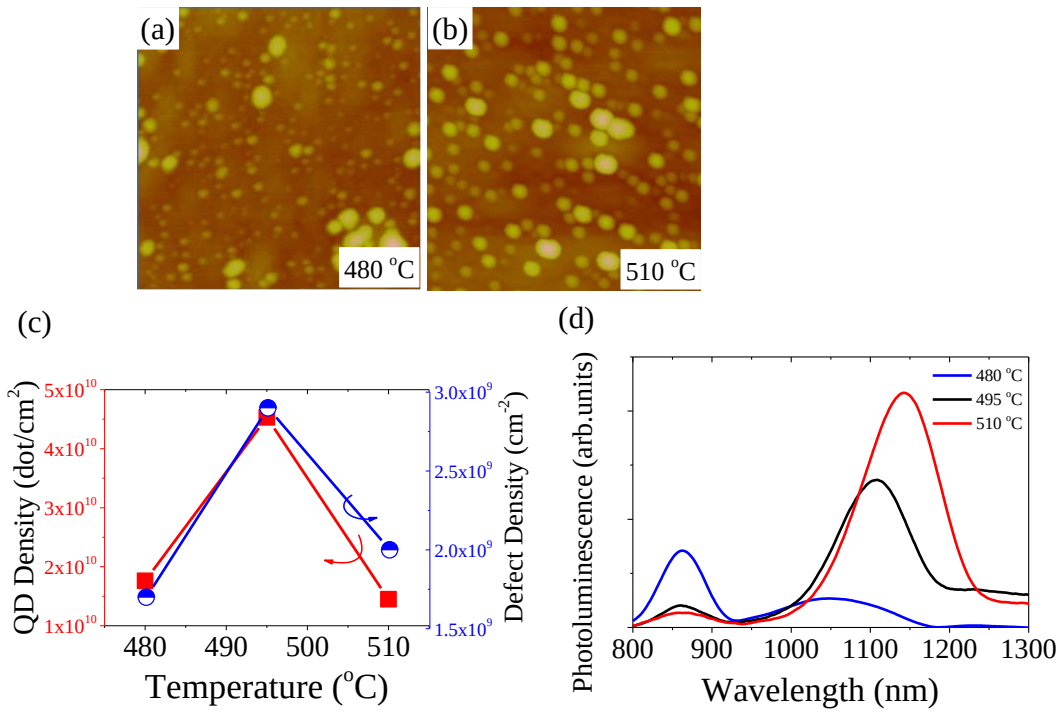

Figure 7.2: AFM images (1×1 μm²) of 0.5 ML of InAs QDs grown on the InGaP buffer layer at different temperatures (a) 480 °C and (b) 510 °C. The density of QDs and defective clusters as a function of temperature is plotted in (c). The corresponding room-temperature photoluminescence measurement is shown in (d).

The influence of growth temperature on InAs/InGaP QD morphology was further investigated at 480 and 510 °C. The 1×1 μm² AFM images of samples with 0.5 ML of

InAs deposited on the InGaP buffer layer at 480 and 510 °C are shown in Figure 7.2(a) and (b), respectively. Not only raising the temperature did not help with the epitaxial growth of a uniform InAs-QD layer, the size of the particles has increased at higher growth temperatures, which indicates an increased surface exchange reaction took place. This is supported by the increase in QD average diameter from 21.9 ± 4.0 nm at 480 °C to 41.0 ± 10.2 nm at 510 °C. This is nearly double the QD diameter which indicates that further increase in growth temperature could lead to greater severity in terms of surface In diffusion interference. At 510 °C, the surface of the sample has particles as large as ~100 nm in diameter. It is worth mentioning that at 495 °C, the particles evolve into bimodal QDs with average diameters of 23.2 ± 4.6 nm and 41.7 ± 7.5 nm for small and large dots, respectively. The small QDs are believed to be coherent dots while the large ones are aggregated clusters. Due to the presence of large dots, the average height is as large as 8.6 ± 3.6nm.

Figure 7.2(c) shows a plot of coherent dot and defective cluster densities as a function of temperature, with the inclusion of AFM results from the sample shown in Figure 7.1(b). The growth temperature that yielded the highest QD density as well as defective dot density was 495 °C. It can be seen that a dramatic reduction of the densities of both coherent dots and defective clusters occurs above 495 °C. Since the In atoms within the InGaP buffer could act as an additional In source for the QD nucleation process [38], increasing the growth temperature could promote the out diffusion of In atoms from the InGaP layer, and hence increases the dot size.

Figure 7.2(d) shows the room temperature PL spectra. The QD peak emission shows a redshift with increasing growth temperature from 480 to 510 °C. This confirms that the overall QD sizes increase with increasing temperature. These results show that non-uniform InAs QDs with larger defective clusters are formed on the InGaP buffer layer across the temperature range of 480-510 °C and the InAs coverage range of 0.3-2.1 ML. This is likely a result of the destructive effect of In atoms from the InGaP buffer and As-P exchange occurring at the InAs/InGaP interface [173].

7.2.3 Growth of InAs/InGaP-QD using AlGaAs interlayer

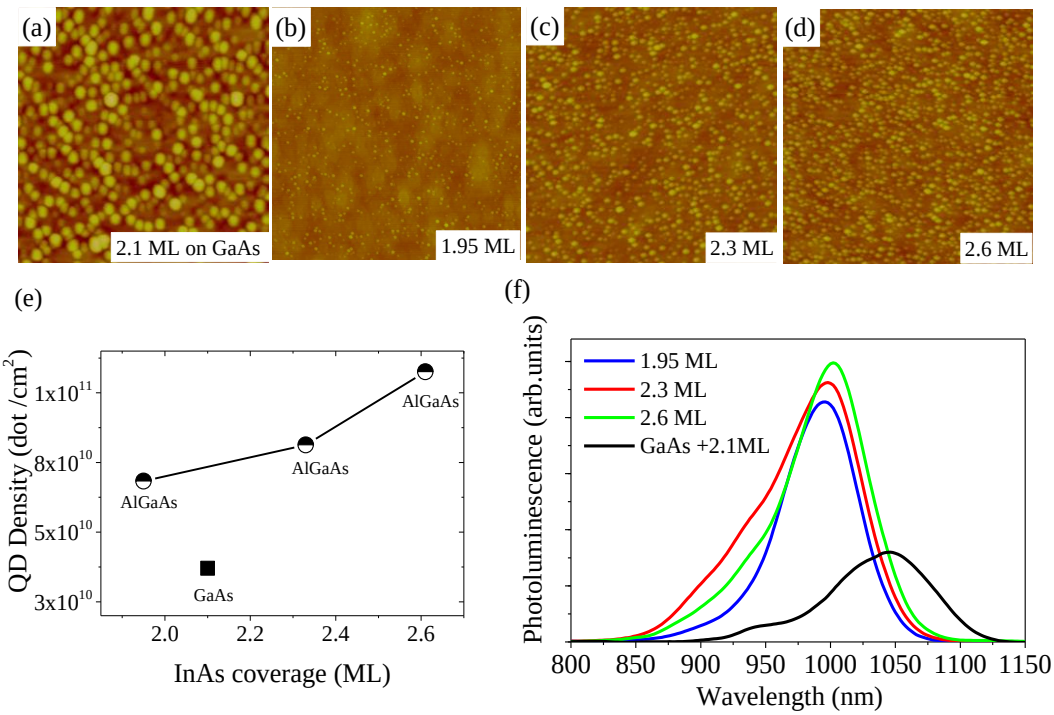

Figure 7.3: AFM images (1×1 µm2) of InAs QDs grown on (a) GaAs and (b), (c) and (d) on AlGaAs with the InAs coverage labelled. QD density vs. InAs ML coverage is plotted in (e). The room-temperature photoluminescence is shown in (f).

To avoid In diffusion and As-P exchange between the InAs QDs and the InGaP buffer, an $Al_{0.33}Ga_{0.67}As$ interlayer was introduced between the InGaP buffer layer and InAs QDs in this work. The $Al_{0.33}Ga_{0.67}As$ material was chosen for its similarity to the bandgap properties of InGaP, because the interlayer must retain the high CB offset between InAs QDs and the confining layers [87] for the purpose of this study. AlGaAs materials can have a bandgap as high as 2.16 eV (pure AlAs), much higher than the GaAs material (1.42 eV). Within the InGaP matrix, InAs QDs were grown on 3-nm $Al_{0.33}Ga_{0.67}As$ and capped by 6-nm $Al_{0.33}Ga_{0.67}As$. All the samples were grown at a fixed temperature of 495 °C. The AFM measurements were performed on the uncapped QD samples. Figure 3(a) shows a 1×1 μm^2 AFM image of 2.1-ML InAs coverage on a GaAs interlayer as a reference. Figure 7.3(b)-(d) show InAs QDs grown on AlGaAs with InAs coverage of 1.95, 2.3, and 2.6 ML, respectively. No large

defective clusters were observed on these AFM images. The average size of QDs formed directly on GaAs surface is 34.8±8.7 nm in diameter and 5.2 ±1.3 nm in height. After the AlGaAs interlayer was deposited, the average lateral size of QDs reduces to 10.2 ± 1.4 nm, 14.9 ± 3.7 nm, and 16.5 ± 1.8 nm while the height of QDs is 5.2±1.0 nm, 9.4±1.9 nm and 7.7±1.9 nm for InAs coverage of 1.95, 2.3, and 2.6 ML, respectively. The reduced average size of the QDs grown on the AlGaAs surface is caused by the decreased adatom diffusion length on the AlGaAs compared to that on the GaAs surface. The corresponding QD density as a function of InAs coverage is plotted in Figure 7.3(e), where the InAs QDs grown on GaAs interlayer is indicated by a black square. The maximum density of InAs QDs on AlGaAs is ~1×10^{11} cm^{-2} for the sample with 2.6-ML InAs coverage. This is similar to a previously reported density of InAs QDs grown on AlGaAs buffer layers [174].

Figure 7.3 (f) shows the room-temperature PL results for those samples with GaAs and AlGaAs interlayers. An improvement in QD emission intensity was observed with increasing InAs coverage, which correlates well with the QD density shown in Figure 7.3(e). QDs grown on AlGaAs exhibit a blueshift and higher PL emission compared to QDs grown on the GaAs. Although this could be attributed to the smaller size and higher density of QDs on the AlGaAs surface, as observed from the AFM images, a raised confinement potential from the AlGaAs interlayer for InAs QDs cannot be ruled out [87].

7.3 **Growth and Fabrication of Solar Cells**

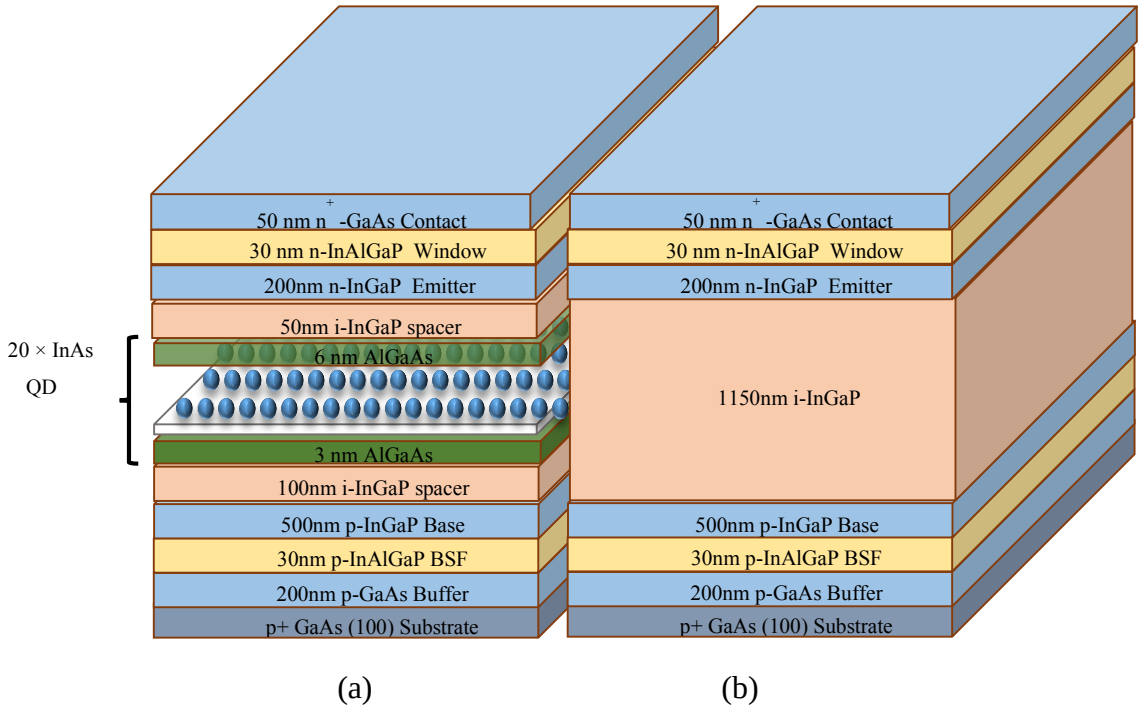

Figure 7.4: Schematic illustration of the (a) InAs/InGaP QD solar cell grown on a p-type GaAs substrate with the undoped region consists of InAs QDs grown on 3-nm AlGaAs, capped by 6-nm AlGaAs, and sandwiched by the InGaP spacer layer, and (b) an InGaP reference solar cell with similar structure except the i-region is replaced with 1150 nm of InGaP bulk material.

Based on the results obtained for the InAs/AlGaAs/InGaP QD structures described above, an InAs/InGaP QD solar cell was grown on epi-ready p+-GaAs (100) substrates. An InGaP solar cell was also fabricated as reference sample, and consists of a 200 nm p-GaAs buffer layer, 30 nm p-InAlGaP BSF layer, 500 nm p-$In_{0.49}Ga_{0.51}P$ base, 1150 nm undoped $In_{0.49}Ga_{0.51}P$ bulk material, 250 nm n-$In_{0.49}Ga_{0.51}P$ emitter, 30 nm n-InAlGaP window, and 50 nm n+-GaAs contact layer. The InAs/InGaP-QD solar cell has the same structure as the InGaP reference solar cell except that 20 repeats of InAs/AlGaAs QD layers were inserted within the intrinsic region instead of InGaP bulk. Each QD layer consists of 2.6-ML InAs grown on 3-nm $Al_{0.33}Ga_{0.67}As$ and capped by 6-nm $Al_{0.33}Ga_{0.67}As$, and is separated by a 50 nm $In_{0.49}Ga_{0.51}P$ spacer layer.

Figure 7.4(a) shows the schematic illustration of the QD Solar Cell and Figure 7.4(b) shows an InGaP reference solar cell. It should be mentioned here that, due to the low temperature growth, AlGaAs layers suffer from the sensitivity to oxygen incorporation, which can degrade the device performance. Therefore post-growth thermal treatment was studied to improve QD solar cell performance. A 200-nm SiO_2 coating was deposited on the QD solar cell using STS plasma-enhanced chemical vapour deposition (PECVD) followed by RTA treatment using a Solaris 150 RTP System at 650, 700, 750 and 800 °C under N_2 environment. The annealing duration was 30 seconds and the ramp-up rate was 25 °C/sec. The SiO_2 coating was removed using a buffered HF bath. The solar cell devices were fabricated for the as-grown and annealed samples. Contact electrodes consisting of Ni-AuGe-Ni-Au (5, 50, 25, 200 nm) and Zn-Au alloy (200 nm) were thermally evaporated onto the front and back of the samples, respectively. No anti-reflective coating was used for these solar cell devices.

7.4 **PL Characterisation**

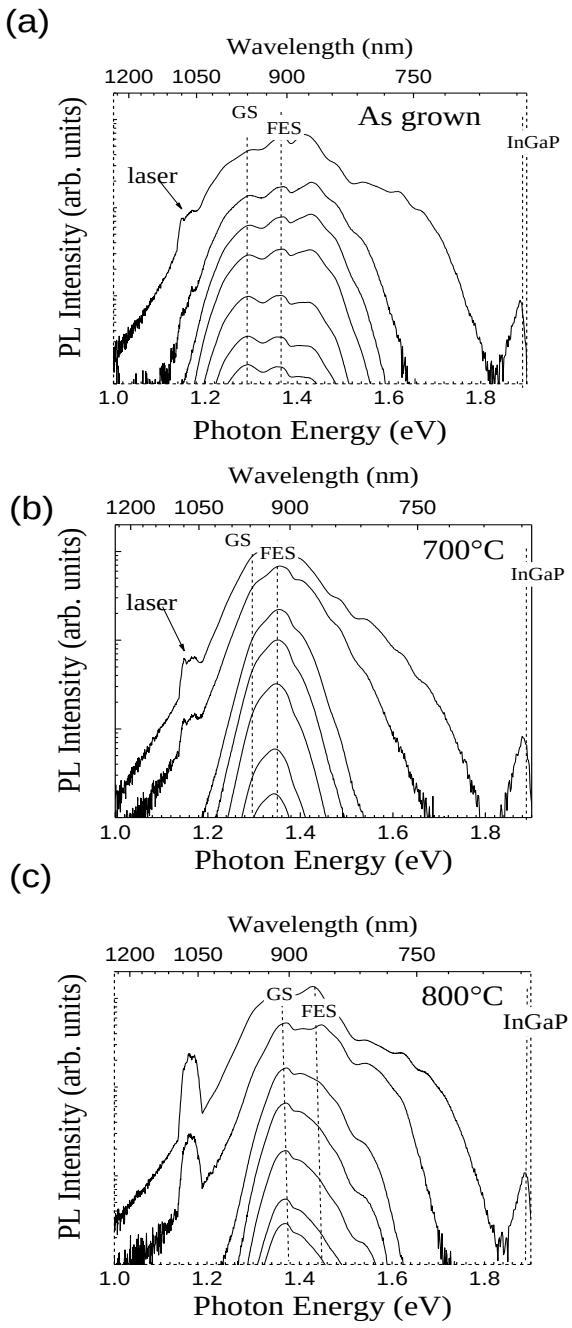

Figure 7.5: Low temperature (10 K) power-dependent photoluminescence spectra for (a) an as-grown QD solar cell and QD solar cells annealed at (b) 700 °C and (c) 800 °C with the excitation power from 0.1 to 1000 W/cm^2. The laser, ground state (GS), first excited state (FES) and InGaP material emission are labelled.

Figure 7.5 shows a power-dependent PL measurement at 10 K for (a) an as-grown QD solar cell, (b) a QD solar cell annealed at 700 °C, and (c) a QD solar cell annealed at 800 °C. The InGaP peak emission is found at ~1.88 eV (~1.76 eV at 300 K), which is close to the aforementioned optimal IBSC bandgap of 1.93 eV. Although the peak emission for the AlGaAs interlayer cannot be distinguished here, it is expected to be ~1.83 eV at 10 K, and hence overlaps with that of the InGaP peak. The emission energies of the QD GS and the FES are 1.29 eV (~1.24 eV at 300 K) and 1.37 eV (~1.28 eV at 300 K), respectively for the as-grown sample. This is illustrated schematically in the bandgap diagram in Figure 7.6. Annealing at 700 °C causes the GS to blueshift to 1.30 eV with an increased PL intensity [111, 157, 161, 175, 176]. The PL spectra further blueshift to 1.35 eV (1.3 eV at 300 K) with annealing temperature of 800 °C. The blueshift of PL emission can be explained by a reduced QD size and/or the change of QD material composition, while the increased emission intensity is related to the removal of NR recombination centres [161, 176, 177]. After annealing the InAs/InGaP QD solar cells at 700 and 800 °C, the GS emission of InAs QDs remains close to the first photon-absorption bandgap at 1.24 eV proposed for IBSCs. Conventional InAs/GaAs QDs generally experience morphological evolution from QDs to QWs for post-growth annealing temperature up to 800 °C. However, for the InAs/InGaP-QD solar cell sample annealed at 800 °C, the relatively small energy shift and the large energy separation between the GS and InGaP matrix indicate that the QDs remain even after the elevated annealing temperature. The rather broadband PL emission of the QD solar cell annealed at 800 °C also confirms the presence of QDs.

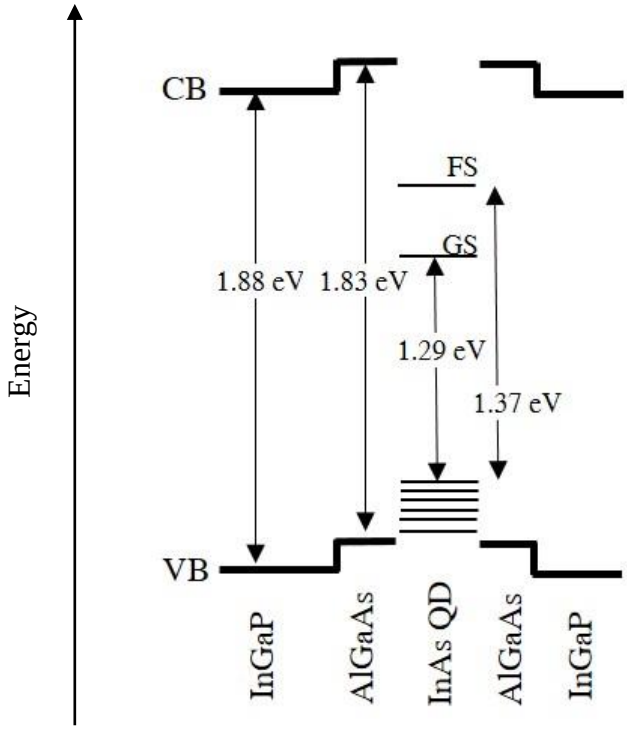

Figure 7.6: A simple bandgap diagram representing the bandgap configuration of the as-grown InAs/AlGaAs/InGaP QD solar cell structure.

7.5 **EQE Measurement**

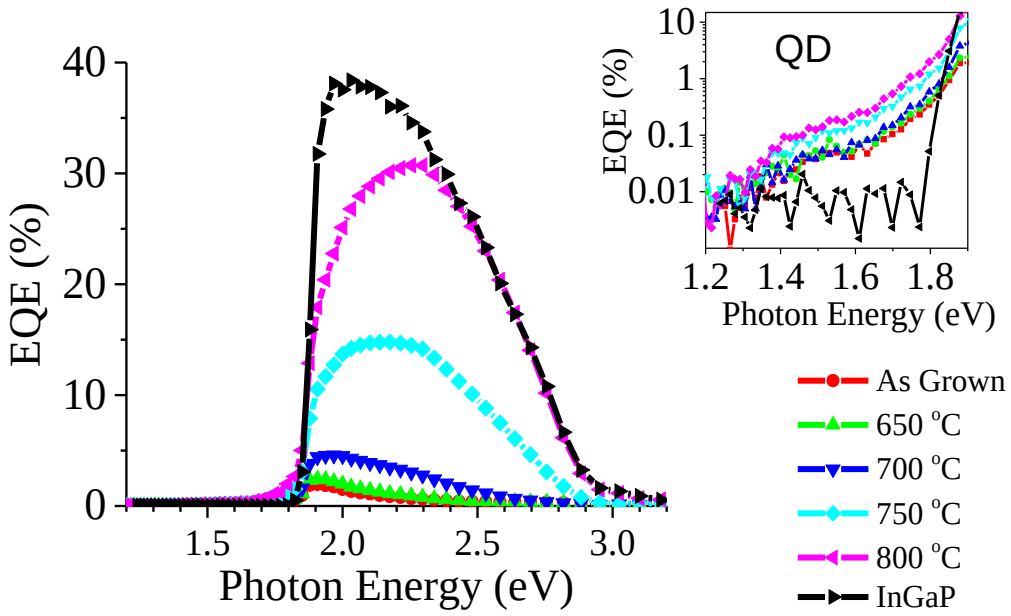

Figure 7.7: Linear external quantum efficiency measurements of the annealed QD solar cells. The inset displays the semi-log spectral response corresponding to the QD region.

Figure 7.7 shows the EQE spectra of the as-grown and annealed InAs/InGaP-QD solar cells and an InGaP reference solar cell, plotted against the photon energy (eV) and measured at room temperature and zero-bias. A gradual increase in spectral response between 1.8 and 3.0 eV, which corresponds to absorption in the InGaP and AlGaAs materials, is observed for QD solar cells with increasing annealing temperature. The supra-bandgap absorption at around red-light region of 2.0 eV shows the dominating improvement in spectral strength. This indicates an improvement in the material quality of the i-region and the base region. This improvement could be due to the removal of point defects or interstitial defects from the AlGaAs and/or InGaP spacer layer, which is consistent with the effect of RTP process on InAs/GaAs QD solar cell shown in chapter 6. The QD region also shows a gradual enhancement in spectral response, as shown in the inset of Figure 7.7. The improvement in material quality owing to RTA has previously been reported for QD materials and devices [177-179].

7.6 **J-V Characteristics**

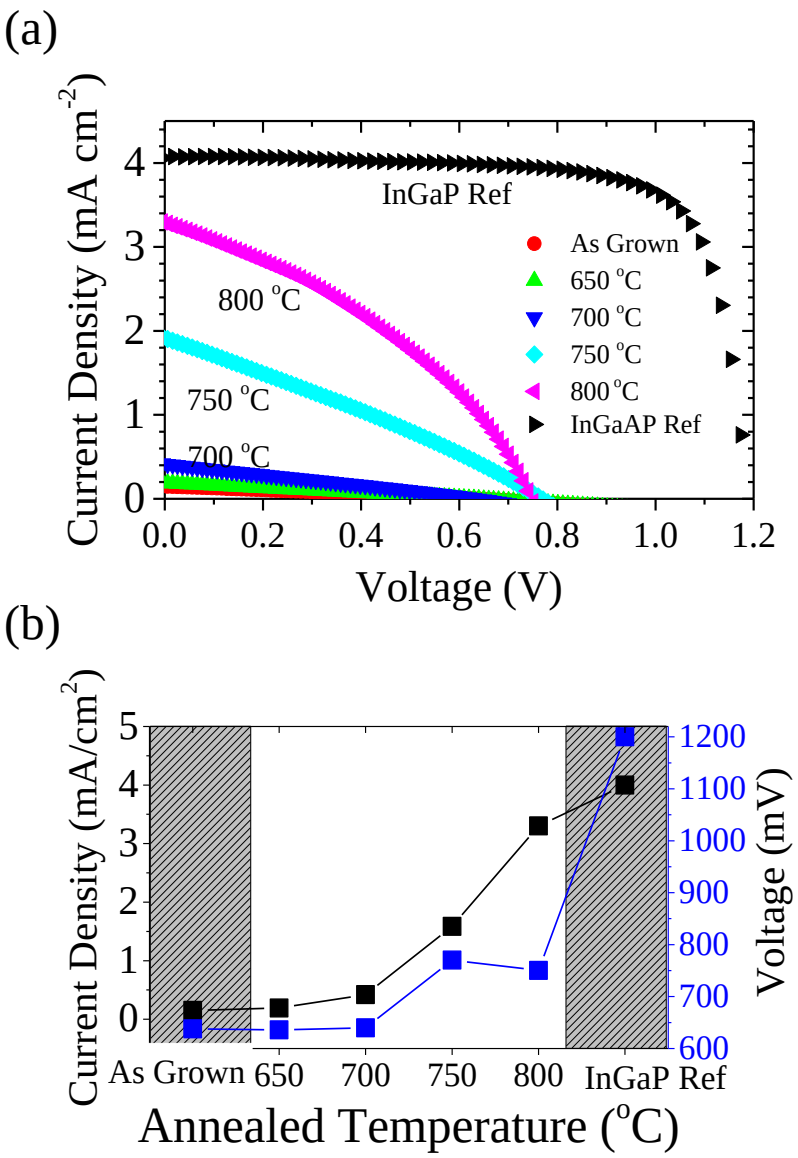

Figure 7.8: (a) Current density-voltage characteristics of InAs/AlGaAs/InGaP QD solar cells with the reference InGaP solar cell and (b) a plot of current density and open-circuit voltage of the QD solar cells as a function of the annealed temperature.

Figure 7.8(a) shows J-V measurements for the solar cells under 1 sun AM 1.5 illumination. Figure 7.8(b) shows a plot of J_{SC} and V_{OC} as a function of annealing temperature. The QD solar cell without RTA treatment exhibits diminished device

performance with a J_{SC} output below 0.5 mA/cm^2 and a V_{OC} just over 0.7 V. This is far below the performance of the reference InGaP solar cell. The poor performance is primarily attributed to the poor material quality of AlGaAs layers grown at a lower temperature. The high-quality AlGaAs MBE layers can only be obtained when the growth temperature is about 700 °C [180]. This would lead to the QD solar cell suffering from severe impediment to the carrier extraction mechanism. In addition, the recombination current through the defects can act as a shunt and degrade the device performance, which is in agreement with the poor fill factors shown in Figure 7.8(a). With increasing annealing temperature, the steady recoveries of both current density and voltage towards those of the reference InGaP solar cell have been observed. The improved J_{SC} output corresponds well with the enhancement in spectral response from the EQE results. A gradual improvement in ideality factor upon annealing can also be observed as a result of reduced recombination and improved carrier collection.

7.7 **Chapter summary**

A growth study was conducted on growing InAs QDs directly on the InGaP surface. Due to the surface exchange reaction, where In out-diffusion from the InGaP material interferes with the InAs QD growth and created large defective cluster, a high quality coherent QD cannot be realised. Despite attempts on changing the InAs coverage and growth temperature, what was needed is an interlayer which could effectively suppress the exchange reaction between the InAs and the InGaP. Hence, an AlGaAs was inserted between the two materials, which resulted in high quality and high density QD arrays. QD solar cells with the QD layers consisting of the InAs/AlGaAs/InGaP configuration was grown and processed by RTP. The optimal QD solar cell performance was obtained at an annealing temperature of 800 °C with a J_{SC} of 3.2 mAcm^{-2} and a V_{OC} equal to 0.75 V. With RTP process, a gradual increase in spectral response between 1.8 and 3.0 eV was recorded for the QD solar cells, which corresponds to absorption in the InGaP and AlGaAs materials. At the same time, the QD region also shows a gradual enhancement in spectral response. With increasing annealing temperature, the steady recoveries of both J_{SC} and V_{OC} towards those of the

reference InGaP solar cell have been observed. The improved J_{SC} output corresponds well with the enhancement in spectral response from the EQE results. Post-growth annealing was clearly effective on improving the device performance, optimization of the low temperature AlGaAs layers would play a key role in improving the solar cell efficiency in the future.

The study of the QD solar cell bandgap was carried out using PL emission measurement. The InGaP peak emission was found at ~1.88 eV (~1.76 eV at 300 K), which is close to the aforementioned optimal IBSC bandgap of 1.93 eV. The emission energies of the QD GS and the FES are 1.29 eV (~1.24 eV at 300 K) and 1.37 eV (~1.28 eV at 300 K), respectively for the as-grown sample. This is also close to the ideal sub-bandgap energy of 1.2 eV for the first photon absorption process in IBSC.

Chapter 8

Conclusions and Future Work

8.1 **Conclusions**

InGaAs/GaAs Quantum Well (QW) and InGaAs/GaAs SML-QD solar cells were grown. Comparison studies using AFM imaging techniques shows undulation from a crosshatch pattern on the surface of QW and SML-QD solar cells which is related to defects in their crystal lattice. The reduced NR-recombination process in SML-QD solar cell structure compared with the QW solar cell is an attractive feature for IBSC. The study provides a good approach of reducing defect density by optimisation of strain relaxation, which delivers better material quality. The SML-QD solar cell gave an enhanced solar cell performance: an increased current density of 17.7 $mA.cm^{-2}$, which marks ~11% improvement from 15.9 $mA.cm^{-2}$ of the QW solar cell. Its open-circuit voltage also increased ~70 mV to 0.69 V. However, due to the low activation energy, the samples would not work well as an IBSC candidate. The SML-QD structure requires a high bandgap capping layer to better fit the IBSC concept.

Five InAs/GaAs-QD solar cells, a GaAs reference solar cell and GaAs reference cell with doping were grown. The QD solar cells were grown via the Stranski-Kranstanov mode with Si impurities directly inserted into the QD during the growth. J-V curves show a recovery in open-circuit voltage in the doped QD solar cells compared with reference QD solar cells. This was attributed to the increased

confinement potential of the QD, verified by a characteristic blueshift in the PL emission spectra. EQE measurements provided evidence that a state-filling effect took place in the QD. The results led to a hypothesis of an electrostatic potential barrier formed between the QD and the wetting layer, supported by the time-resolve PL spectra. These findings has helped to explain the voltage-recovery characteristic by reducing thermal-coupling effect. This finding is beneficial to IBSC operations and could help to improve future IBSC designs by recovery the voltage.

Conventional InAs/GaAs QD solar cells grown by Stranski-Kranstanov mode were subjected to a post-growth rapid thermal process with 3 different temperatures: 650, 700 and 750 °C. Rapid thermal annealing led to stronger PL emission spectra and suppresses the NR-recombination, as supported by the increased EQE spectra. NR recombination effects were suppressed in the GaAs material as well as the QD material, which would help to improve material quality in IBSC. This study offers an approach for improving material quality of IBSC for future studies.

Finally, to fabricate a QD solar cell with ideal sub-bandgaps to fit IBSC requirements, InAs/InGaP QD solar cells were studied. The growth of InAs QDs directly on an InGaP buffer layer has been systematically investigated. The evolution of InAs-QD grown on an InGaP buffer layer was examined as a function of InAs coverage and growth temperature. To counter cross-diffusion of atoms, an AlGaAs interlayer was inserted between InAs and the InGaP buffer layer to prevent the surface exchange reactions between InAs and InGaP. As a result, InAs QDs with a density of 1×10^{11} cm^{-2} have been demonstrated with stronger PL emission compared to those with GaAs interlayers. The QD solar cell studied here showed the bandgap configuration of InAs/AlGaAs/InGaP QD system is close to that of the ideal IBSC, which provides a new system of choice for future test of a two-photon absorption effect.

8.2 Future Work

In the chapters four, five, six and seven, favourable QD discrete energy levels were successfully extracted from the InAs-QD energy states to mimic the IB, which allowed the photogeneration pathway to make use of sub-bandgap photons. However, the photocurrent produced is insufficient compared to its host material, as seen in the EQE results. Due to the short carrier lifetime of the QD nanomaterial which causes high recombination rates [144], the optimal IBSC operation is limited. There is a need to achieve QD materials with a long carrier lifetime and low recombination rates in order to maintain a populated IB. Type-II QD configuration should be explored to achieve this. It exhibits spatially separated electrons and holes which enables long carrier lifetime endurance. This is evidenced from TRPL which shows an dramatic increased carrier lifetime by a factor of 54 [87]. InAs/$GaAs_{1-x}Sb_x$ QD (x>14%) is a suitable material system to form type-II configuration, and research on this material system is ongoing [34].

Since QD provide photovoltaic conversion of below-bandgap photons to multistep electron transitions, longer carrier lifetime in QD would be beneficial. In fact, the potential material system for IBSC that needs to fulfil the requirement of (i) having zero band offset between QD and barrier in order to avoid V_{OC} losses and (ii) confinement of both carrier types is InAs-QD/GaAsSb [181]. Furthermore, it has been shown that due to Sb-As exchange, the Sb-containing buffer layers used to host the QD forms a surfactant layer which lowers the surface energy and favours a nucleation process that results in a bonus increase in QD areal density [106, 130, 182]. This is an added benefit to help solve the low-QD density problem documented in chapter four.

However, one problem with type-II QD solar cells is the reduced wavefunction overlapping in the QD, which gives a weaker photon-electron coupling and results in decreased absorption. Therefore, to counter this problem confinement enhancing (CE) techniques can be used to increase absorption coefficient [183]. This increases the oscillation strength of the IR absorption [184]. To achieve this, the QD solar cell

design requires the implementation of high bandgap material such as AlGaAs, which is similar to the work shown in chapter seven where high bandgap offset between the QD and the host material is created. It has been reported that this configuration applied to QD infra-red photodetector has achieved enhanced absorption [183]. Figure 8.1 shows a band gap diagram with AlGaAs CE barrier in a QD system:

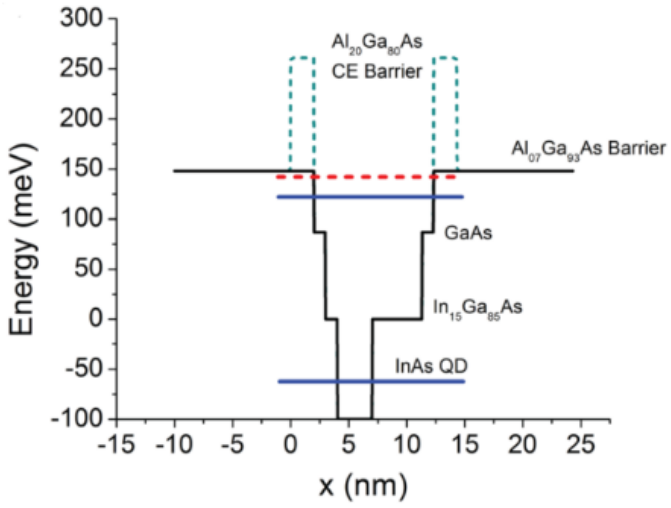

Figure 8.1: Band diagram of QD enclosed with AlGaAs confinement enhancing layer [183]

CE barriers are capable in supressing electron capture to QDs, therefore facilitates the reduction in recombination [185], especially Auger recombination. Therefore, in the proposed QD solar cell structure, AlGaAs barrier material is used to sandwich the InAs/GaAsSb QD system as depicted in Figure 8.2. The figure shows a schematic layout of a type-II InAs/GaAsSb QD solar cell structure with AlGaAs barrier layer. This proposed structure could use Stranski-Kranstanov mode to grow QD with high uniformity, as shown in chapter 7. The growth can be optimised to reduce coalescence and minimise defective NR recombination as necessary to retain the maximum V_{OC} [137]. Note that the size of the QD can be affected by GaAsSb thickness and the residual strain at the GaAsSb surface can affect the type-I to type-II transitions [86], therefore the growth parameters for InAs-QD on GaAsSb surface should follow closely to those used in the work of Ref [34] to ensure the establishment of the type-II characteristic.

Furthermore, it has been reported that the insertion of an Al-contained layer causes a redshift for the GS due to the suppression of the In segregation, where distinct effects of suppressing the intermixing and strain-reducing is seen [186]. This seems to be an interesting feature suggesting that the effect of RTP process on QD solar cell could yield alternative results compared to those studied in chapter six. Ultimately, using what was learned in chapter five, n-type dopant incorporation into the QD could lead to strong charging of the QD. It has been reported that this QD charging effect allows for both enhancement of IR harvesting and suppression of electron capture also [185].

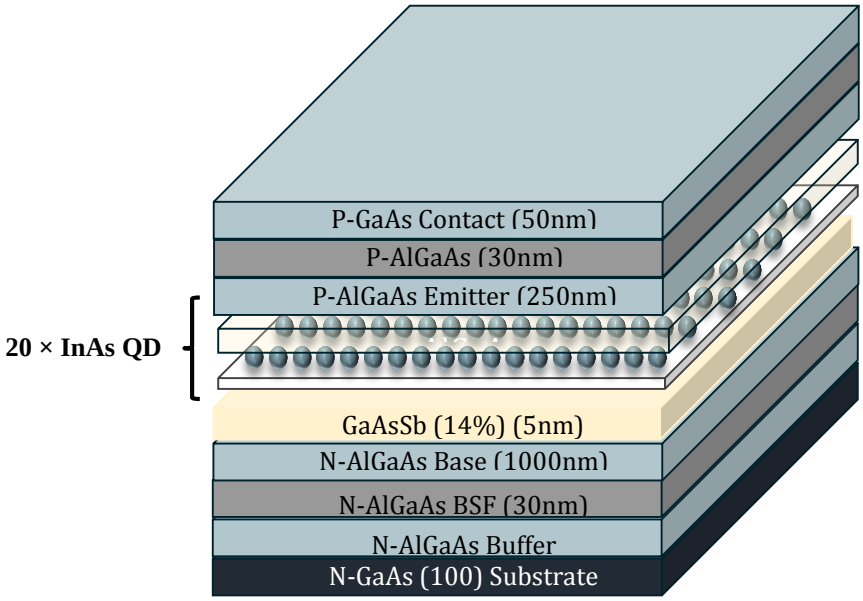

Figure 8.2: Schematic illustration of a QD solar cell structure proposed for future work, using InAs-QD/GaAsSb type-II system to prolong carrier lifetime within a high-bandgap AlGaAs barrier.

The proposed structure enclosing the QD in AlGaAs layers may lead to intraband transition which enhances infrared absorption [183, 184]. This may be attributed by the fact that AlGaAs confining layers localises the QD's excited wave function and enhances the absorption strength of the GS electrons by stronger wave function coupling [184]. The transfer of this mechanism to IBSC is valuable. The Al composition in AlGaAs is usually 20-30% for CE layers. InAs-QD grown directly onto AlGaAs layers shows dislocation-free QD layers and there are no sign of strain built-up, as confirmed by BF-XTEM images [88]. Furthermore InAs/AlGaAs QD with

Al: 25% have a measured thermal activation energy of 361 meV [87], which facilitates the establishment of an ideal IBSC.

In terms of measurement, as AlGaAs enclosing the InAs/GaAsSb-QD is expected to raise the confinement potential. It is important to investigate the effect of this to the thermal activation energy of the QD using low temperature PL experiments. Also, the carrier lifetime in this structure is influenced by the spatial separation of carriers in the type-II configuration as well as the suppression of carrier capture mechanism via the CE layer, therefore carrier lifetime measurements using TRPL is important to understand the carrier behaviour in the AlGaAs material, GaAsSb material, InAs WL and InAs QD.

Bibliography

1. D. Pimenel, G. Rodrigues, T. Wang, R. Abrams, K. Goldberg, H. Staecker, E. Ma, L. Brueckner, L. Trovato, C. Chow, U. Govindarajulu, and S. Boerke, "Energy : Economic Renewable Issues Environmental the potential," Oxford Journals, vol. 44, no. 8, pp. 536–547, 2015.
2. M. Tran, "Nuclear Disaster Report - Guardian," Guardian, 2011. [Online]. Available: http://www.theguardian.com/world/2011/apr/12/japan-fukushima-chernobyl-crisis-comparison. [Accessed: 16-Feb-2016].
3. "Renewables 2015 Global Status Report," REN 21 Renewable Energy Policy Network for the 21st Century, 2015.
4. F. de Winter and R. B. Swenson, "Dawn of the solar era: A wake up call," Solar Today, pp. 1–5, 2006.
5. J. Blanco and S. Malato, Solar Energy Conversion And Photoenergy System - Volume I. 2009.
6. "Technology Roadmap," International Energy Agency, 2014. [Online]. Available: www.iea.org. [Accessed: 16-Feb-2016].
7. C. E. Fritts, "On the fritts selenium cells and batteries," J. Franklin Inst., vol. 119, no. 3, pp. 221–232, 1885.
8. M. A. Green, K. Emery, Y. Hishikawa, W. Warta, and E. D. Dunlop, "Solar cell efficiency tables (version 47)," Prog. Photovolt Res. Appl., vol. 15, pp. 659–676, 2015.
9. D. DeGraaff, S. Caldwell, R. Lacerda, G. Bunea, A. Terao, and D. Rose, "Qualification, Manufacturing, and Reliability Testing Methodologies for Deploying High-Reliability Solar Modules" Sunpower, 2010.
10. A. Basnet, "Architectural Integration of Photovoltaic and Solar Thermal Collector Systems into buildings," Norwegian University of Science and Technoloogy, 2012.
11. K. Sun, M. Zhu, L. Wang, and H. Liu, "Analysis of the Hybrid Power System for High-Altitude Unmanned Aircraft," Adv. Mater. Sci. Eng., vol. 2015, pp. 1–9, 2015.
12. A. Luque, "Will we exceed 50% efficiency in photovoltaics?," J. Appl. Phys., vol. 110, no. 3, p. 031301, 2011.
13. H. Sargent, "Colloidal Quantum Dot Solar Cells," Nat. Photonics, vol. 6, no. March, pp. 133–135, 2012.

14. “Renewable Power Generation Costs in 2014”, International Renewable Energy Agency, 2015.
15. W. Shockley and H. J. Queisser, “Detailed Balance Limit of Efficiency of p-n Junction Solar Cells,” J. Appl. Phys., vol. 32, no. 3, p. 510, 1961.
16. “Solar cell efficiencies, National Renewable Energy Laboratory.” [Online]. Available: http://www.nrel.gov/ncpv/images/efficiency_chart.jpg. [Accessed: 10-Feb-2016].
17. G. Conibeer, “Third-generation photovoltaics,” Mater. Today, vol. 10, no. 11, pp. 42–50, 2007.
18. A. J. Nozik, “Exciton multiplication and relaxation dynamics in quantum dots: applications to ultrahigh-efficiency solar photon conversion.,” Inorg. Chem., vol. 44, no. 20, pp. 6893–9, Oct. 2005.
19. A. Luque and A. Martı, “Increasing the Efficiency of Ideal Solar Cells by Photon Induced Transitions at Intermediate Levels,” Phys. Rev. Lett., vol. 78, no. 26, p. 1997, 1997.
20. A. Luque, A. Martí, and C. Stanley, “Understanding intermediate-band solar cells,” Nat. Photonics, vol. 6, no. 3, pp. 146–152, Feb. 2012.
21. S. Hubbard and R. Raffaelle, “Boosting solar-cell efficiency with quantum-dot-based nanotechnology,” SPIE, pp. 9–11, 2010.
22. R. P. Raffaelle, S. Sinharoy, J. Andersen, D. M. Wilt, and S. G. Bailey, “Multi-junction solar cell spectral tuning with quantum dots,” in Photovoltaic Energy Conversion, Conference Record of the 2006 IEEE 4th World Conference on, vol. 1, pp. 162–166, 2006
23. A. W. Walker, O. Thériault, and K. Hinzer, “Positioning and doping effects on quantum dot multi- junction solar cell performance,” no. April 2014, pp. 793–799, 2015.
24. C. Cypranowski, “Power Recovery of Radiation-damaged GaAs and InP solar cells,” Naval Postgraduate School, 1989.
25. C. Kerestes, D. V Forbes, Z. Bittner, S. Polly, Y. Lin, B. Richards, P. Sharps, and S. Hubbard, “Strain Effects on Radiation Tolerance of Quantum Dot Solar Cells,” IEEE, vol. 4, no. 1, pp. 224 – 232, 2011.
26. C. D. Cress, S. M. Hubbard, B. J. Landi, R. P. Raffaelle, and D. M. Wilt, “Quantum dot solar cell tolerance to alpha-particle irradiation,” Appl. Phys. Lett., vol. 91, no. 18, p. 183108, 2007.
27. H. C. Liu, M. Gao, J. McCaffrey, Z. R. Wasilewski, and S. Fafard, “Quantum dot infrared photodetectors,” Appl. Phys. Lett., vol. 78, no. 1, p. 79, 2001.
28. A. Marti, C. Tablero, E. Antolin, A. Luque, R. P. Campion, S. V Novikov, and C. T. Foxon, “Potential of Mn doped In1-xGaxN for implementing intermediate band solar cells,” Sol. Energy Mater. Sol. Cells, vol. 93, The Institution of Engineering and Technology, pp. 641–644, 2009.
29. N. Ahsan, N. Miyashita, M. Monirul Islam, K. M. Yu, W. Walukiewicz, and Y. Okada, “Two-photon excitation in an intermediate band solar cell structure,” Appl. Phys. Lett., vol. 100, no. 17, p. 172111, 2012.
30. T. Sogabe, Y. Shoji, M. Ohba, K. Yoshida, R. Tamaki, H.-F. Hong, C.-H. Wu, C.-T. Kuo, S. Tomić, and Y. Okada, “Intermediate-band dynamics of quantum dots solar cell in concentrator photovoltaic modules.,” Sci. Rep., vol. 4, p. 4792, Jan. 2014.

31. E. Antolín, A. Martí, C. D. Farmer, P. G. Linares, E. Hernández, a. M. Sánchez, T. Ben, S. I. Molina, C. R. Stanley, and A. Luque, "Reducing carrier escape in the InAs/GaAs quantum dot intermediate band solar cell," J. Appl. Phys., vol. 108, no. 6, p. 064513, 2010.
32. A. G. Jordan, R. W. Lade, and D. L. Scharfetter, "A Note on Fermi Levels, Quasi-Fermi Levels, and Terminal Voltages in Semiconductor Devices," Am. J. Phys., vol. 31, no. 7, p. 490, 1963.
33. T. Tayagaki, Y. Hoshi, and N. Usami, "Investigation of the open-circuit voltage in solar cells doped with quantum dots.," Sci. Rep., vol. 3, p. 2703, 2013.
34. S. Hatch, J. Wu, K. Sablon, P. Lam, M. Tang, Q. Jiang, and H. Liu, "InAs/GaAsSb quantum dot solar cells," Opt. Express, vol. 22, no. S3, p. A679, 2014.
35. S. A. Blokhin, A. V. Sakharov, A. M. Nadtochy, A. S. Pauysov, M. V. Maximov, N. N. Ledentsov, A. R. Kovsh, S. S. Mikhrin, V. M. Lantratov, S. A. Mintairov, N. A. Kaluzhniy, and M. Z. Shvarts, "AlGaAs/GaAs photovoltaic cells with an array of InGaAs QDs," Phys. Semicond. Devices, vol. 43, no. 4, pp. 514–518, 2009.
36. T. Morioka and Y. Okada, "Multi-Stacked InAs/GaAs/GaNAs Quantum Dots with Direct Si Doping for use in IBSC," IEEE, vol. 1, pp. 4–7, 2010.
37. K. A. Sablon, J. W. Little, V. Mitin, A. Sergeev, and N. Vagidov, "Strong Enhancement of Solar Cell Efficiency Due to Quantum Dots," Nano Lett., vol. 11, pp. 2311–2317, 2011.
38. D. V. Forbes, A. M. Podell, M. A. Slocum, S. J. Polly, and S. M. Hubbard, "OMVPE of InAs quantum dots on an InGaP surface," Mater. Sci. Semicond. Process., vol. 16, no. 4, pp. 1148–1153, 2013.
39. C. Himwas, S. Panyakeow, and S. Kanjanachuchai, "Optical properties of as-grown and annealed InAs quantum dots on InGaAs cross-hatch patterns.," Nanoscale Res. Lett., vol. 6, no. 1, p. 496, 2011.
40. Y. Okada, T. Morioka, K. Yoshida, R. Oshima, Y. Shoji, T. Inoue, and T. Kita, "Increase in photocurrent by optical transitions via intermediate quantum states in direct-doped InAs/GaNAs strain-compensated quantum dot solar cell," J. Appl. Phys., vol. 109, no. 2, p. 024301, 2011.
41. P. Lam, J. Wu, M. Tang, Q. Jiang, S. Hatch, R. Beanland, J. Wilson, R. Allison, and H. Liu, "Submonolayer InGaAs/GaAs quantum dot solar cells," Sol. Energy Mater. Sol. Cells, vol. 126, pp. 83–87, 2014.
42. P. Lam, S. Hatch, J. Wu, M. Tang, V. G. Dorogan, Y. I. Mazur, G. J. Salamo, I. Ramiro, A. Seeds, and H. Liu, "Voltage recovery in charged InAs/GaAs quantum dot solar cells," Nano Energy, vol. 6, pp. 159–166, 2014.
43. P. Lam, J. Wu, M. Tang, D. Kim, S. Hatch, I. Ramiro, V. G. Dorogan, M. Benamara, Y. I. Mazur, G. J. Salamo, J. Wilson, R. Allison, and H. Liu, "InAs/InGaP quantum dot solar cells with an AlGaAs interlayer," Sol. Energy Mater. Sol. Cells, vol. 144, pp. 96–101, 2016.
44. M. Avadhanulu, "A textbook of engineering physics." S. Chand Publishing - Science, pp 845, 1992
45. "Absorption Coefficient vs Wavelength Graph." [Online]. Available: http://pveducation.org/pvcdrom/pn-junction/absorption-coefficient.

[Accessed: 12-Feb-2016].
46. R.S. Sedha, "A Textbook of Electronic Circuits", S. Chand Limited, 2014
47. R. Chavali, J. Wilcox, B. Ray, J. Gray, M. Alam, "Correlated Non-ideal Effects of Dark and Light IV Characteristics in a-Si/c-Si Heterojunction Solar Cells". IEEE Journal of Photovoltaics, vol. 4, no. 3, pp 763–771, 2014.
48. I. Ramiro, A. Martı, E. Antolın, and A. Luque, "Review of Experimental Results Related to the Operation of Intermediate Band Solar Cells," IEEE J. Photovoltaics, vol. 4, no. 2, pp. 736–748, 2014.
49. A. Luque and A. Martí, "The Intermediate Band Solar Cell: Progress Toward the Realization of an Attractive Concept," Adv. Mater., vol. 22, no. 2, pp. 160–174, 2010.
50. A. Luque, "Photovoltaics: Towards the intermediate band," Nat. Photonics, vol. 2, no. March, p. 166, 2011.
51. Y. Okada, N. Ekins-Daukes, T. Kita, R. Tamaki, M. Yoshida, A. Pusch, O. Hess, C. C. Phillips, D. J. Farrell, K. Yoshida, N. Ahsan, Y. Shoji, T. Sogabe, and J.-F. Guillemoles, "Intermediate band solar cells: Recent progress and future directions" Applied Physics Reviews, pp. 021302, 2015
52. W. G. Hu, T. Inoue, O. Kojima, and T. Kita, "Effects of absorption coefficients and intermediate-band filling in InAs/GaAs quantum dot solar cells," Appl. Phys. Lett., vol. 97, no. 19, p. 193106, 2010.
53. K. Yoshida, Y. Okada, and N. Sano, "Device simulation of intermediate band solar cells: Effects of doping and concentration," J. Appl. Phys., vol. 112, no. 8, p. 084510, 2012.
54. F. Xu, X.-G. Yang, S. Luo, Z.-R. Lv, and T. Yang, "Enhanced performance of quantum dot solar cells based on type II quantum dots," J. Appl. Phys., vol. 116, no. 13, p. 133102, 2014.
55. A. Lin and J. Phillips, "Drift-Diffusion Modeling for Impurity Photovoltaic Devices," IEEE Transactions on Electronic Devices, vol. 56, no. 12, pp. 3168–3174, 2009.
56. S. Tomić, "Intermediate-band solar cells: Influence of band formation on dynamical processes in InAs/GaAs quantum dot arrays," Phys. Rev. B, vol. 82, no. 19, p. 195321, 2010.
57. M. Yoshida, N. J. Ekins-Daukes, D. J. Farrell, and C. C. Phillips, "Photon ratchet intermediate band solar cells," Appl. Phys. Lett., vol. 100, no. 26, pp. 3–7, 2012.
58. M. Grätzel, "The light and shade of perovskite solar cells," Nat. Mater., vol. 13, no. 9, pp. 838–842, 2014.
59. S. Mathew, A. Yella, P. Gao, R. Humphry-Baker, B. F. E. Curchod, N. Ashari-Astani, I. Tavernelli, U. Rothlisberger, M. K. Nazeeruddin, and M. Grätzel, "Dye-sensitized solar cells with 13% efficiency achieved through the molecular engineering of porphyrin sensitizers," Nat. Chem., vol. 6, no. 3, pp. 242–247, 2014.
60. H. M. Gibbs, G. Khitrova, and S. W. Koch, "Exciton–polariton light–semiconductor coupling effects," Nat. Photonics, vol. 5, no. 5, pp. 273–273, 2011.
61. G. Shan, X. Zhao, M. Hu, C. Shek, and W. Huang, "Vertical-external-cavity surface-emitting lasers and quantum dot lasers," Front. Optoelectron., vol. 5,

no. 2, pp. 157–170, 2012.
62. Y. Yang, Y. Zheng, W. Cao, A. Titov, J. Hyvonen, J. R. Manders, J. Xue, P. H. Holloway, and L. Qian, “High-efficiency light-emitting devices based on quantum dots with tailored nanostructures,” Nat. Photonics, vol. 9, no. March, pp. 1–9, 2015.
63. T.-H. Kim, D.-Y. Chung, J. Ku, I. Song, S. Sul, D.-H. Kim, K.-S. Cho, B. L. Choi, J. Min Kim, S. Hwang, and K. Kim, “Heterogeneous stacking of nanodot monolayers by dry pick-and-place transfer and its applications in quantum dot light-emitting diodes.,” Nat. Commun., vol. 4, p. 2637, 2013.
64. S. Coe-Sullivan, W. Liu, P. Allen, and J. S. Steckel, “Quantum Dots for LED Downconversion in Display Applications,” ECS J. Solid State Sci. Technol., vol. 2, no. 2, pp. R3026–R3030, 2012.
65. K. A. Sablon, J. W. Little, V. Mitin, A. Sergeev, and N. Vagidov, “Strong Enhancement of Solar Cell Efficiency Due to Quantum Dots,” Nano Lett., vol. 11, no. 6, pp. 2311–2317, 2011.
66. V. Klimov, A. Mikhailovsky, S. Xu, A. Malko, J. Hollingsworth, C. A. Leatherdale, H. Eisler, and M. G. Bawendi, “Optical gain and stimulated emission in nanocrystal quantum dots,” Science, vol. 290, no. 5490, pp. 314–317, 2000.
67. T. Jamieson, R. Bakhshi, D. Petrova, R. Pocock, M. Imani, and A. M. Seifalian, “Biological applications of quantum dots,” Biomaterials, vol. 28, no. 31, pp. 4717–4732, 2007.
68. J. Urayama, T. B. Norris, J. Singh, and P. Bhattacharya, “Observation of phonon bottleneck in quantum dot electronic relaxation,” Phys. Rev. Lett., vol. 86, no. 21, pp. 4930–4933, 2001.
69. R. T. Ross, “Efficiency of hot-carrier solar energy converters,” J. Appl. Phys., vol. 53, no. 5, p. 3813, 1982.
70. C.-P. Tsai, S.-C. Hsu, S.-Y. Lin, C.-W. Chang, L.-W. Tu, K.-C. Chen, T.-S. Lay, and C.-C. Lin, “Type II GaSb quantum ring solar cells under concentrated sunlight.,” Opt. Express, vol. 22 Suppl 2, no. March, pp. A359–64, 2014.
71. J. Cui, Q. He, X. M. Jiang, Y. L. Fan, X. J. Yang, F. Xue, and Z. M. Jiang, “Self-assembled SiGe quantum rings grown on Si(001) by molecular beam epitaxy,” Appl. Phys. Lett., vol. 83, no. 14, p. 2907, 2003.
72. D. Granados and J. M. García, “In(Ga)As self-assembled quantum ring formation by molecular beam epitaxy,” Appl. Phys. Lett., vol. 82, no. 15, pp. 2401–2403, 2003.
73. Y. Zhang, J. Wu, M. Aagesen, J. Holm, S. Hatch, M. Tang, S. Huo, and H. Liu, “Self-Catalyzed Ternary Core–Shell GaAsP Nanowire Arrays Grown on Patterned Si Substrates by Molecular Beam Epitaxy,” Nano Lett., vol. 14, no. 8, pp. 4542–4547, 2014.
74. R. Calarco, R. J. Meijers, R. K. Debnath, T. Stoica, E. Sutter, and H. Lüth, “Nucleation and Growth of GaN Nanowires on Si(111) Performed by Molecular Beam Epitaxy,” Nano Lett., vol. 7, no. 8, pp. 2248–2251, 2007.
75. L. Cerutti, J. Ristić, S. Fernández-Garrido, E. Calleja, a. Trampert, K. H. Ploog, S. Lazic, and J. M. Calleja, “Wurtzite GaN nanocolumns grown on Si(001) by molecular beam epitaxy,” Appl. Phys. Lett., vol. 88, no. 21, pp.

160–163, 2006.
76. F. Rinaldi, “Basics of Molecular Beam Epitaxy (MBE)”, Annual Report 2002, Optoelectronics Department, University of Ulm, pp 1-8, 2000.
77. A. Barron, "Molecular Beam Epitaxy", OpenStax-CNX , Rice University course CHEM-496: Chemistry of Electronic Materials. 2009
78. K. Yamaguchi, “Self-Formation of Semiconductor Quantum Dots,” in Handbook of Nano-Optics and Nanoparticles, 2013, pp. 809–843.
79. K. Amaguchi, K. Ujobo, and T. Aizu, “Stranski-Krastanov Growth of InAs Quantum Dots with Narrow Size Distribution,” Appl. Phys., vol. 39, no. 12, pp. 1245–1248, 2000.
80. S. O. Ferreira, B. R. a Neves, R. Magalhães-Paniago, a. Malachias, P. H. O. Rappl, a. Y. Ueta, E. Abramof, and M. S. Andrade, “AFM characterization of PbTe quantum dots grown by molecular beam epitaxy under Volmer-Weber mode,” J. Cryst. Growth, vol. 231, pp. 121–128, 2001.
81. Y. Xu, E. Kernohan, M. Tselepi, C. Bland, and S. Holmes, “Single crystal Fe films grown on InAs(100) by molecular beam epitaxy,” Appl. Phys. Lett., vol. 73, no. 3, p. 399, 1998.
82. M. Copel, M. C. Reuter, E. Kaxiras, and R. M. Tromp, “Surfactants in epitaxial growth,” Phys. Rev. Lett., vol. 63, no. 6, pp. 632–635, 1989.
83. K. Oura, V. Lifshits, A. Saranin, A. Zotov, M. Katayama, "Surface Science: An Introduction" Advanced Texts in Physics, Springer-Verlag Berlin Heidelberg, 2003.
84. Z. S. Bittner, D. V Forbes, C. G. Bailey, S. J. Polly, M. A. Slocum, C. Kerestes, and S. M. Hubbard, “Characterization of InGaP Heterojunction Emitter Quantum Dot Solar Cells,” IEEE, pp. 3158–3161, 2011.
85. S. P. Bremner, A. Pancholi, K. Ghosh, S. Dahal, G. M. Liu, K. Y. Ban, M. Y. Levy, and C. B. Honsberg, “Growth of InAs Quantum Dots on GaAsSb for the realisation of a quantum dot solar cells on GaAs,” in 33rd IEEE Photovoltaic Specialists Conference, 2008.
86. Y. D. Jang, T. J. Badcock, D. J. Mowbray, M. S. Skolnick, J. Park, D. Lee, H. Y. Liu, M. J. Steer, and M. Hopkinson, “Carrier lifetimes in type-II InAs quantum dots capped with a GaAsSb strain reducing layer,” Appl. Phys. Lett., vol. 92, no. 25, p. 251905, 2008.
87. Í. Ramiro, E. Antolın, M. J. Steer, P. G. Linares, E. Hernández, I. Artacho, E. López1, T. Ben4, J. M. Ripalda, S. I. Molina, F. Briones, C. R. Stanley, A. Martí1, and A. Luque, “InAs / AlGaAs quantum dot intermediate band solar cells with enlarged sub-bandgaps,” in Photovoltaic Specialists Conference (PVSC), pp. 652–656, 2012
88. S. Lee, O. Lazarenkova, P. von Allmen, F. Oyafuso, and G. Klimeck, “Effect of wetting layers on the strain and electronic structure of InAs self-assembled quantum dots,” Phys. Rev. B, vol. 70, no. 12, p. 125307, 2004.
89. C. Adelmann, J. Simon, G. Feuillet, N. T. Pelekanos, B. Daudin, and G. Fishman, “Self-assembled InGaN quantum dots grown by molecular-beam epitaxy,” Appl. Phys. Lett., vol. 76, no. May 2015, p. 1570, 2000.
90. D. Leonard, “Molecular-beam epitaxy growth of quantum dots from strained coherent uniform islands of InGaAs on GaAs,” J. Vac. Sci. Technol. B Microelectron. Nanom. Struct., vol. 12, no. 2, p. 1063, 1994.

91. D. Bushnell, “Optimisation of strain-compensated multiquantum well solar cells,” Imperial College of Science, PhD Thesis, 2003.
92. H. Y. Liu, I. R. Sellers, M. Gutiérrez, K. M. Groom, W. M. Soong, M. Hopkinson, J. P. R. David, R. Beanland, T. J. Badcock, D. J. Mowbray, and M. S. Skolnick, “Influences of the spacer layer growth temperature on multilayer InAs ⁄ GaAs quantum dot structures,” J. Appl. Phys., vol. 96, no. 4, p. 1988, 2004.
93. F. K. Tutu, I. R. Sellers, M. G. Peinado, C. E. Pastore, S. M. Willis, a. R. Watt, T. Wang, and H. Y. Liu, “Improved performance of multilayer InAs/GaAs quantum-dot solar cells using a high-growth-temperature GaAs spacer layer,” J. Appl. Phys., vol. 111, no. 4, p. 046101, 2012.
94. T. Sugaya, S. Furue, H. Komaki, T. Amano, M. Mori, K. Komori, S. Niki, O. Numakami, and Y. Okano, “Highly stacked and well-aligned In[sub 0.4]Ga[sub 0.6]As quantum dot solar cells with In[sub 0.2]Ga[sub 0.8]As cap layer,” Appl. Phys. Lett., vol. 97, no. 2010, p. 183104, 2010.
95. A. Turala, A. Jaouad, D. P. Masson, S. Fafard, R. Arès, and V. Aimez, “Isolation of III-V/Ge Multijunction Solar Cells by Wet Etching,” Int. J. Photoenergy, vol. 2013, pp. 1–7, 2013.
96. O. Breitenstein, J. Bauer, A. Lotnyk, and J.-M. Wagner, “Defect induced non-ideal dark – characteristics of solar cells,” Superlattices Microstruct., vol. 45, no. 4–5, pp. 182–189, Apr. 2009.
97. G. E. Bulman, G. F. Gwilliam, and F. A. Chambers, “Low Resistance Ti/Pt/Au Ohmic Contacts to GaAs ⁄ Al[sub x]Ga[sub 1−x]As Heterostructures Using Open-Tube Zn Diffusion,” J. Electrochem. Soc., vol. 136, no. 8, p. 2423, 1989.
98. M. Yoder, “Ohmic contacts in GaAs,” Solid. State. Electron., vol. 23, no. 2, pp. 117–119, 1980.
99. F. Tutu, “InAs/GaAs Quantum Dot Solar Cells,” Ph.D Thesis, University College of London, 2013.
100. U. Maver, T. Maver, Z. Peršin, M. Mozetič, A. Vesel, M. Gaberšček and K. Stana-Kleinschek, "Polymer Characterization with the Atomic Force Microscope", Polymer Science, Cahpter 4, 2013
101. H. J. Snaith, “The perils of solar cell efficiency measurements,” Nature, vol. 6, no. June, pp. 337–340, 2012.
102. T. Sugaya, T. Amano, M. Mori, and S. Niki, “Highly stacked InGaAs quantum dot structures grown with two species of As,” J. Vac. Sci. Technol. B Microelectron. Nanom. Struct., vol. 28, no. 3, pp. C3C4–C3C8, 2010.
103. N. J. Ekins-Daukes, I. M. Ballard, K. W. J. Barnham, J. P. Connolly, and T. Tibbits, “Quantum wells in concentrator solar cells,” SPIE newsroom, 2008.
104. C. Heyn, “Critical coverage for strain-induced formation of InAs quantum dots,” Phys. Rev. B, vol. 64, no. 16, pp. 1–7, 2001.
105. A. J. Nozik, “Spectroscopy and Hot Electrons Relaxation Dynamics in Semiconductor Quantum Wells and Quantum Dots,” Renew. Energy, pp. 193–231, 2001.
106. F. K. Tutu, J. Wu, P. Lam, M. Tang, N. Miyashita, Y. Okada, J. Wilson, R. Allison, and H. Liu, “Antimony mediated growth of high-density InAs quantum dots for photovoltaic cells,” Appl. Phys. Lett., vol. 103, no. 4, p.

043901, 2013.
107. P. J. Simmonds, M. Sun, R. B. Laghumavarapu, B. Liang, A. G. Norman, J.-W. Luo, and D. L. Huffaker, "Improved quantum dot stacking for intermediate band solar cells using strain compensation.," Nanotechnology, vol. 25, no. 44, p. 445402, 2014.
108. H. Y. Liu, B. Xu, Y. H. Chen, D. Ding, and Z. G. Wang, "Effects of seed layer on the realization of larger self-assembled coherent InAs/GaAs quantum dots," J. Appl. Phys., vol. 88, no. 9, p. 5433, 2000.
109. C. G. Van de Walle, "Band lineups and deformation potentials in the model-solid theory," Phys. Rev., vol. 39, no. 3, 1989.
110. K. Rammohan, H. T. Lin, and A. Larsson, "Influence of misfit dislocations on thermal quenching of luminescence in InGaAs/GaAs multiple quantum wells," J. Appl. Phys., vol. 78, no. 11, pp. 6687–6690, 1995.
111. K. Stewart, M. Buda, J. Wong-Leung, L. Fu, C. Jagadish, a. Stiff-Roberts, and P. Bhattacharya, "Influence of rapid thermal annealing on a 30 stack InAs/GaAs quantum dot infrared photodetector," J. Appl. Phys., vol. 94, no. 8, p. 5283, 2003.
112. T. Morioka and Y. Okada, "Dark current characteristics of InAs/GaNAs strain-compensated quantum dot solar cells," Phys. E Low-dimensional Syst. Nanostructures, vol. 44, no. 2, pp. 390–393, 2011.
113. T. Morioka, Y. Shoji, and Y. Okada, "Current enhancement in direct-doped InAs/GaNAs strain-compensated quantum dot solar cell," 2011 37th IEEE Photovolt. Spec. Conf., pp. 003499–003502, 2011.
114. H. Y. Liu, M. J. Steer, T. J. Badcock, D. J. Mowbray, M. S. Skolnick, P. Navaretti, K. M. Groom, M. Hopkinson, and R. a. Hogg, "Long-wavelength light emission and lasing from InAs ⁄ GaAs quantum dots covered by a GaAsSb strain-reducing layer," Appl. Phys. Lett., vol. 86, no. 14, p. 143108, 2005.
115. X. Yang, T. Yang, K. Wang, H. Ji, H. Ni, Z. Niu, and Z. Wang, "Effect of antimony irradiation on InAs/Sb:GaAs quantum dots grown by molecular beam epitaxy," Semicond. Sci. Technol., vol. 26, no. 7, p. 075010, 2011.
116. L. Cuadra, A. Martí, and A. Luque, "Strain Considerations for the design of quantum dot intermediate band solar cell in the InGaAsAlGaAs Material System," in 17th European Photovoltaic Solar Energy Conference and Exhibition, 2001.
117. D. Z.-Y. Ting, S. V. Bandara, S. D. Gunapala, J. M. Mumolo, S. a. Keo, C. J. Hill, J. K. Liu, E. R. Blazejewski, S. B. Rafol, and Y.-C. Chang, "Submonolayer quantum dot infrared photodetector," Appl. Phys. Lett., vol. 94, no. 11, p. 111107, 2009.
118. X.-K. Li, D.-C. Liang, P. Jin, Q. An, H. Wei, J. Wu, and Z.-G. Wang, "InAs/GaAs submonolayer quantum dot superluminescent diode emitting around 970 nm," Chinese Phys. B, vol. 21, no. 2, p. 028102, 2012.
119. N. N. Ledentsov, D. Bimberg, F. Hopfer, A. Mutig, and V. A. Shchukin, "Submonolayer quantum dots for high speed surface emitting lasers.," Nanoscale Res. Lett., vol. 2, no. 9, pp. 417–29, 2007.
120. J. O. Kim, S. Sengupta, Y. Sharma, A. V. Barve, S. J. Lee, S. K. Noh, and S. Krishna, "Sub-monolayer InAs/InGaAs quantum dot infrared photodetectors

(SML-QDIP)," in Proceedings of SPIE, vol. 8353, pp. 835336–835336–6, 2012

121. H. Y. Liu, C. M. Tey, I. R. Sellers, T. J. Badcock, D. J. Mowbray, M. S. Skolnick, R. Beanland, M. Hopkinson, and A. G. Cullis, "Mechanism for improvements of optical properties of 1.3-μm InAs ⁄ GaAs quantum dots by a combined InAlAs–InGaAs cap layer," J. Appl. Phys., vol. 98, no. 8, p. 083516, 2005.
122. F. K. Tutu, P. Lam, J. Wu, N. Miyashita, Y. Okada, K.-H. Lee, N. J. Ekins-Daukes, J. Wilson, and H. Liu, "InAs/GaAs quantum dot solar cell with an AlAs cap layer," Appl. Phys. Lett., vol. 102, no. 16, p. 163907, 2013.
123. S. Sengupta, J. O. Kim, a. V. Barve, S. Adhikary, Y. D. Sharma, N. Gautam, S. J. Lee, S. K. Noh, S. Chakrabarti, and S. Krishna, "Sub-monolayer quantum dots in confinement enhanced dots-in-a-well heterostructure," Appl. Phys. Lett., vol. 100, no. 19, p. 191111, 2012.
124. J. F. Chen, R. S. Hsiao, Y. P. Chen, J. S. Wang, and J. Y. Chi, "Strain relaxation in InAs ⁄ InGaAs quantum dots investigated by photoluminescence and capacitance-voltage profiling," Appl. Phys. Lett., vol. 87, no. 14, p. 141911, 2005.
125. E. Fitzgerald, M. Currie, S. Samavedam, T. Langdo, G. Taraschi, V. Yang, C. Leitz, and M. Bulsara, "Dislocations in Relaxed SiGe/Si Heterostructures", phys. stat. sol. (a), vol. 171, pp. 227–238, 1999
126. A. Lenz, E. Lenz, U. W. Pohl, D. Bimberg, and M. Da, "Atomic Structure of Buried InAs Sub-Monolayer Depositions in GaAs," Appl. Phys. Express, vol. 3, no. 10, p. 105602, 2010.
127. S. M. Hubbard, C. D. Cress, C. G. Bailey, R. P. Raffaelle, S. G. Bailey, and D. M. Wilt, "Effect of strain compensation on quantum dot enhanced GaAs solar cells," Appl. Phys. Lett., vol. 92, no. 12, p. 123512, 2008.
128. Z. Xua and Y. Zhang, "Short exciton radiative lifetime in submonolayer InGaAs ⁄ GaAs quantum dots", App. Phys. Lett, vol. 92, pp. 063103, 2008
129. J. C. Zolper and A. M. Barnett, "The effect of dislocations on the performance of gallium arsenide solar cells," Conf. Rec. Twent. IEEE Photovolt. Spec. Conf., vol. 37, no. 2, pp. 478–484, 1988.
130. P. Aivaliotis, L. R. Wilson, E. a. Zibik, J. W. Cockburn, M. J. Steer, and H. Y. Liu, "Enhancing the dot density in quantum dot infrared photodetectors via the incorporation of antimony," Appl. Phys. Lett., vol. 91, no. 1, p. 013503, 2007.
131. S. Sengupta, A. Mandal, H. Ghadi, S. Chakrabarti, and K. L. Mathur, "Comprehensive study on molecular beam epitaxy-grown InAs sub-monolayer quantum dots with different capping combinations," J. Vac. Sci. Technol. B Microelectron. Nanom. Struct., vol. 31, no. 3, p. 03C136, 2013.
132. A. Marti, E. Antolin, E. Canovas, N. Lopez, P. Linares, A. Luque, C. R. Stanley, and C. D. Farmer, "Elements of the design and analysis of quantum-dot intermediate band solar cells," Thin Solid Films, vol. 516, no. 20, pp. 6716–6722, 2008.
133. A. Mellor, A. Luque, I. Tobías, and A. Martí, "The feasibility of high-efficiency InAs/GaAs quantum dot intermediate band solar cells," Sol. Energy Mater. Sol. Cells, vol. 130, pp. 225–233, 2014.

134. P. G. Linares, A. Martí, E. Antolín, C. D. Farmer, Í. Ramiro, C. R. Stanley, and A. Luque, "Voltage recovery in intermediate band solar cells," Sol. Energy Mater. Sol. Cells, vol. 98, pp. 240–244, 2012.
135. A. Luque, S. Member, and A. Martí, "On the Partial Filling of the Intermediate Band in IB Solar Cells," IEEE Trans. Electron Devices, vol. 57, no. 6, pp. 1201–1207, 2010.
136. I. Ramiro, E. Antolín, P. G. Linares, E. Hernández, a. Martí, a. Luque, C. D. Farmer, and C. R. Stanley, "Application of photoluminescence and electroluminescence techniques to the characterization of intermediate band solar cells," Energy Procedia, vol. 10, pp. 117–121, 2011.
137. C. Bailey, D. Forbes, S. Polly, Z. Bittner, Y. Dai, C. Mackos, R. Raffaelle, and S. Hubbard, "Open-Circuit Voltage Improvement of InAs / GaAs Quantum-Dot Solar Cells Using Reduced InAs Coverage," IEEE J. Photovoltaics, vol. 2, no. 3, pp. 269–275, 2012.
138. R. B. Laghumavarapu, M. El-Emawy, N. Nuntawong, a. Moscho, L. F. Lester, and D. L. Huffaker, "Improved device performance of InAs ⁄ GaAs quantum dot solar cells with GaP strain compensation layers," Appl. Phys. Lett., vol. 91, no. 24, p. 243115, 2007.
139. A. Luque and A. Martı, "A metallic intermediate band high efficiency solar cell," Prog. Photovoltaics Res. Appl., vol. 9, no. 2, pp. 73–86, 2001.
140. A. Marti, E. Antolin, E. Cánovas, N. López, and A. Luque, "Progress in quantum-dot intermediate band solar cell research," in Proc. of the 21st European Photovoltaic Solar Energy Conference, pp. 99–102, 2006
141. A. Luque and A. Marti, "The intermediate band solar cell: progress toward the realization of an attractive concept.," Adv. Mater., vol. 22, no. 2, pp. 160–174, 2010.
142. X. Yang, K. Wang, Y. Gu, H. Ni, X. Wang, T. Yang, and Z. Wang, "Improved efficiency of InAs/GaAs quantum dots solar cells by Si-doping," Sol. Energy Mater. Sol. Cells, vol. 113, pp. 144–147, 2013.
143. T. S. Wang, J. T. Tsai, K. I. Lin, J. S. Hwang, H. H. Lin, and L. C. Chou, "Characterization of band gap in GaAsSb/GaAs heterojunction and band alignment in GaAsSb/GaAs multiple quantum wells," Mater. Sci. Eng. B, vol. 147, no. 2–3, pp. 131–135, 2008.
144. H. J. Queisser, "Photovoltaic conversion at reduced dimensions," Phys. E Low-dimensional Syst. Nanostructures, vol. 14, no. 1–2, pp. 1–10, 2002.
145. J. Phillips, K. Kamath, X. Zhou, N. Chervela, and P. Bhattacharya, "Photoluminescence and far-infrared absorption in Si-doped self-organized InAs quantum dots," Appl. Phys. Lett., vol. 71, no. 15, pp. 2079, 1997.
146. H. L. Wang, F. H. Yang, and S. L. Feng, "Photoluminescence in Si and Be directly doped self-organized InAs/GaAs quantum dots," J. Cryst. Growth, vol. 212, no. 1–2, pp. 35–38, 2000.
147. C. Y. Jin, H. Y. Liu, S. Y. Zhang, Q. Jiang, S. L. Liew, M. Hopkinson, T. J. Badcock, E. Nabavi, and D. J. Mowbray, "Optical transitions in type-II InAs ⁄ GaAs quantum dots covered by a GaAsSb strain-reducing layer," Appl. Phys. Lett., vol. 91, no. 2, p. 021102, 2007.
148. K. Drozdowicz-Tomsia, E. M. Goldys, L. Fu, and C. Jagadish, "Doping effect on dark currents in In0.5Ga0.5As ⁄ GaAs quantum dot infrared

photodetectors grown by metal-organic chemical vapor deposition," Appl. Phys. Lett., vol. 89, no. 11, p. 113510, 2006.
149. B. Zeghbroeck, "Principles of Semiconductor Devices", Colarado University, 2004.
150. T. Kita, R. Hasagawa, and T. Inoue, "Suppression of nonradiative recombination process in directly Si-doped InAs/GaAs quantum dots," J. Appl. Phys., vol. 110, no. 10, pp. 103511, 2011.
151. "Introduction to Time-resolved photoluminescence." [Online]. Available: https://www.picoquant.com/applications/category/materials-science/time-resolved-photoluminescence. [Accessed: 17-Jul-2016].
152. A. Babiński, J. Jasiński, R. Bożek, A. Szepielow, and J. M. Baranowski, "Rapid thermal annealing of InAs/GaAs quantum dots under a GaAs proximity cap," Appl. Phys. Lett., vol. 79, no. 16, pp. 2576, 2001.
153. H. Zhao, S. F. Yoon, C. Y. Ngo, and R. Wang, "Improved ground-state modulation characteristics in 1.3 μm InAs/GaAs quantum dot lasers by rapid thermal annealing.," Nanoscale Res. Lett., vol. 6, no. 1, p. 382, 2011.
154. R. Gunawan, M. Y. L. Jung, E. G. Seebauer, and R. D. Braatz, "Optimal control of rapid thermal annealing in a semiconductor process," J. Process Control, vol. 14, no. 4, pp. 423–430, 2004.
155. W. H. Ng, E. a. Zibik, L. R. Wilson, M. S. Skolnick, J. W. Cockburn, and M. J. Steer, "Tuning of intraband absorption and photoresponse in self-assembled InAs ⁄ GaAs quantum dots by thermal annealing," J. Appl. Phys., vol. 103, no. 6, pp. 066101, 2008.
156. Y. Fukai and H. Sugimoto, "Formation mechanism of defect metal hydrides containing superabundant vacancies," J. Phys. Condens. Matter, vol. 19, no. 43, pp. 436201, 2007.
157. S. J. Xu, X. C. Wang, S. J. Chua, C. H. Wang, W. J. Fan, J. Jiang, and X. G. Xie, "Effects of rapid thermal annealing on structure and luminescence of self-assembled InAs/GaAs quantum dots," Appl. Phys. Lett., vol. 72, no. 25, p. 3335, 1998.
158. L. Fu, P. Kuffner, I. McKerracher, H. H. Tan, and C. Jagadish, "Rapid thermal annealing study of InGaAs/GaAs quantum dot infrared photodetectors grown by metal-organic chemical vapor deposition," Lasers Electro-Optics Soc, LEOS 2005. 18th Annu. Meet. IEEE, pp. 228–229, 2005.
159. K. Stewart, M. Buda, L. Fu, C. Jagadish, S. State, and C. Science, "Strain relaxation in rapid thermally annealed InAs/GaAs quantum dot infrared photodetectors," in Conference on Optoelectronic and Microelectronic Materials and Devices, pp. 475–478, 2002.
160. X. Zhou, Y. Chen, and B. Xu, "Optical identification of electronic state levels of an asymmetric InAs/InGaAs/GaAs dot-in-well structure.," Nanoscale Res. Lett., vol. 6, no. 1, p. 317, 2011.
161. J. Guo-Zhi, Y. Jiang-hong, S. Yong-chun, and X. X. and Pi-Biao, "Evolution of InAs Quantum Dots during Annealing Process," ACTA Phys. Pol. A, vol. 114, no. 4, pp. 919–923, 2008.
162. S. Hiratsuka, S. Saravanan, T. Harayama, and N. Ohtani, "Photoluminescence properties of annealed InAs quantum dots capped by InGaAs layers," Phys. Status Solidi, vol. 6, no. 1, pp. 189–192, 2009.

163. J.-F. Chen, R.-S. Hsiao, S.-H. Shih, P.-Y. Wang, J.-S. Wang, and J. Y. Chi, "Properties of Defect Traps in Triple-Stack InAs/GaAs Quantum Dots and Effect of Annealing," Jpn. J. Appl. Phys., vol. 43, no. 9A, p. L1150, 2004.
164. D. Guimard, R. Morihara, D. Bordel, K. Tanabe, Y. Wakayama, M. Nishioka, and Y. Arakawa, "Fabrication of InAs/GaAs quantum dot solar cells with enhanced photocurrent and without degradation of open circuit voltage," Appl. Phys. Lett., vol. 96, no. 20, p. 203507, 2010.
165. S. M. Hubbard, Chelsea Plourde, V. Forbes, and R. Raffaelle, "InAs quantum dot enhancement of GaAs solar cells," IEEE, pp. 1217–1222, 2010.
166. H. Yoshikawa, T. Kotani, Y. Kuzumoto, M. Izumi, Y. Tomomura, and C. Hamaguchi, "Proposal of high efficiency solar cells with closely stacked InAs/In0.48Ga0.52P quantum dot superlattices: Analysis of polarized absorption characteristics via intermediate–band," Appl. Phys. Lett., vol. 105, no. 1, p. 011120, 2014.
167. K. Ikeda, H. Sekiguchi, F. Minami, J. Yoshino, Y. Mitsumori, H. Amanai, S. Nagao, and S. Sakaki, "Phonon bottleneck effects in InAs/GaInP quantum dots," J. Lumin., vol. 108, no. 1–4, pp. 273–276, 2004.
168. T. Sugaya, A. Takeda, R. Oshima, K. Matsubara, S. Niki, and Y. Okano, "InGaP-based InGaAs quantum dot solar cells with GaAs spacer layer fabricated using solid-source molecular beam epitaxy," Appl. Phys. Lett., vol. 101, no. 13, p. 133110, 2012.
169. I. Ramiro, J. Villa, P. Lam, S. Hatch, J. Wu, L. Esther, E. Antol, H. Liu, and A. Mart, "Wide-Bandgap InAs / InGaP Quantum-Dot Intermediate Band Solar Cells," IEEE J. Photovoltaics, vol. 5, no. 3, pp. 840–845, 2015.
170. H. Y. Liu, B. Xu, Y. H. Chen, D. Ding, and Z. G. Wang, "Effects of seed layer on the realization of larger self-assembled coherent InAs/GaAs quantum dots," J. Appl. Phys., vol. 88, no. 9, p. 5433, 2000.
171. H. Amanai, S. Nagao, and H. Sakaki, "Growth and temperature characteristic of self-assembled InAs-QD on GaInP," J. Cryst. Growth, vol. 251, no. 1–4, pp. 223–229, 2003.
172. H. Y. Liu, I. R. Sellers, M. Gutiérrez, K. M. Groom, W. M. Soong, M. Hopkinson, J. P. R. David, R. Beanland, T. J. Badcock, D. J. Mowbray, and M. S. Skolnick, "Influences of the spacer layer growth temperature on multilayer InAs ⁄ GaAs quantum dot structures," J. Appl. Phys., vol. 96, no. 4, p. 1988, 2004.
173. H. Amanai, S. Nagao, and H. Sakaki, "InAs / GaInP self-assembled quantum dots : molecular beam epitaxial growth and optical properties," J. Cryst. Growth, vol. 228, pp. 1089–1094, 2001.
174. D. Zhou, G. Sharma, S. F. Thomassen, T. W. Reenaas, and B. O. Fimland, "Optimization towards high density quantum dots for intermediate band solar cells grown by molecular beam epitaxy," Appl. Phys. Lett., vol. 96, no. 6, pp. 061913–3, 2010.
175. H. Y. Liu, X. D. Wang, Y. Q. Wei, B. Xu, D. Ding, and Z. G. Wang, "Effects of interdiffusion on the luminescence of InAs/GaAs quantum dots covered by InGaAs overgrowth layer," J. Cryst. Growth, vol. 220, no. 3, pp. 216–219, 2000.
176. A.-S. Mahajumi, P. Carrington, I. Kostakis, M. Missous, A. Sanchez, Q.

Zhuang, R. Young, M. Hayne, and A. Krier, “Rapid thermal annealing and photoluminescence of type-II GaSb single monolayer quantum dot stacks,” J. Phys. D. Appl. Phys., vol. 46, no. 30, p. 305104, 2013.

177. P. M. Lam, J. Wu, R. Allison, S. Hatch, M. Tang, J. Wilson, D. Kim, and H. Liu, “Effect of rapid thermal annealing on InAs/GaAs quantum dot solar cells,” IET Optoelectron., vol. 9, no. 2, pp. 65–68, 2015.
178. M. M. Sobolev, I. V Kochnev, V. M. Lantratov, N. A. Bert, N. A. Cherkashin, N. N. Ledentsov, and D. A. Bedarev, “Thermal annealing of defects in InGaAs/GaAs heterostructures with three-dimensional islands,” Semiconductors, vol. 34, no. 2, pp. 195–204, 2000.
179. K. Cui, B. J. Robinson, D. A. Thompson, and G. A. Botton, “Effect of layer separation, InAs thickness, and rapid thermal annealing on the optical emission from a multi-layer quantum wire structure,” J. Appl. Phys., vol. 109, no. 12, pp. 1–10, 2011.
180. Y. Shiraki, T. Mishima, and M. Morioka, “Low temperature MBE growth of high quality AlGaAs,” J. Cryst. Growth, vol. 81, pp. 164–168, 1987.
181. M. Y. Levy, C. Honsberg, A. Martí, and A. Luque, “Quantum dot intermediate band solar cell material systems with negligable valence band offsets” Conference Record of the Thirty-first IEEE Photovoltaic Specialists Conference, pp. 90–93, 2005
182. D. Guimard, M. Nishioka, S. Tsukamoto, and Y. Arakawa, “Effect of antimony on the density of InAs/Sb:GaAs(100) quantum dots grown by metalorganic chemical-vapor deposition,” J. Cryst. Growth, vol. 298, pp. 548–552, 2007.
183. V. Barve, S. Sengupta, J. O. Kim, Y. D. Sharma, S. Adhikary, T. J. Rotter, S. J. Lee, Y. H. Kim, and S. Krishna, “Confinement enhancing barriers for high performance quantum dots-in-a-well infrared detectors,” Appl. Phys. Lett., vol. 99, no. 19, p. 191110, 2011.
184. H. S. Ling, S. Y. Wang, C. P. Lee, and M. C. Lo, “High quantum efficiency dots-in-a-well quantum dot infrared photodetectors with AlGaAs confinement enhancing layer,” Appl. Phys. Lett., vol. 92, no. 19, p. 193506, 2008.
185. K. Sablon, A. Sergeev, N. Vagidov, J. W. Little, and V. Mitin, “Effects of quantum dot charging on photoelectron processes and solar cell characteristics,” Sol. Energy Mater. Sol. Cells, vol. 117, pp. 638–644, 2013.
186. Z. Y. Zhang, B. Xu, P. Jin, X. Q. Meng, C. M. Li, X. L. Ye, and Z. G. Wang, “Photoluminescence study of self-assembled InAs/GaAs quantum dots covered by an InAlAs and InGaAs combination layer,” J. Appl. Phys., vol. 92, no. 1, p. 511, 2002.